

Chapter 1 Introduction

1.1 The research background on GaN

The III-V Gallium nitride compound semiconductor have attracted a wide range of bandgaps and high temperature stability for optoelectronic and electronic devices such as light-emitting diodes (LEDs) [1]-[5], laser diodes (LDs) [6]-[8], photoconductive detectors, photovoltaic detectors [9]-[13] in the blue-ultraviolet (UV) range of spectrum, and metal-semiconductor field-effect transistors (MESFETs) [14], [15], high electron mobility transistors (HEMTs) [16], [17] in the high temperature/high power electronic devices. In order to fabricate GaN-based devices and define the mesa layer for formed p and n contacts, inductively coupled plasma reactive ion etching (ICP-RIE) method is generally applied due to GaN quite hard to etch. Precise pattern transfer during fabrication of these devices is required by using ICP-RIE etching method to break strongly Ga-N bonds (8.92 eV/atom). However, there are certain of ion-etching damages on the GaN in these processes. Moreover, ion bombardment from ICP-RIE etching process can induce dislocations or formation of dangling bonds on the GaN surface and may cause material and/or device damage after ICP etching process. Thus, a high leakage current which may result from various defects such as vacancy and dislocation can degrade the device characteristics. Previously, it was reported that studies of the GaN defects induced by ICP etching

process [18]-[22] in means of material [23]-[26] and device electrical behavior [27]-[32] analysis. The optical and electrical properties of semiconductor can be degraded because of ICP-induced defects in the leakage current or breakdown voltage of devices [33], [34].

On the other hand, Lee [35] has reported that leakage current of a GaN Schottky diode with annealing different temperatures after ICP etching process. Cheung [36] has developed the optical characterization of GaN with RIE-induced effects. Achouche [37] has discussed electrical characterization of InAlAs with RIE-induced damage. As a result, many groups have investigated the interfacial defect effects of GaN or other compound semiconductors. And these related process defects are reduced by thermal or chemical treatments [38], [39]. Therefore, to characterize interfacial defect and solve deteriorations of devices becomes an important issue.

1.2 Overview of the our studies

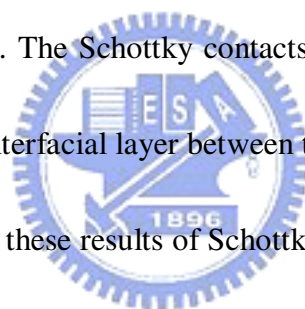
In order to characterize GaN interfacial defects and surface states effects, we can divide into two points in material properties and devices fabrications. First, we have utilized Schottky diodes to analyze these defects and material properties, and have defined the interfacial states density of these defects for Schottky diodes. Second, to apply results of Schottky contacts characteristics in interfacial states effects, the

GaN-based devices have been fabricated in metal-semiconductor-metal photodetectors (MSM-PDs) and *p-i-n* photodiodes (*p-i-n* PDs). We have demonstrated relationship between results of interfacial defects for Schottky contacts and GaN-based photodetector devices, and have been carried out the devices characteristics.

Previously, many studies of Schottky contacts in GaN have already been reported [17]-[39]. Although metal work function can effectively determine the Schottky barrier height due to the ionic nature of GaN, it is not the exclusive factor. The metal-semiconductor contacts can be divided into two groups: these made on lightly doped semiconductors and these made on heavily doped semiconductors. The first, general called Schottky barrier, have been studied and thermionic emission have been established as the current transport mechanisms. Second, ohmic contacts are usually made by metal on heavily doped semiconductor.

For electrical analysis, the leakage current and breakdown voltage in the reverse bias region for Schottky diodes were generally used to characterize the ICP etching GaN samples. Therefore, investigations of the ohmic and Schottky barriers on GaN are important both of metal characterization. In our report, characteristics of the ICP-induced defects have been developed and are divided into two issues. First, the current transport mechanisms of Ni-Au / *n*-GaN and the annealing effects of Schottky contacts after ICP etching process under the forward bias condition by the

current-voltage-temperature (I - V - T) methods. The current transport mechanisms are analyzed in terms of specific contact resistance (ρ_c), characteristic energy (E_{00}) and ideality factor (η) under different annealing temperatures. We have demonstrated that the current transport mechanisms are directly dependent on the surface treated conditions, and annealing processes are an effective step in eliminating these defects. On the other hand, we can also characterize the ICP-induced defects by capacitance-frequency (C - f) methods. The ICP-induced defects density on the GaN surface has been carried out by C - f measurements over a frequency range (100 Hz ~1MHz) at room temperature. The Schottky contacts are investigated by taking into account for the effects of an interfacial layer between the metal and semiconductor.



Second, we have utilized these results of Schottky contacts with different surface treatments to apply to GaN or AlGaIn-based photodiode devices. The surface treatments are classified KOH solutions and different annealing ambients at 600°C. The spectral responsivity for AlGaIn-based photodiode devices with different surface treatments is also studied. From this, the surface-treated effects and defects are discussed. We have found that the ICP-induced defects can be partially eliminated and the characteristics of the AlGaIn-based photodiodes devices improved by these surface treatments after ICP-RIE etching process.

This dissertation describes all aspects of interfacial states effects and is divided

into four parts- introduction, foundational theory, physical characteristics of devices and conclusion.

The first part, Chapter 1, describes the introduction of GaN-based background in this thesis. Overview of GaN-based material properties and related devices applications is developed.

The second part, Chapter 2, the theory and characteristics of Schottky contacts between metal and semiconductor in interfacial states density by current-voltage and capacitance-voltage methods is defined. On the other hand, the introduction of photodetector operation model and optical characteristics is discussed.

The three part, Chapter 3, 4 and 5 describes Schottky diodes properties in interfacial defects and defines interfacial states density of defects or damage by capacitance- frequency methods, characterize metal-semiconductor-metal photodetectors (MSM-PDs) and *p-i-n*-photodiodes with interfacial state effects due to different surface treatments, respectively.

The final part, Chapter 6 discusses the conclusion and future work in interfacial states effects to apply the other devices or fabrication.

Chapter 1 : Introduction

Chapter 2 : Foundational theory and physics

Chapter 3 : Interfacial states effects and characteristics for Schottky diodes

Chapter 4: Investigation of interfacial states for metal-semiconductor-metal photodetectors (MSM-PDs)

Chapter 5: Interfacial states effects and characteristics for *p-i-n*-photodiodes (*p-i-n*-PDs)

Chapter 6 : Conclusions and future prospects



Chapter 2 Foundational Theory and physics

2.1 Physical and electrical characteristics of metal-semiconductor rectifies

2.1.1 Introduction

When the metal makes intimate contact with semiconductor, the Fermi level in the two materials must be equal at thermal equilibrium, furthermore, the vacuum level must be continuous. For *n*-type semiconductor, as the metal work function (Φ_m) [40] is smaller than the semiconductor work function (Φ_s ; 4.07eV for GaN) [41], the contact denotes an ohmic contact. On the contrary, as the metal work function (Φ_m) is larger than the semiconductor work function (Φ_s), there is a rectifying behavior arising in metal-semiconductor contact. Because of Fermi level has to equal and vacuum level must be continuous at thermal equilibrium. As electrons in the semiconductor emit into metal, a depletion region collecting positive charge, bending up the conduction band and generating an electric potential well near the boundary are observed as shown in Fig.2-1. The barrier theory which was called Schottky barrier height was first developed by Schottky and Mott. [42]. For the ideal case, the Schottky barrier height ($q\Phi_B$) is simply the difference between the metal work function (Φ_m) and the semiconductor electron affinity $q\chi_s$ is defined by

$$q\phi_B = S[q\phi_m - q\chi_s] \quad (2-1)$$

where S is slope parameter $\left(= \frac{\partial \phi_B}{\partial \phi_m} \right)$. If S is unity, donate the barrier height relies on the metal work function. In contract, as S is zero, the barrier height is independent of the metal work function and a range of $0 < S < 1$, the barrier height is weakly dependent on the metal work function [43].

In general, an increase in the barrier height correlated with an increase in the

metal work function or semiconductor electron affinity. However, as the surface or defects states exist between semiconductor and metal, the barrier height is independent of metal work function and semiconductor electron affinity. This phenomenon denotes the Fermi level pinned at the interface by these surface states [43]. We found the results of this work and many reports discuss the relationship between the metal work function and barrier height as illustrated in Fig. 2-2 [44]-[48]. The barrier height is dependent on the metal work function but indicated large variations in value among the authors and this work. As the barrier height value is nearly in the solid line, it is dependent the metal work function. In contract, the barrier height by utilized the surface treatment is far the solid line. The dot line donates in this work for Schottky diodes with different surface treatments and discussed in next section. On the other hand, the extracted slope value S which denotes electronegativity differences results form the bunching of surface states near the band edges [29] is around 0.4 for GaN materials in Fig. 2-2, indicating the barrier height is weakly dependent on the metal work function in GaN materials [49].

2.1.2 Theory of current transport mechanisms for Schottky contacts

It is known that the barrier height of Schottky barrier diode is electric-field dependent [50]-[53]. If a metal-semiconductor (M-S) contact has no potential barrier at the interface, a true ohmic result has linear current-voltage characteristics in the bulk semiconductor. However, if the potential barrier is so low that a negligible amount of voltage drops across the interface between metal and semiconductor, and

an ohmic behavior is observed. The current transport mechanism for Schottky barrier height is dependent on image force lowering (neglect in this work), interfacial states, generation-recombination within the depletion layer and thermionic or field emission [54].

The current transport mechanisms for thermionic emission (TE) and field emission (FE) mechanisms for a metal and the n -type semiconductor are illustrated in Fig.2-3 (a) and Fig.2-3 (b), respectively. [50], [51]. The three regimes could be differentiated by the characteristic energy E_{00} is defined as

$$E_{00} = \frac{qh}{4\pi} \sqrt{\frac{N_d}{K_S \varepsilon_0 m^*}} = 1.86 \times 10^{-11} \sqrt{\frac{N_d}{K_S \left(\frac{m^*}{m}\right)}} = 1.86 \times 10^{-11} \sqrt{\frac{N_d}{K_S \left(\frac{A^*}{120}\right)}}, \quad [eV] \quad (2-2)$$

where q is the electronic charge, h Planck constant, N_d the donor concentration with N_d in units of cm^{-3} , m^* the effective mass of the tunneling electron, m the free electron

mass, K_S the semiconductor dielectric constant $\left(K_{S|\text{GaN}} = \frac{\varepsilon_S}{\varepsilon_0} = 9.5\right)$, and ε_0 is the permittivity of free space. The ratio $\frac{KT}{E_{00}}$ indicates that thermionic emission (TE) dominates as $\frac{KT}{E_{00}} \gg 1$; thermionic-field emission (TFE) dominates as $\frac{KT}{E_{00}} \cong 1$, and field emission (FE) dominates as $\frac{KT}{E_{00}} \ll 1$. The total current from semiconductor to metal is given by

$$I = AA^*T^2 \exp\left(\frac{-q\phi_B}{KT}\right) \exp\left(\frac{qV}{KT}\right) + \frac{AA^*T^2}{a} \left(\exp\left(\frac{-q\phi_B}{KT}\right) \exp\left(\frac{qV}{KT}\right) \right) - \exp\left(\frac{-q\phi_B}{E_{00}}\right) \exp\left(\frac{qV}{E_{00}}\right) \exp\left(a \frac{qV_n}{KT}\right)$$

(2-3)

where $E_{00} \approx 0$, the second term of Eq.(2-2) becomes zero with $\eta=1$, as a pure thermionic current [52].

2.1.2.1 Thermionic emission (TE)

For moderately semiconductor, $N_d \leq 10^{17} \text{ cm}^{-3}$, the depletion region is relatively wide. It is impossible to tunnel through the barrier unless aided by defects. The electrons can surmount the top of the barrier, which should be small for contacts, by thermionic emission (TE) as shown in Fig.2-3 (a). For low-doped or high-barrier semiconductors, the vast majority electrons would be unable to cross in either direction into the semiconductor, and the ohmic behavior is not observed.

In the thermionic emission (TE) region by $\frac{KT}{E_{00}} \gg 1$, the specific contact resistance $\rho_c (\Omega - \text{cm}^2)$ is given by [53]

$$\rho_c = \frac{K}{qA^*T} \exp\left(\frac{q\phi_B}{KT}\right), \quad [\Omega - \text{cm}^2] \quad (2-4)$$

$$A^* \left(= \frac{4\pi qK^2 m^*}{h^3} = 120 \left(\frac{m^*}{m_0} \right) \right), \quad \left[\frac{A}{\text{cm}^2 \text{K}^2} \right]$$

where A^* is the Richardson's constant.

2.1.2.2 Field emission (FE)

For heavily doped semiconductor, $N_d \geq 10^{18} \text{ cm}^{-3}$, the space charge region (scr) is narrow, and electrons can tunnel from the metal to the semiconductor and from the semiconductor to the metal by field emission (FE) in Fig.2-3 (b). The work function which is the best approach to pursue for ohmic contacts is the absence of a good match between the metal and the semiconductor. The ohmic contact doesn't depend on the work function between the metal and the semiconductor for field emission mechanism.

In the field emission (FE) region, the specific contact resistance $\rho_c (\Omega - \text{cm}^2)$ is given by

$$\rho_c = \frac{K}{q A^*} \exp\left(\frac{q\phi_B}{E_{00}}\right) \left[\frac{\pi T}{\sin(\pi C_1 K T)} \frac{\exp(-C_1 q V_n)}{K C_1} \right]^{-1}, \quad [\Omega - \text{cm}^2] \quad (2-9)$$

$$C_1 = \frac{1}{2E_{00}} \ln\left(\frac{4\phi_B}{V_n}\right), \quad \left[\frac{1}{eV} \right] \quad (2-10)$$

2.1.2.3 Thermionic-field emission (TFE)

For intermediately doped semiconductors, $\approx 10^{17} < N_d < 10^{18} \text{ cm}^{-3}$, the depletion region is not sufficiently thin to allow direct tunneling of carriers that are more or less in equilibrium. If the carriers gain a little energy, they may be able to tunnel. Consequently, both of thermionic field emission (TFE) indicates that current transport mechanisms dominate between thermionic emission (TE) and field emission (FE).

The specific contact resistance $\rho_C (\Omega - cm^2)$ by thermionic field emission (TFE)

is calculated by

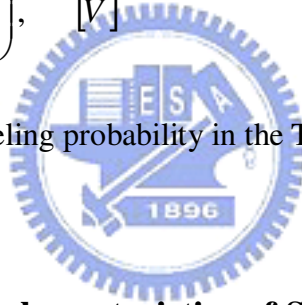
$$\rho_C = \frac{K}{qA^*T} \frac{KT}{\sqrt{\pi q(\phi_B + V_n)E_{00}}} \cosh\left(\frac{E_{00}}{KT}\right) \sqrt{\coth\left(\frac{E_{00}}{KT}\right)} \times \exp\left[\frac{q(\phi_B + V_n)}{E_0} - \frac{qV_n}{KT}\right], \quad [\Omega - cm^2] \quad (2-5)$$

$$E_0 = E_{00} \coth\left(\frac{E_{00}}{KT}\right), \quad [eV] \quad (2-6)$$

$$N_C = 2 \left[\frac{2\pi m^* KT}{h^2} \right]^{\frac{3}{2}}, \quad [cm^{-3}] \quad (2-7)$$

$$V_n = \frac{E_C - E_F}{q} = \frac{KT}{q} \ln\left(\frac{N_C}{N_d}\right), \quad [V] \quad (2-8)$$

where E_0 is a measure of tunneling probability in the TFE region.



2.1.3 Current-voltage characteristics of Schottky contacts

2.1.3.1 Current-voltage (I-V) characteristics by thermionic emission (TE) theory

According to the thermionic emission (TE) theory and neglecting series and shunt resistance, the $I-V$ characteristics in the forward bias for a metal-semiconductor diode, is given by

$$I = I_s \left[\exp\left(\frac{qV}{\eta KT}\right) - 1 \right], \quad [A] \quad (2-11)$$

where V is the voltage drop across the rectifying barrier, η the ideality factor, K the

boltzmann's constant, T the absolute temperature and I_S the saturation current. The saturation current is given by

$$I_S = AA^*T^2 \exp\left(\frac{-q\Phi_B}{KT}\right) = I_{S1} \exp\left(\frac{-q\phi_B}{KT}\right), \quad [A] \quad (2-12)$$

where A^* is the effective Richardson constant, m^* the tunneling effective mass, A the contact area and Φ_B the barrier height at zero bias.

Richardson constant A^* always doesn't follow the value predicted above even when quantum mechanical reflection at the interface and phonon scattering is considered [50]. Richardson constant A^* of the experimental results is much smaller than that of the theoretical calculation, and is caused by presence of a barrier through which the electron must tunnel. On the other hand, the lower Richardson constant A^* is observed due to the decrease of the effective contact area [27], [48]. Published values of Richardson contact A^* are given in Table 2-1.

The barrier height could be obtained from the equation.

$$q\Phi_B = \frac{KT}{q} \ln\left(\frac{AA^*T^2}{I_S}\right), \quad [eV] \quad (2-13)$$

$$\eta = \frac{q}{KT} \frac{\partial V}{\partial(\ln J)} \quad (2-14)$$

2.1.3.2 Current-voltage (I-V) characteristics by thermionic-field emission (TFE) theory

At moderate temperatures and doping levels, thermionic-field emission (TFE) is responsible for current transport, the current-voltage (*I-V*) characteristics in the forward bias is given by [55]

$$J = J_s \exp\left(\frac{V}{E_0}\right) \left[1 - \exp\left(\frac{-qV}{KT}\right)\right] \quad (2-15)$$

At low temperature $\left(\frac{KT}{E_{00}} \ll 1\right)$, $E_0 \cong E_{00}$ so that the slope of graph of

$\ln\left[\frac{J}{1 - \exp\left(\frac{-qV}{KT}\right)}\right]$ versus *V* is independent the temperature for field emission (FE).

At high temperature $\left(\frac{KT}{E_{00}} \gg 1\right)$, E_{00} is slightly greater than KT/q , and the slope could

be written as $q/\eta KT$.

where the ideality factor η is related to E_0 by the relation.

$$\eta = \frac{E_0}{KT} = \frac{E_{00}}{KT} \coth\left(\frac{E_{00}}{KT}\right) \quad (2-16)$$

The reverse current density, J_s , is a complicated function of voltage, temperature, barrier height, and other semiconductor parameters. If

$$KT > \frac{2qE_{00}}{\ln\left[\frac{4(\phi_e - V)}{V_n}\right]}$$

and

$$\frac{\cosh^2\left(\frac{E_{00}}{KT}\right)}{\sinh^3\left(\frac{E_{00}}{KT}\right)} < \frac{2(\phi_e + V_n - V)}{3E_{00}}$$

The reverse saturation current density J_S is reduced to

$$J_S = \frac{A^* T q \sqrt{[\pi E_{00} (\phi_e - V - V_n)]} \times \exp\left[\frac{-qV_n - (\phi_e - V_n)}{KT} - \frac{(\phi_e - V_n)}{E_0}\right]}{K \cosh\left(\frac{qE_{00}}{KT}\right)} \quad (2-17)$$

where $\phi_e (= \phi_{B0} - \Delta\phi_{B0})$ is the effective barrier height. $\Delta\phi_{B0}$ is the barrier lowering at zero bias due to image force, V_n is the energy of the Femi level of the semiconductor with respect to the bottom of the conduction band.

where N_C is the effective density of states near the bottom of the conduction band.

When $\phi_e \gg V_n(\eta - 1)$ and $\phi_e > V + V_n$. The reverse saturation current density equation could be simplified to

$$J_S = \frac{A^* T q \sqrt{[\pi E_{00} (\phi_0 - \Delta\phi_{B0})]} \times \exp\left[\frac{-q(\phi_0 - \Delta\phi_{B0})}{\eta KT}\right]}{K \cosh\left(\frac{qE_{00}}{KT}\right)} \quad (2-18)$$

2.1.3.3 Current-voltage-temperature (I-V-T) characteristics by thermionic emission (TE) theory

For $V \gg KT/q$, Eq.(2-11) can be written as

$$\ln \frac{I}{T^2} = \ln AA^* - \frac{1}{T} \left(\frac{q\phi_{Bn} - V_F}{K} \right)$$

$$Slope = \left(\frac{\frac{V}{\eta} - q\phi_B}{1000K} \right) \quad (2-19)$$

$$q\phi_B = \frac{V}{\eta} - \frac{1000k}{q} \frac{d \left[\ln \left(\frac{I}{T^2} \right) \right]}{d \left(\frac{1000}{T} \right)}$$

where $q(\phi_{Bn} - V_F)$ is the activation energy. Over a limited range of temperature (e.g., $273K < T < 373K$), the value of A^* and ϕ_{Bn} are essentially temperature-independent. The slope of $\ln \frac{I}{T^2}$ versus $\frac{1}{T}$ yields the product of the electrically active area A and the effective Richardson constant A^* for a given forward bias V_F [43].



2.1.3.4 Current-voltage characteristics with series resistance by thermionic emission (TE) theory

The thermionic current-voltage expression of a Schottky barrier diode with series resistance is given by [50]

$$I = I_s \left[\exp \left(\frac{qV - IR_s}{\eta KT} \right) - 1 \right], \quad [A] \quad (2-20)$$

where I_s is the saturation current

$$I_s = AA^* T^2 \exp \left(\frac{-q\phi_B}{KT} \right) = I_{s1} \exp \left(\frac{-q\phi_B}{KT} \right), \quad [A]$$

where A is the diode area, A^* the Richardson's constant, ϕ_B the effective barrier height and η the ideality factor. Eq.(2-20) is expressed as

$$I = I_s \exp\left(\frac{qV}{\eta KT}\right) \left(1 - \exp\left(\frac{-qV}{KT}\right)\right) \quad (2-21)$$

According to Eq.(2-20) are only linear for $V \gg KT/q$, this equation is valid when $IR_s \ll V$. Data plotted on a semi-log plot. However, if R_s is too large and the linear region is too small to provide a reliable value of I_s , the current-voltage characteristics can be deduced by using the Norde function method, and it is given by [56]-[59]

$$F(V) = \frac{V}{2} - \frac{KT}{q} \ln \left[\frac{I(V)}{A A^* T^2} \right] \quad (2-22)$$

where A is the contact area, A^* the effective Richardson constant, The effective Schottky barrier height is given by

$$q\Phi_B = F(V_{min}) + \frac{V_{min}}{2} - \frac{V}{\eta} + \frac{IR_s}{\eta} \quad [\text{eV}] \quad (2-23)$$

where $F(V_{min})$ is the minimum value of $F(V)$ and V_{min} is the corresponding voltage.

However, the effective barrier height can't be analyzed by Norde function method due to neglected series resistance effects in this study.

2.1.4 Capacitance-voltage (C-V) characteristics of Schottky contact

Capacitance-voltage (C-V) measurements are done to determine depletion region

in the Schottky barrier. Capacitance was measured by applying a dc between $-1V$ to $1V$ with $1M$ Hz. The capacitance voltage relationship for Schottky barrier with a negligible oxide layer between the metal and the semiconductor is given by [29]

$$C^2 = S^2 \left[\frac{\varepsilon_s q N_d}{2 \left(V_{bi} - V - \frac{KT}{q} \right)} \right], \quad [F^2] \quad (2-24)$$

where S the diode cross-sectional area, ε_s the permittivity of the semiconductor $\left(\frac{\varepsilon_s}{\varepsilon_0} |_{GaN} = 9.5 \right)$, and V the applied bias voltage. The effective carrier concentration is

given by

$$N_d = \frac{-2}{S^2 \varepsilon_s q} \frac{d(1/C^2)}{dV}, \quad [cm^{-3}] \quad (2-25)$$

From the $1/C^2$ and the applied bias voltage V , the ionized donor density N_d and the built in potential V_{bi} are determined. Then the x intercept V_0 (at $1/C^2=0$) is related to the built in potential via $V_0 = V_{bi} - \frac{KT}{q}$.

If the barrier height is assumed not to depend on the electric field in the junction (i.e., neglecting the effect of an imaging force), then the effective Schottky barrier height is given by

$$q\phi_B = q(V_{bi} + V_n), \quad [eV] \quad (2-26)$$

$$V_n = \frac{E_C - E_F}{q} = \frac{KT}{q} \ln \left(\frac{N_C}{N_d} \right), \quad [V]$$

where N_C the effective density of conduction band states

$$N_C = 2 \left[\frac{2\pi m^* KT}{h^2} \right]^{\frac{3}{2}}, \quad [cm^{-3}]$$

where m^* the tunneling effective mass and h the Planck's constant.

2.1.5 Capacitance-frequency (C - f) characteristics of Schottky contact with interfacial states

With the device capacitance and conductance measurement, the junction capacitance (C) is done according to the series resistance correction from the relation [60]-[63]

$$C = C_M / [(1 - R_s \cdot G_M)^2 + (2\pi \cdot f \cdot R_s \cdot C_M)^2], \quad (2-27)$$

where C_M and G_M are the measured device capacitance and conductance with parallel model, R_s is the series resistance and f is the frequency.

The interfacial states capacitance C_p is obtained from [63], [64]

$$C_p = C - C_{sc}, \quad (2-28)$$

For the Schottky contact with interfacial states, the junction capacitance, C , is the sum of the space charge capacitance, C_{sc} , and the interfacial states capacitance, C_p . The space charge capacitance, C_{sc} , can be obtained by extrapolating the linear portion of the high frequency (1MHz) $1/C^2 - V$ plots under reverse bias [63]. The interfacial states capacitance, depending on the interfacial states density N_{ss} with the relaxation time τ , is given by [61]-[65]

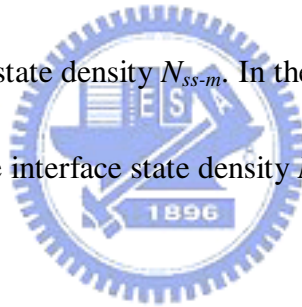
$$C_p = qAN_{ss} \text{arc tan}(\omega\tau) / \omega\tau, \quad (2-29)$$

where q is the electron charge, A the contact area and $\omega (= 2\pi \cdot f)$ the angular frequency. According to Eq.(2-29), there is one plateau region in the C_p -frequency

relation with certain relaxation time. Yet, in my experiments, the data manifests two plateau regions in the frequency range around 100Hz to 2KHz and 100KHz to 300KHz. There may be different types of state in the semiconductor. This interfacial states capacitance can be considered to be the overall effects of different kinds of interfacial centers [66]-[68]. We can do the best fitting procedure in different frequency ranges [62]. For each interfacial center, the interfacial states capacitance can be achieved by

$$C_{p-i} = C_p - C_{p-i-0}, \quad (2-30)$$

where i represent the i -type interfacial state ($i = m, f$). C_{p-i-0} is the height of the plateaus region in the C_p -frequency relation. In the frequency range 100Hz to 2KHz, the attracted m -type interface state density N_{ss-m} . In the frequency range from 100KHz to 1MHz, the associated f -type interface state density N_{ss-f} .

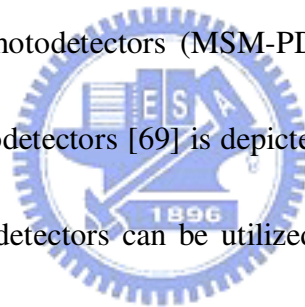


2.2 Theory and physical characteristics of photodetector

2.2.1 Introduction

Semiconductor photodetectors and photon sources are inverse devices. Photodetectors can convert an input photon flux to an output electric current, therefore it can convert optical power into electrical power. The characteristics of photodetectors depend on the optical energy which is absorbed in a semiconductor and generate excess electron-hole pairs to produce photocurrent. There are two classifications of photodetectors that one is photoconductive and the other is

photovoltaic. As an electrical field is applied to the semiconductor, the photoconductive detector can increase conductivity and leads to decrease resistance of the semiconductor. As the electrons and the holes are separated by the electrical field at the pn -junction without any electric bias, and an electromotive force between the p - and n -side semiconductors is generated, the photovoltaic has a pn -junction in the illuminated area. The photovoltaic detector can generate photo-carriers due to electrons and holes are separated by electrical field. The most of usual type of photovoltaic detector is the $p-n$, $p-i-n$, Schottky barrier photodetectors (SB-PDs) and metal-semiconductor-metal photodetectors (MSM-PDs). The schematic structure of different semiconductor photodetectors [69] is depicted in Fig.2-4. There are two key issues why photoconductive detectors can be utilized. One is internal gain, and the other one is fabrication simplicity. However, its disadvantages are high dark or leakage current and very slowly when fabricated using GaN-based material. Schottky barrier photodetectors (SB-PDs) and metal-semiconductor-metal photodetectors (MSM-PDs) are the fastest detector, but must face higher dark or leakage current due to lower barrier height observed and lower efficiency due to narrow space charge region, combined with the short diffusion lengths. The $p-n$ or $p-i-n$ photodetectors has lower dark or leakage current and higher rejection ratio.



2.2.2 Metal-semiconductor-metal photodetectors (MSM-PDs)

2.2.2.1 Geometrical structure and physical characteristics

A metal-semiconductor-metal photodetector (MSM-PDs) can be utilized as a high efficiency photogenerated diode. The MSM-PD is an excellent candidate for fabrication simplicity, geometrical convenience, only a single dopant bulk of the semiconductor, high efficiency and high speed. The MSM-PDs with interdigitated electrodes have planar structures in contrast with the other photodetector as shown in Fig.2-5. The MSM-PDs for geometry consideration consists of finger width, length and spacing of interdigitated electrodes. The MSM-PDs optical and electrical characteristics depend on these parameters such as responsivity and leakage current. The response speed is limited by transit time and RC time due to finger width, length and spacing of interdigitated electrodes. In generally, as the finger spacing decreasing, the carrier transit time reduced to lead response time increasing. However, RC time will be increasing due to space charge capacitance effect by decreasing finger spacing to lead response time decreasing. The competition between transit time and RC time depend on the finger spacing of interdigitated electrodes. The planar interdigitated electrodes MSM-PDs which is equivalent to a back-to back pair of Schottky diodes consists of a semiconductor and metal electrodes. The equivalent structure of MSM-PDs is shown in Fig.2-6.

When photons are absorbed by a semiconductor material, photo-carriers are

generated by optical absorption processes, which is by band to band transitions or by band to impurity level transitions. As light fall on the bulk of semiconductor, the photon energy ($h\nu$) dominates that the photons absorbed or propagated through the semiconductor. If photon energy is more than bandgap energy, the photon can interact with a valence electron and excite the electron into the conduction band. The electrons in the conduction band and the holes in the valence band can be formed, thus the photo-carriers are generated by this interaction, this is dominated by band to band transitions as shown in Fig.2-7 (a). The detailed illustration for optical absorption processes in direct band-gap semiconductor is indicated in Fig.2-7. In contrast, the band to impurity level transitions includes acceptor level to conduction band, valence band to donor level, acceptor level to donor level, donor level to conduction level and valence band to acceptor level transitions. If the photon energy is less than bandgap energy (E_g), the photons are not absorbed. Light with fallen on the bulk of semiconductor may propagate through the semiconductor and semiconductor appear to be transparent. However, as light with a photon energy is lower than for with bandgap energy, the electrons can excite from a deep level to the conduction band by these impurity levels, thus its processes or transitions will contribute to photocurrent. The schematic photoexcitation processes is shown in Fig.2-8.



To analyze and defined MSM-PDs characteristics, the electrical and optical

absorption properties are employed. The dark or leakage current for MSM-PDs or Schottky barrier photodetectors (SB-PDs) depends on the barrier height and surface states. Because of the current transport mechanism of MSM-PDs or SB-PDs is dominated by majority carrier, the larger dark or leakage current will be observed. It is different that the $p-n$ or $p-i-n$ type photodetectors due to minority carrier dominated. As a reason, why dark or leakage current for MSM-PDs is greater than that for $p-n$ or $p-i-n$ type PDs. The total current consists of thermionic emission current over the Schottky barrier region and generation-recombination current in the space charge region. As above-mentioned discussion, thermionic emission current can be defined by Eq.(2-11) and Eq.(2-12).

$$J_{th} = A^* T^2 \exp\left(\frac{-q\Phi_B}{KT}\right) \left[\exp\left(\frac{qV}{\eta KT}\right) - 1 \right], \quad [A] \quad (2-31)$$

The generation-recombination current is expressed by

$$J_{gr} = \frac{qn_i}{\tau_0} \sqrt{\frac{2\epsilon_s}{qN_d} (V_{bi} - V)} \left(e^{\frac{qV}{2KT}} - 1 \right) \quad (2-32)$$

Where n_i is the intrinsic concentration, N_d the dopant concentration, V_{bi} the built in potential and V the applied bias voltage.

The space charge region width (W) for n -type semiconductor theory model is defined by

$$W = \sqrt{\frac{2\epsilon_s (V_{bi} - V)}{qN_d}} \quad (2-33)$$

Then, substituting Eq.(2-33) into is given by

$$J_{gr} = \frac{qn_i W}{2\tau_0} \left(e^{q\frac{V}{2KT}} - 1 \right) \quad (2-34)$$

where τ_0 is life time of minority carrier in the space charge region. The total dark current is expressed by

$$J_{total} = J_{th} + J_{gr} \quad (2-35)$$

2.2.2.2 Responsivity and quantum efficiency

The responsivity of an MSM-PDs which is ratio of the actual photocurrent to the incident optical power is defined by

$$R = \frac{I_{ph}}{P_{out}} = \frac{\eta_{ext} q}{h\nu} \Gamma_G \quad (2-36)$$



where I_{ph} is the actual photocurrent, η_{ext} the external quantum efficiency, h the Planck's constant, ν the frequency of the light and Γ_G the internal gain. The measured current (I_p) with illuminated by light is sum of actual photocurrent (I_{ph}) and dark current (I_d) without illuminated by light, and is written as

$$I_p = I_{ph} + I_d \quad (2-37)$$

As semiconductor in the thermal equilibrium state are illuminated with light having a photon energy ($E=h\nu$) higher than the bandgap energy (E_g), electrons are elevated from the valance band to the conduction band and holes are stayed the

valance band. The excited electrons stay in the conduction band for a certain time and then return to the valance band to keep thermal equilibrium. As the electrons return to the valance band, the recombination processes which emitted a photon will be take place. The cutoff wavelength of this photon in direct bandgap semiconductor is written as

$$\lambda_c = \frac{c}{\nu} = \frac{hc}{E_g} = \frac{1.24}{E_g} \quad [\mu m] \quad (2-38)$$

Substituting Eq.(2-38) to Eq.(2-36) is given as

$$R = \frac{\eta_{ext} q \lambda_c [um]}{1.24} \Gamma_G \quad (2-39)$$

Under light incidence, a single photon incident on the semiconductor generates a photocarrier pair that contributed to the photocurrent. The quantum efficiency is defined by the ratio of the flux of generated electron-hole pairs that contributed to the detector current to the flux of incident photons, and is written as

$$\begin{aligned} \eta_{ext} &= \frac{\text{number of electron - hole pairs comtributing to photo - induced current}}{\text{number of incident photons}} \\ &= \frac{I_{photo} / q}{P_{inc} / h\nu} \times 100\% \\ \eta_{ext} &= \left[\frac{s}{s+w} \right] (1-r) [1 - e^{-\alpha d}] \end{aligned} \quad (2-40)$$

where s is the finger spacing for MSM-PDs, w the finger width, r the optical power of

reflectance at the surface(= $\left(\frac{n_1 - n_2}{n_1 + n_2} \right)^2$, $n_{1|GaN} = 2.5$, $n_{2|air} = 1$, $r = 0.18$), α the

absorption coefficient of material (GaN in this case as shown in Fig.2-9 and d the absorption depth.

2.2.2.3 Shockley-Read-Hall Theory of recombination and internal gain

When light having a high energy photons are incident on the semiconductor, the electrons in the valance band may be excited into the conduction band (excess electrons) and the holes may be leave in the valance band (excess holes), thus an electron-hole pair is generated. The concentration of electrons in the conduction band and holes in the valance band by generated the excess electrons and holes are more than that by thermal equilibration, and are given by

$$\begin{aligned} n &= n_0 + \delta n \\ \text{and} & \\ p &= p_0 + \delta p \end{aligned} \tag{2-41}$$

where n_0 and p_0 are the thermal equilibration concentrations, and δn and δp are the excess electrons and holes concentration by applying an external force such as illuminated processes. The current voltage characteristics with/without illumination, structure and band diagram for $p-i-n$ PDs under operated reverse bias is shown in Fig. 2-10 and Fig.2-11, respectively. The net of change in the electron concentration in the thermal equilibration is given by

$$\frac{d[\delta n(t)]}{dt} = -\alpha_r \delta n(t) [(n_0 + p_0) + \delta n(t)] \quad (2-42)$$

where α_r is parameter.

For n -type semiconductor under low-level injection, thereby

$$n_0 \gg p_0, \quad \delta n(t) \ll n_0$$

The decay of minority carrier holes take place as minority carrier lifetime is written as

$$\tau_{p0} = \frac{1}{\alpha_r n_0} \quad (2-44)$$

The excess minority carrier concentration is defined by

$$\begin{aligned} \delta p(t) &= \delta p(0) e^{-\alpha_r n_0 t} \\ &= \delta p(0) e^{-\frac{t}{\tau_{p0}}} \end{aligned} \quad (2-43)$$

The recombination rate of the majority carrier electrons will be the same as that of minority carrier holes, and is defined by

$$R_{n'} = R_{p'} = \frac{\delta n(t)}{\tau_{p0}} \quad (2-45)$$

According to Shockley-Read-Hall theory, an allowed energy state donates a trap, within the forbidden bandgap may act as a recombination center which exists at an energy E_t within the bandgap. The capturing probability of recombination center and capture cross sections for electrons are equal to that for holes.

If the trap energy E_t coincided with the Fermi energy E_F , an electron concentration (n') is exist in the conduction band, and is defined by

$$n' = N_c \exp\left[\frac{-(E_c - E_t)}{kt}\right] \quad (2-46)$$

Thus,

As the recombination center at $E=E_t$, the recombination rate of electrons and holes is given by

$$R_n = R_p = \frac{C_n C_p N_t (np - n_i^2)}{C_n (n + n') + C_p (p + p')} \quad (2-47)$$

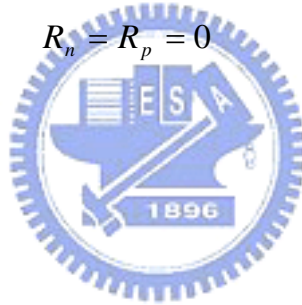
where N_t is the total concentration of trapping centers.

For thermal equilibration, thereby

$$np = n_0 p_0 = n_i^2, \quad R_n = R_p = 0$$

Eq.(2-47) can simplify by

$$R = \frac{\delta n}{\tau} \quad (2-48)$$



For n -type semiconductor and low injection, thereby

$$n_0 \gg p_0, \quad n_0 \gg \delta p, \quad n_0 \gg n', \quad n_0 \gg p'$$

Eq.(2-47) can simplify by

$$R = C_p N_t \delta p \quad (2-49)$$

To combine with Eq.(2-48) and Eq.(2-49) can extract to minority carrier holes lifetime is written as

$$\tau_{p0} = \frac{1}{C_p N_t} \quad (2-50)$$

The excess minority carrier lifetime is inversely proportional to the density of trap

states by Eq.(2-50). The density of traps at the surface is higher than in the bulk, the excess minority carrier lifetime at the surface will be lower than the corresponding lifetime in the bulk.

For the photoconductive detector as a resistor comprises a bulk of semiconductor by applying bias at the ohmic contact utilized as shown in Fig.2-12. As a semiconductor is illuminated by light having a photon energy larger than its bandgap energy, the light is absorbed in the semiconductor and the electron-hole pairs are generated. If an electrical field is applied to the semiconductor, photoinduced carriers lead to decrease resistance of the semiconductor. The photodetectors with internal gain is attributed to the excess electrons in the conduction band and excess the holes in the valance band in addition to the thermal equilibration concentrations as the external excitation is applied to the semiconductor. The recombination lifetime and transit time are key issue for internal gain.

As steady state, the carrier generation rate must be equal to the recombination rate. If the device absorption depth (D) is greater than the light penetration depth ($1/\alpha$). The total steady-state generation rate of carriers per unit volume is written as

$$G = \frac{n}{\tau} = \frac{\eta_{ext} \left(\frac{P_{inc}}{h\nu} \right)}{WLD} \quad (2-51)$$

where n is the number of carriers in the thermal equilibration, τ the carrier lifetime, η the quantum efficiency, P_{inc} the incident optical power, $h\nu$ the photon energy, L the

finger length, W the finger width and D the device absorption depth. The measured photocurrent (I_p) is given by substituting n in Eq.(2-51) into Eq.(2-52)

$$\begin{aligned}
 I_p &= (\sigma)EWD \\
 &= (qn\mu_n)EWD \\
 &= q\mu_n EWD \left(\frac{\tau \eta_{ext} \left(\frac{P_{inc}}{h\nu} \right)}{WLD} \right) \\
 &= q \left(\eta_{ext} \frac{P_{inc}}{h\nu} \right) \left(\frac{\tau \mu_n E}{L} \right) \\
 &= q \left(\eta_{ext} \frac{P_{inc}}{h\nu} \right) \Gamma_G
 \end{aligned} \tag{2-52}$$

Simplifying and substituting Eq.(2-40) into Eq.(2-52), the responsivity can be given

with internal gain by

$$\begin{aligned}
 R &= \frac{I_p}{P_{inc}} \\
 &= \frac{q\eta_{ext}}{h\nu} \Gamma_G \\
 &= \left[\frac{s}{s+w} \right] (1-r) [1 - e^{-\alpha d}] \frac{q}{h\nu} \Gamma_G
 \end{aligned} \tag{2-53}$$



The actual photocurrent is defined by

$$\begin{aligned}
 I_{ph} &\equiv q \left(\eta_{ext} \frac{P_{inc}}{h\nu} \right) \\
 &\equiv q\eta_{ext} \phi_0
 \end{aligned} \tag{2-54}$$

where Φ_0 is photon flux (W/cm^2)

$$\phi_0 \equiv \frac{P_{inc}}{h\nu}$$

The internal gain is given by

$$\Gamma_G = \frac{I_p}{I_{ph}} = \frac{\tau \mu_n E}{L} = \frac{\tau}{t_r} = \frac{\tau \mu_n V}{L^2} \quad (2-55)$$

$$t_r = \frac{L}{V} = \frac{L}{\mu_n E} \quad (2-56)$$

Substituting Eq.(2-55) into Eq.(2-53), the relationship between responsivity and applied bias is linear, and is expressed by

$$\begin{aligned} R &= \left[\frac{s}{s+w} \right] (1-r) [1 - e^{-\alpha d}] \frac{q}{h\nu} \Gamma_G \\ &= \left[\frac{s}{s+w} \right] (1-r) [1 - e^{-\alpha d}] \frac{q}{h\nu} \frac{\tau \mu_n V}{L^2} \\ &= \left[\frac{s}{s+w} \right] (1-r) [1 - e^{-\alpha d}] \frac{q \lambda_c [\mu m]}{1.24} \frac{\tau \mu_n V}{L^2} \end{aligned} \quad (2-57)$$

where t_r is the carrier transit time and E the electric field ($=V/L$). The internal gain and responsivity are indicated as a function of carrier mobility, interdigital electrodes spacing for MSM-PDs (L), carrier lifetime (τ) and transit time (t_r). Larger internal gain with small transit time which is attributed to higher interfacial states density by surface defects will be expected. The response time depends on the transit time. In order to extract higher internal gain, the fast response time must be requested by increasing reverse bias to enhance electric field, greater carrier mobility and reducing finger spacing for MSM-PDs.

2.2.3 *p-i-n* junction photodetector

The *p-i-n* photodetectors (*p-i-n* PDs) convert light power into electrical power by applying reverse bias. The *p-i-n* PDs are most common of photodetectors due to having thicker absorption region by intrinsic layer and lower dark or leakage current. The schematic *p-i-n* PDs circuit and current-voltage characteristics are shown in Fig.2-10. As incident photon energy is more than bandgap energy, the light are absorbed and photocurrent is generated as shown in Fig.2-10. In contrast, the current of PDs without illuminated light by applying reverse bias donates dark current. In order to understand *p-i-n* PDs characteristics, the current-voltage characteristics are employed. Fig.2-11 indicates schematic of *p-i-n* PDs structure and photon absorption. When *p-i-n* PDs are operated by applying reverse bias and are illuminated by photon energy ($h\nu$) higher than bandgap energy E_g , the photo-induced current and excess carrier can be generated in the depletion region. The reverse bias current density under steady-state conditions is sum of reverse saturation current density and generation current density given by

$$J_R = J_s + J_{gen} \quad (2-58)$$

Fig.2-13 indicates the photogenerated current density and is given by

$$J_{gen} = q \int_0^W G(x) dx \quad (2-59)$$

Where $G(x)$ is photon flux and is shown as a function of absorption depth in the

semiconductor.

$$\begin{aligned}\phi_0 &= (1-r) \frac{P_{inc}}{h\nu} \\ G(x) &= \phi_0 \alpha e^{-\alpha x} \\ &= (1-r) \frac{P_{inc}}{h\nu} \alpha e^{-\alpha x}\end{aligned}\tag{2-60}$$

where R is the optical power of reflectance at the surface. Substituting Eq.(2-60) into

Eq.(2-59) is given by

$$\begin{aligned}J_{gen} &= q \int_0^w \phi_0 \alpha e^{-\alpha x} dx \\ &= q \phi_0 (1 - e^{-\alpha w}) \\ &= q (1-r) \frac{P_{inc}}{h\nu} (1 - e^{-\alpha w})\end{aligned}\tag{2-61}$$

According to Shockley-Read-Hall recombination theory, the recombination rate of excess carrier is given by

$$R = \frac{C_n C_p N_t (np - n_i^2)}{C_n (n + \delta n) + C_p (p + \delta p)}\tag{2-62}$$

where C_n is electron capture cross section, C_p is hole capture cross section, n the electron concentration and p the hole concentration.

Under reverse bias, the recombination rate can simplify from Eq.(2-62)

$$R = \frac{-C_n C_p N_t n_i^2}{C_n \delta n + C_p \delta p}\tag{2-63}$$

If the traps level (E_t) occurs at the intrinsic Fermi level, the recombination rate can simplify by

$$R = \frac{-n_i}{\frac{1}{N_t C_p} + \frac{1}{N_t C_n}} \quad (2-64)$$

By using the lifetime of electron and hole is defined by

$$\begin{aligned} \tau_{n0} &= \frac{1}{N_t C_n} \\ \tau_{p0} &= \frac{1}{N_t C_p} \\ \tau_0 &= \frac{\tau_{n0} + \tau_{p0}}{2} \end{aligned} \quad (2-65)$$

Substituting Eq.(2-65) into Eq.(2-64) is given by

$$R = -G = \frac{-ni}{2\tau_0} \quad (2-66)$$

Thus Eq.(2-59) is simplify by

$$\begin{aligned} J_{gen} &= \frac{qn_i W}{2\tau_0} \\ J_{rec} &= \frac{qn_i W}{2\tau_0} e^{\left(\frac{eV_a}{2kT}\right)} \end{aligned} \quad (2-67)$$



On the other hand, the forward bias current density is sum of diffusion current density

and recombination current density is given by

$$J_F = J_{diff} + J_{rec} \quad (2-68)$$

When light illuminated on the semiconductor, the excess carriers are generated and

increased the minority carrier concentration by Eq.(2-41) is given by

$$\begin{aligned}\delta p_n(x) &= p_{n0} \left[e^{\left(\frac{qV_a}{kT}\right)} - 1 \right] e^{\left(\frac{x_n - x}{L_p}\right)} \\ \delta n_p(x) &= n_{p0} \left[e^{\left(\frac{qV_a}{kT}\right)} - 1 \right] e^{\left(\frac{x_p - x}{L_n}\right)}\end{aligned}\tag{2-69}$$

The minority carrier hole diffusion current density is given by

$$\begin{aligned}J_p(x_n) &= -qD_p \frac{d(\delta p_n(x))}{dx} \Big|_{x=x_n} \\ J_p(x_n) &= \frac{qD_p p_{n0}}{L_p} \left[e^{\left(\frac{qV_a}{kT}\right)} - 1 \right]\end{aligned}\tag{2-70}$$

The minority carrier electron diffusion current density is given by

$$\begin{aligned}J_n(-x_p) &= -qD_n \frac{d(\delta n_p(x))}{dx} \Big|_{x=x_p} \\ J_n(-x_p) &= \frac{qD_n n_{p0}}{L_n} \left[e^{\left(\frac{qV_a}{kT}\right)} - 1 \right]\end{aligned}\tag{2-71}$$

The forward bias current density is given by

$$\begin{aligned}J_F &= J_p(x_n) + J_n(-x_p) \\ &= \left[\frac{qD_p p_{n0}}{L_p} + \frac{qD_n n_{p0}}{L_n} \right] \left[e^{\left(\frac{qV_a}{kT}\right)} - 1 \right] \\ &= J_s \left[e^{\left(\frac{qV_a}{kT}\right)} - 1 \right]\end{aligned}\tag{2-72}$$

Where J_s is reverse saturation current.

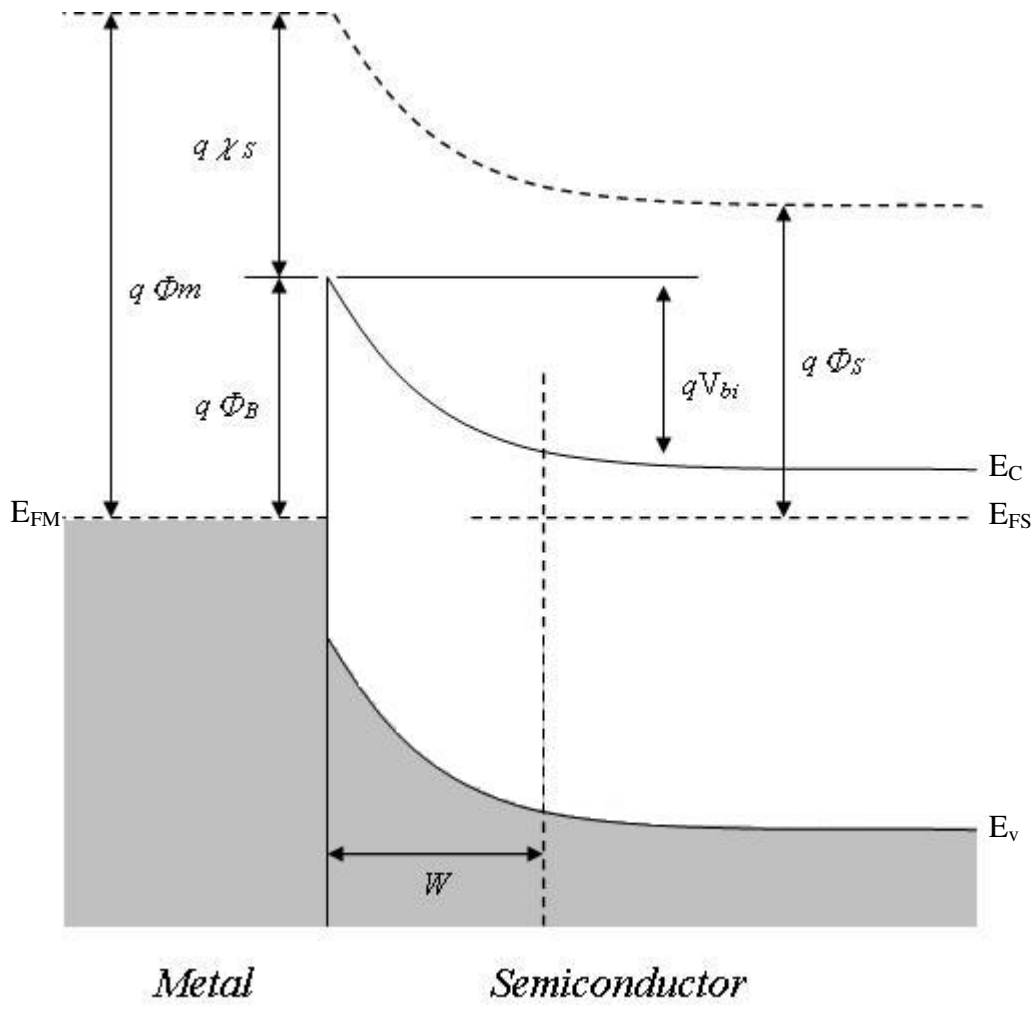


Fig. 2-1 Schematic energy band diagram of metal-semiconductor junction

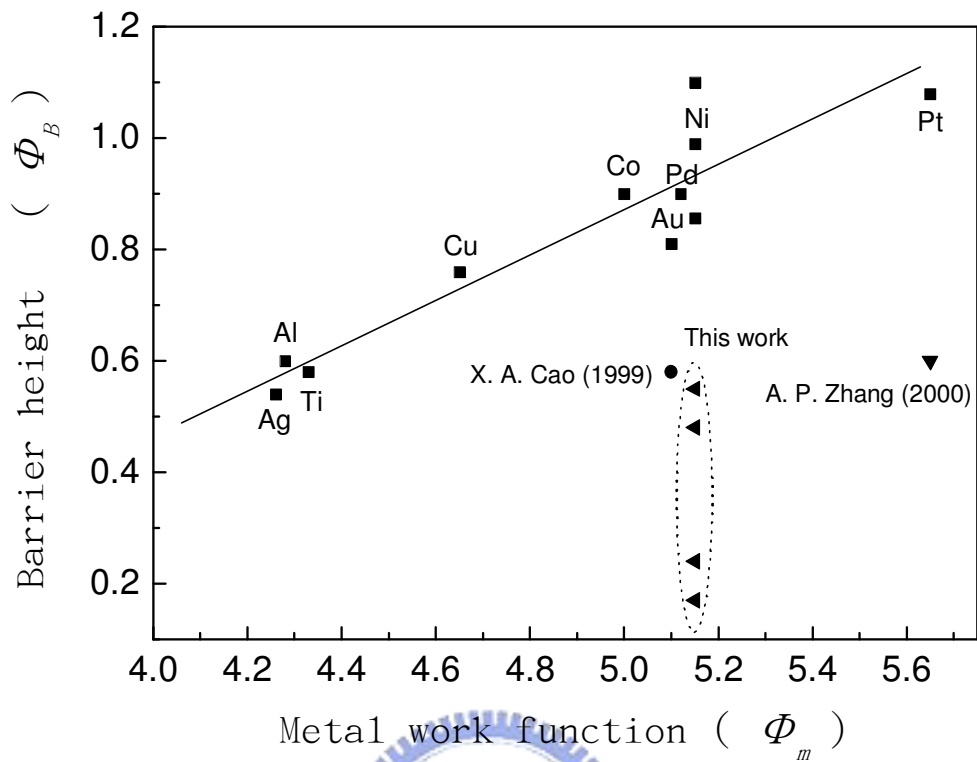


Fig. 2-2 Barrier height is depicted as a function of the metal work function and surface treatment. The results of this work are compared to that of other authors.

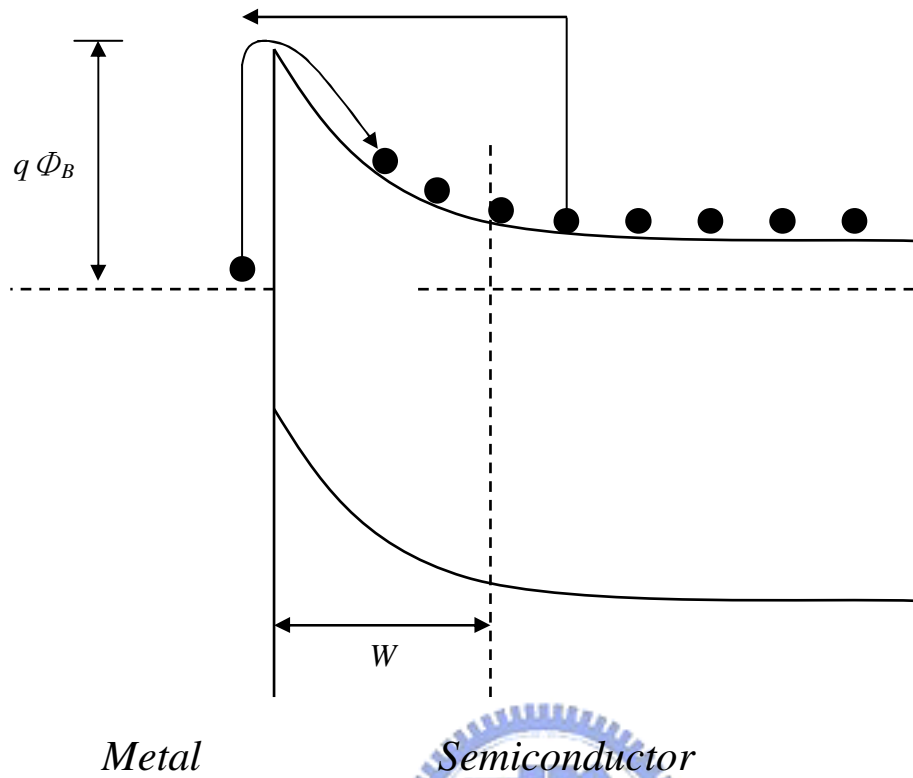


Fig. 2-3(a) Schematic description of the thermionic emission mechanism in *n*-type semiconductor

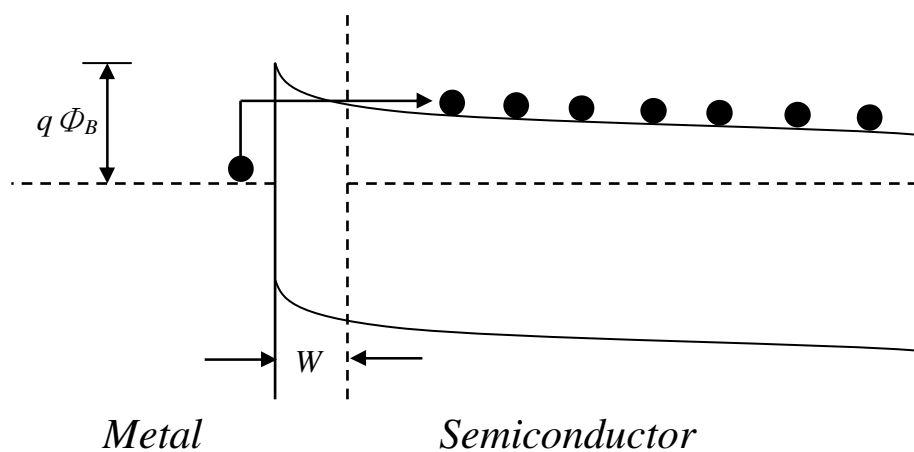
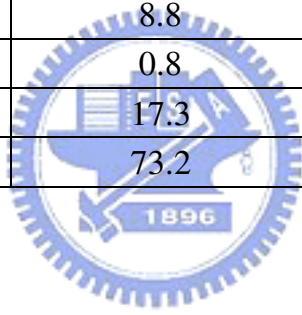


Fig. 2-3(b) Schematic description of the tunneling mechanisms in *n*-type semiconductor

Table 2-1 Experimental Richardson constant A^* data

Semiconductor	A^* ($A/cm^2 \cdot K^2$)	Reference
<i>n</i> -Si	112(\pm 6)	[49]
<i>p</i> -Si	32(\pm 2)	[49]
<i>n</i> -GaAs	4~8	[49]
<i>n</i> -GaAs	0.41(\pm 0.15)	[49]
<i>p</i> -GaAs	7(\pm 1.5)	[49]
<i>n</i> -InP	10.7	[49]
Au/GaN	0.006	[53]
Pt/GaN	6.61	[53]
Pd/GaN	0.44	[53]
Ni/GaN	0.11	[53]
Ag/GaN	1.5	[48]
Cu/GaN	2.2	[48]
Co/GaN	7.9	[48]
Au/GaN	8.8	[48]
Pd/GaN	0.8	[48]
Ni/GaN	17.3	[48]
Pt/GaN	73.2	[48]



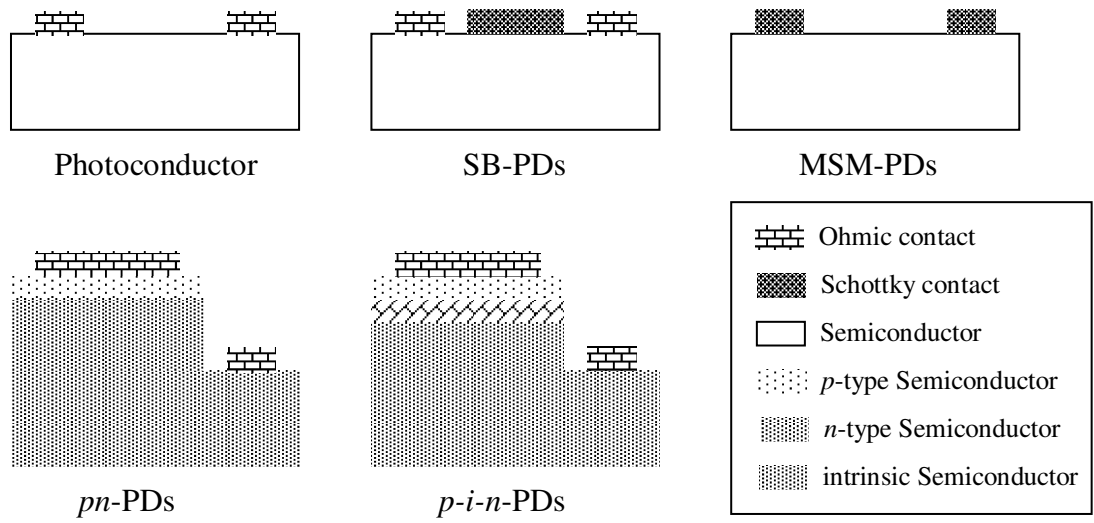


Fig. 2-4 Schematic structure of different type photodetectors



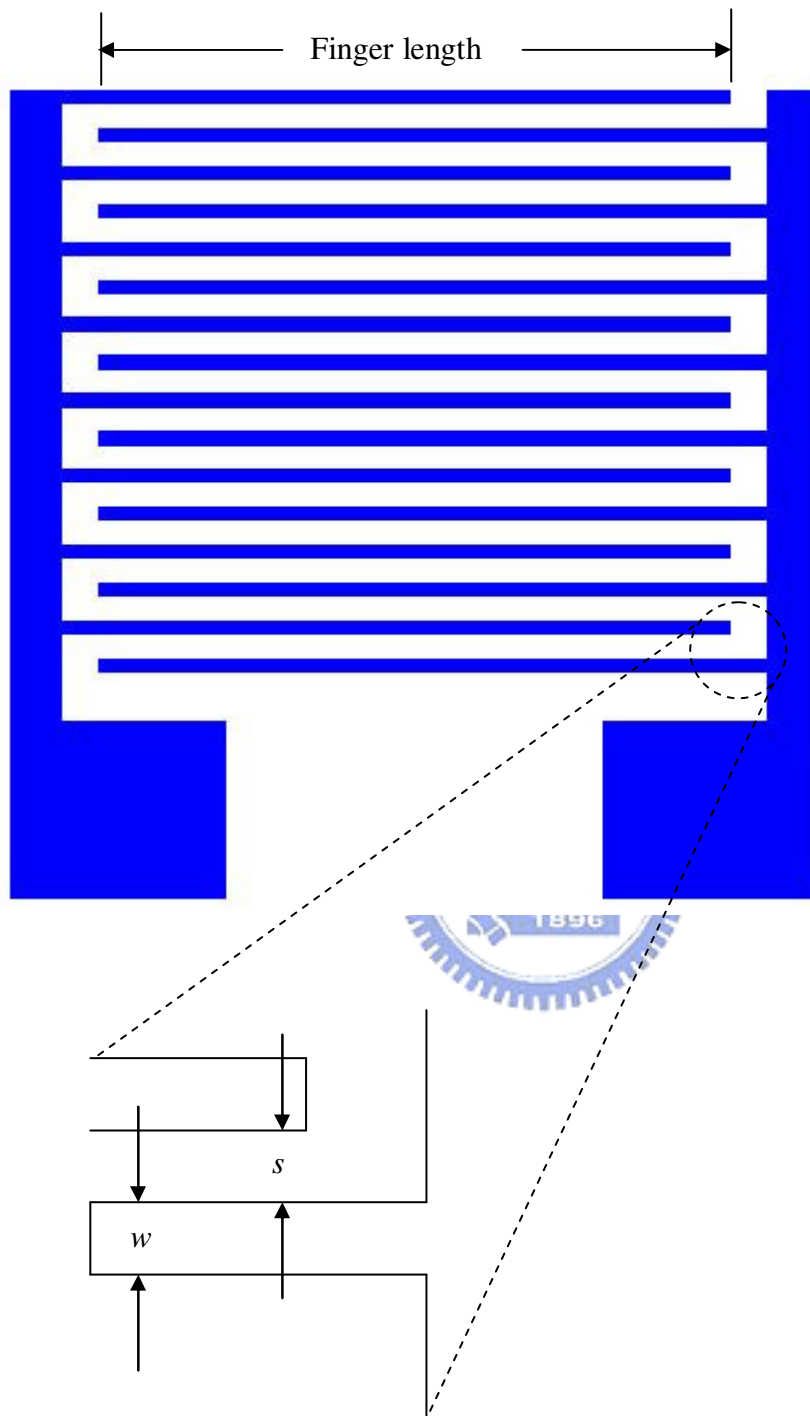


Fig. 2-5 MSM-PDs with interdigitated electrodes by planar structures

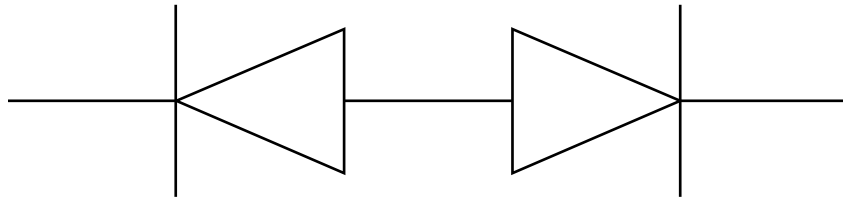


Fig. 2-6 Equivalent metal-semiconductor-metal photodetectors (MSM-PDs)

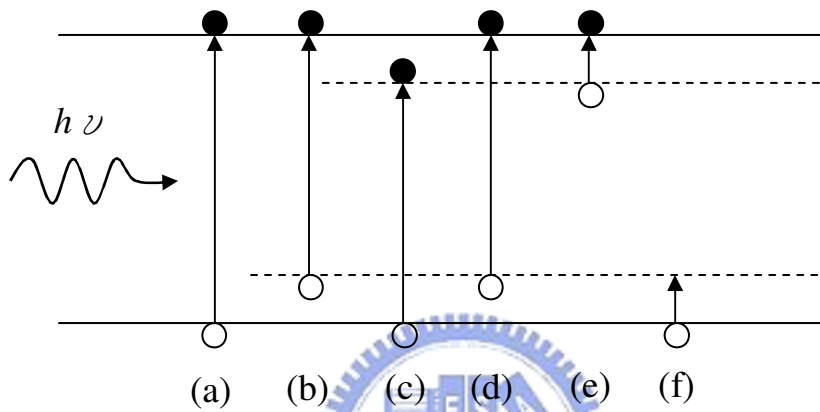


Fig. 2-7 Optical absorption processes in direct band-gap semiconductor. (a) band to band, (b) acceptor level to conduction band, (c) valence band to donor level, (d) acceptor level to donor level, (e) donor level to conduction level and (f) valence band to acceptor level.

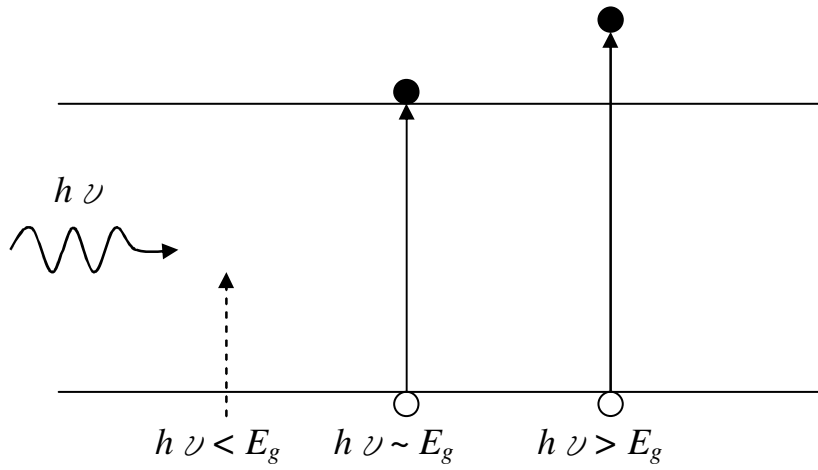


Fig. 2-8 Schematic photoexcitation processes

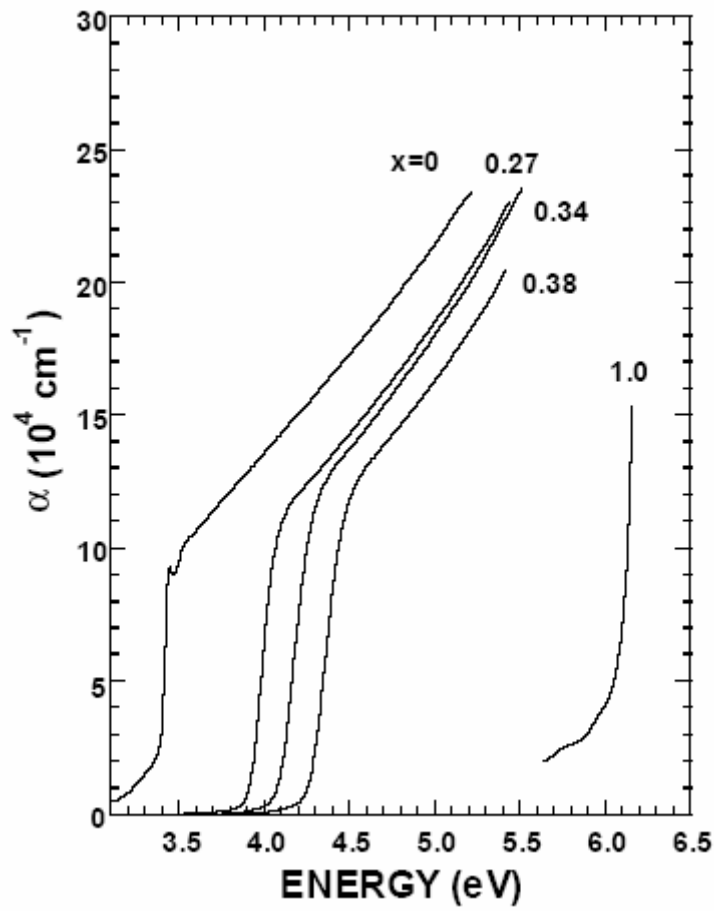


Fig. 2-9 Absorption coefficient for $\text{Al}_x\text{Ga}_{1-x}\text{N}$ -based material

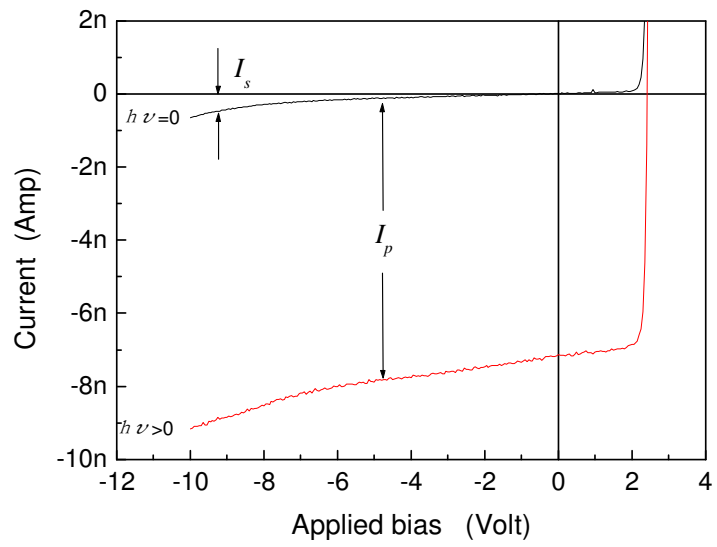


Fig. 2-10 Electrical characteristics for *p-i-n* photodetectors under reverse bias



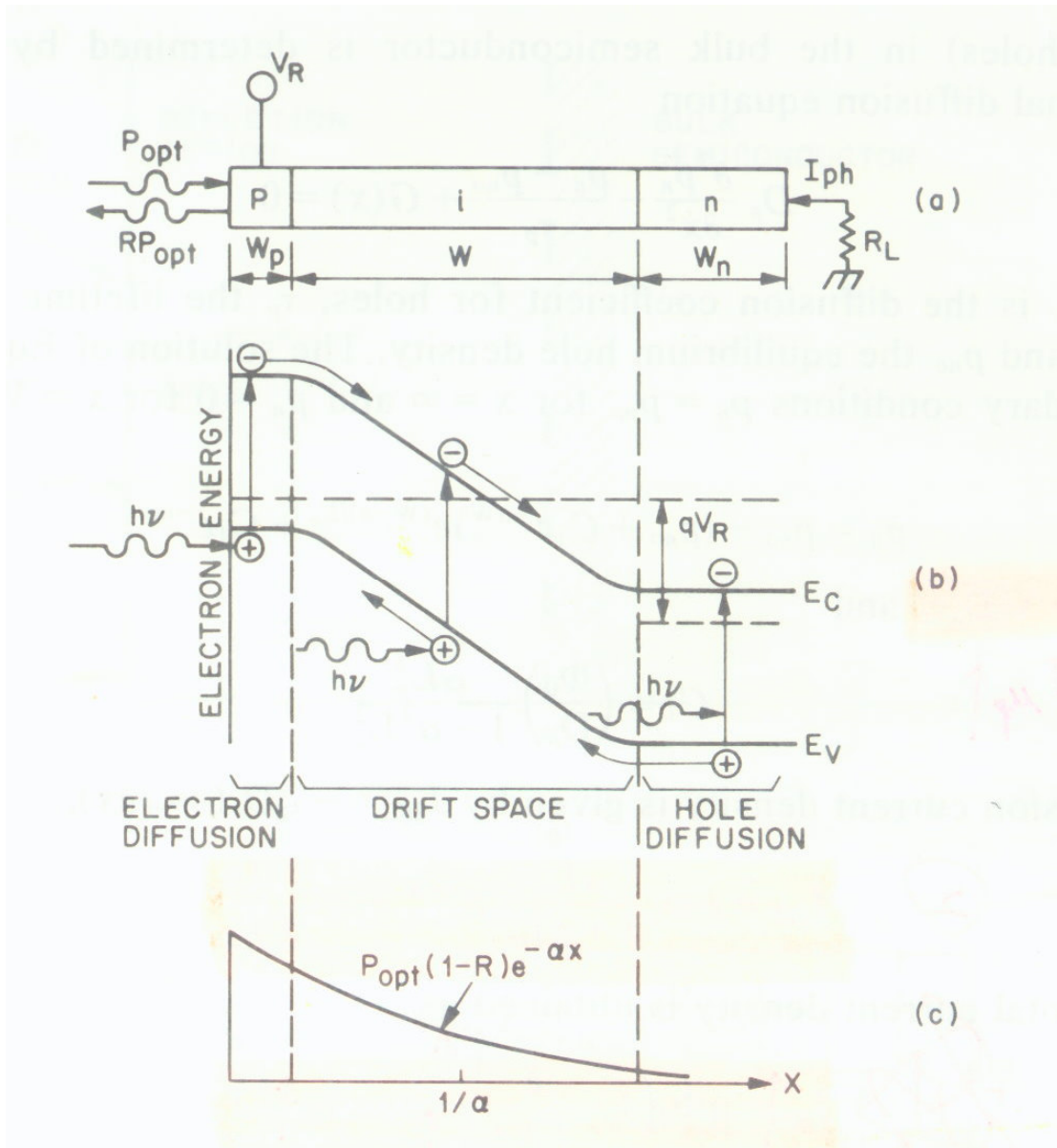


Fig. 2-11 (a) Schematic structure (b) band diagram (c) absorption process of photodetectors under operated reverse bias

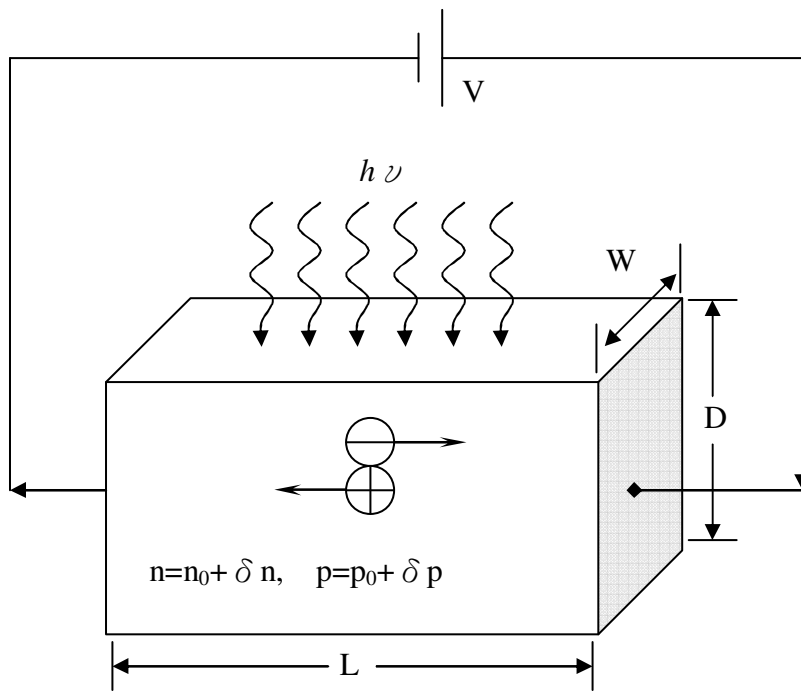


Fig. 2-12 A photoconductive detector with an electrical field is applied to the semiconductor, and the photo-carriers are generated in response to the applied bias voltage.

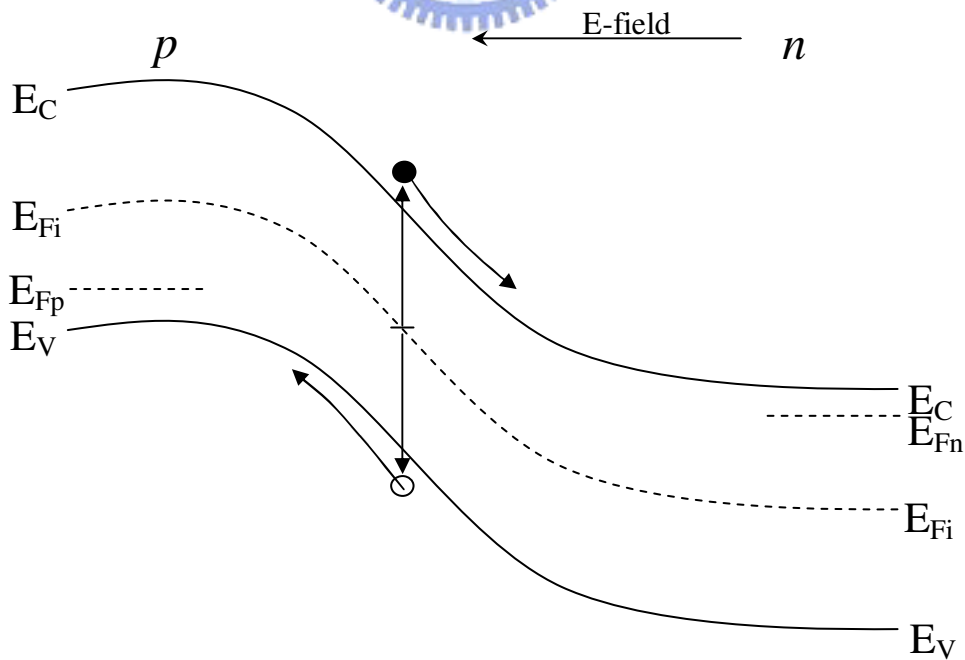


Fig. 2-13 Generation process of photodetectors under reverse bias voltage

Chapter 3 Interfacial states effects and characteristics of Schottky diodes

3.1 Introduction

The III-V Gallium nitride compound semiconductor has attracted a wide range of bandgaps and high temperature stability for optoelectronic and electronic devices such as light-emitting diodes (LEDs) and laser diodes (LDs). In order to fabricate GaN-based devices and define the mesa layer for formed p and n contacts, inductively coupled plasma reactive ion etching (ICP-RIE) method is generally applied due to GaN quite hard to etch. Precise pattern transfer during fabrication of these devices is required by using ICP-RIE etching method to break strongly Ga-N bonds (8.92eV/atom). However, there are certain of ion-etching damages on the GaN in these processes. Moreover, ion bombardment from ICP-RIE etching process can induce dislocations or formation of dangling bonds on the GaN surface, and it may cause material and/or device damage after ICP etching process. Many reports have found that the studies of the GaN defects induced by the ICP etching process. The optical and electrical properties of semiconductor can be degraded due to ICP-induced defects, and these related process defects are reduced by thermal treatment.

In this work, we mainly study the current transport mechanisms of Ni-Au / n -GaN and the annealing effect of Schottky diodes after ICP etching process under the forward-bias condition. The current transport mechanisms are analyzed in terms of

specific contact resistance (ρ_c), characteristic energy (E_{00}) and ideality factor (η) under different temperatures. We found that the current transport mechanisms are directly dependent on the etching conditions and the annealing process is an effective step in eliminating these defects.

3.2 Schottky diodes with annealing nitride and hydrogen effects

3.2.1 Current voltage characteristics

The reverse current-voltage characteristics of the *n*-GaN Schottky diodes by annealing in N₂ ambient as shown in Fig.3-1. These samples with different surface treatment process conditions are listed in Table 3-1. In Fig.3-1, after ICP etching process, the current-voltage characteristic shows a significant leakage current in the Non-annealed ICP-treated sample (R2). This result may be attributed to the ICP etching process formed damages to deteriorate diodes characteristics due to the ion bombardment [18]-[34]. However, this figure indicated that these damages can be eliminated in the subsequent annealing process at higher temperatures. After annealing at 600°C (A3) and 700°C (A4) for Schottky diodes, the less reverse leakage current for A3 and A4 sample is recovered from Non-annealed ICP-treated sample (R2). Inset of Fig.3-1 indicates the detailed reverse leakage current characteristics of Schottky diodes for R1, A3 and A4 sample. As same discussed above, the reverse breakdown voltage characteristics of Schottky diodes by different surface treatments are shown in Fig.3-2. The reverse breakdown voltage for non-annealed ICP-treated sample (R2) is less than that for the other ones. After ICP etching process, the Schottky diodes have more and more damages to form between metal and semiconductor. The higher reverse leakage current and lower breakdown voltage

result from these damages or ion bombardment from ICP etching process. However, the reverse breakdown voltage characteristics can be recovered by annealing at 600°C (A3) and 700°C (A4) as shown in Fig.3-2. These results were in good agreement with the correlation reverse leakage current. On the other hand, the forward current-voltage characteristics of the *n*-GaN Schottky diodes with annealing in N₂ ambient are also analyzed and shown in Fig.3-3. An obvious current reduction at approximately 0.08 V with samples annealing at 600°C (A3) and 700°C (A4) can be observed. According to Eq.(2-11), the current voltage curves of non-treated sample (R1) are fitted and shown in Fig.3-4. The ideality factor, saturation current and barrier height of Schottky diodes with different annealing treatments can be extracted and analyzed as listed in Table 3-2.

The ideality factor and barrier height for R1 sample is approximately 1.17 and 0.71eV at room temperature and is better than that for the other ones. It is known that the ideality factor (η) is an indicator of ideal surface and is unity for the perfect surface. In our knowledge, samples with a higher ideality factor (η) value have a semiconductor surface far from ideality which means that more defects may be present in the surface. Generally, the barrier height is dependent of the metal work function, semiconductor electron affinity, semiconductor doping density and surface states. The barrier width is subject to the doping density of semiconductor. Therefore, the highly doped semiconductors have narrow barrier width. In this case, the Schottky diodes with different annealing treatments are fabricated and formed by utilized same doping density for epitaxial wafer and contact metal. But the varied barrier width of these samples with different annealing treatments is observed. The damage generally incorporated in the ICP etching process and formed surface states between metal and semiconductor. These surface states can assist electron tunnel from a metal to a

semiconductor and can not pass through barrier height between metal and semiconductor. It means the surface defects generated by ICP etching process to cause higher ideality factor and lower barrier height. There may be some different current transport characteristics in the metal-semiconductor interface of these samples. In this work, the ideality factor for non-annealed ICP-treated sample (R2) is higher than that for the other ones. Lower barrier height for R2 sample will be expected due to ICP etching damage. This indicates that the electrons tunnel and pass through the defects states which generated in the ICP etching process dominate the current transport mechanisms. However, these ICP damages and surface states can be effectively eliminated and reduced by annealing at higher temperature in N₂ ambient. The ideality factor of Schottky diodes with annealing temperatures at higher than 600°C in N₂ ambient for 30 min is nearly unity and similar to non-treated sample (R1). The barrier height of these samples with annealing temperature at higher than 600°C in N₂ ambient for 30 min can recover from non-annealed ICP-treated sample (R2). The ideality factor and barrier height of Schottky diodes by annealing at different temperatures in N₂ ambient are exhibited in Fig.3-5. The solid and hollow shapes represent non-treated sample (R1) and different annealing conditions samples after ICP etching process. The nearly unity ideality factor and higher barrier height are clearly obvious by annealing temperature in N₂ ambient increasing. Therefore, the better Schottky diodes characteristics can be demonstrated by annealing at higher temperature in N₂ ambient.

On the other hand, to study the thermal treatment effects, we utilized H₂ gas during the annealing of the samples after ICP etching process. In our experiment, the samples were annealed in H₂ ambient for 30 min, after ICP etching process. The reverse current-voltage (I-V) and breakdown voltage characteristics of the Schottky

diodes with annealing at different temperatures in H₂ ambient are shown in Fig.3-6 and Fig.3-7, respectively. The reverse leakage current of Schottky diodes is reduced by annealing temperature at higher than 500°C in H₂ ambient. These results are in agreement with the above discussion for N₂ gas. The breakdown voltage at reverse current -100μA of R1, R2, B1, B2, B3 and B4 are around 6.9Volt, 0.8Volt, 0.7Volt, 2.3Volt, 3.0Volt and 3.1Volt, respectively. These detailed results for Schottky diodes with different annealing treatments are listed in Table 3-2. The forward current voltage characteristics of Schottky diodes with annealing at different temperatures in H₂ ambient is shown in Fig.3-8. The better forward current voltage characteristics of Schottky diodes can be observed by annealing temperature at higher than 500°C. According to Eq.(2-11), these current-voltage curves can fit and extract diodes parameter such as ideality factor, saturation current and barrier height, and the plot curve to compare different annealing temperature effects in H₂ ambient as discussed in Table 3-2 and Fig.3-9. By annealing temperature increasing, the ideality factor of Schottky diodes as function of annealing temperature is reduced and the barrier height is enhanced. These results are attributed to less than defects incorporated in the ICP etching process and form defects states between metal and semiconductor due to annealing processes. These surface states can assist electron tunnel from a metal to a semiconductor and can not pass through barrier height between metal and semiconductor to cause higher ideality factor and lower barrier height. Therefore, we found that these defects can be reduced by annealing at higher temperature in N₂ or H₂ ambient. As the defects between metal and semiconductor are decreased, less than surface states can be observed and expected.

3.2.2 Current temperature characteristics

For understand why better current-voltage characteristics of Schottky diodes by annealing at higher temperature and defined current transport mechanisms, theoretical model and current-voltage-temperature characteristics ($I-V-T$) of Schottky diodes can be utilized and discussed. The current transport mechanisms are analyzed in terms of specific contact resistance (ρ_c), characteristic energy (E_{00}), ideality factor (η) and barrier height (Φ_{B0}) for $I-V-T$ characteristics under different measured temperatures. The current-voltage temperature characteristics of R1, R2, A1, A2, A3 and A4 sample are measured at different temperatures and shown in Fig.3-10, Fig.3-11, Fig.3-12, Fig.3-13, Fig.3-14 and Fig.3-15, respectively. As a result, the extracted values for ideality factor indicate a strong temperature, and the ideality factor of R1 sample is strongly deviates from unity as shown in Fig.3-16. As the Schottky diodes with different annealing treatments, the lower barrier height can be observed at low temperature in Fig.3-17. This effect is more obvious at low temperature where the other mechanisms of current transport (generation-recombination, tunneling and leakage) are dominant. According to Eq.(2-3), the specific contact resistance of Schottky diodes with/without different annealing treatments after ICP etching process under different measured temperatures are indicated in Fig.3-18. A strongly temperature-dependent trend of specific contact resistance including that of the non-treated sample (R1) can be observed. In this figure, there is also a weak temperature-dependent trend of specific contact resistance including that of the non-annealed ICP-treated sample (R2). Therefore, the current transport mechanisms of the metal-semiconductor interface can be defined as three regions: the field emission (FE) and the thermionic emission (TE) regions and the mixed region: thermionic/field emission region.

As shown in Fig.3-18, samples by annealing temperature higher than 600°C in N₂ ambient (A3 and A4) as well as the non-treated sample (R1) show a similar trend at different measured temperatures. Thus, the current transport mechanism for these samples was characterized as TE with a strongly temperature-dependent factor by Eq.(2-3). According to the studies of Yu et al. [52], the lower value of the characteristic energy (E_{00}) indicates the current transport mechanism was pure TE and the current transport mechanism was much more temperature sensitive. Also Suzue et al. [70] reported that the thermionic emission current is small at low temperature, thus electrons in the metal do not exhibit sufficient energy to overcome the Schottky barrier and to enter the semiconductor. Electrons may emit the Schottky barrier at low temperature, and the current transport mechanisms are strongly dependent on the temperature. From Eq.(2-19), we can determine the effective Richardson constant A^* by the plot of $\ln I/T^2$ versus $1/T$, and the Richardson constant of Schottky contact with/without surface treatments is shown in Fig.3-19 and detailed extracted values are listed in Table 3-3.

Comparing to the specific contact resistance for TE mechanism as described in Eq.(2-3), a weak relationship of specific contact resistance to temperature can be expected in the FE regime [53]. The specific contact resistance for FE mechanism is characterized by Eq.(2-9). As shown in Fig.3-18, samples with annealing temperature lower than 600°C after ICP etching process (R2, A1 and A2) show weak temperature-dependent trend of specific contact resistance. The current transport mechanism for these samples was characterized as the FE mechanism with weak temperature-dependent trend of specific contact resistance [43], [55]. Thus, the damage incorporated in the ICP etching process on the *n*-GaN surface changes the current transport mechanism in the metal-semiconductor interface from TE to FE.

This indicates the Schottky barrier can be tunneled through the defect states generated in the ICP etching process. These surface states dominate the current transport mechanism of FE at annealing temperatures lower than 600°C. With annealing temperature higher than 600°C in N₂ ambient, the defect states may be reduced to a lower level, and the current transport mechanism changes to TE.

The current transport mechanisms can also be described from the characteristic energy E_{00} by Eq.(2-1). A comparison of characteristic energy (E_{00}) with thermal energy $k_B T$ shows TE is dominant when $k_B T \gg E_{00}$ and FE is dominant when $k_B T \ll E_{00}$. The characteristic energy (E_{00}) and the ideality factor (η) derived from Eq.(2-11) is described as a functions of annealing temperature as listed in Table 3-3. The ideality factor (η) is an indicator of ideal surface and is unity for the perfect surface. Samples with a high ideality factor (η) value have a semiconductor surface far from ideal. It means more defects, and may be present in the surface. With annealing temperature higher than 600°C in N₂ ambient for 30 min, the ideality factor (η) is nearly unity which means the surface defects generated by ICP etching process can be eliminated. The current transport mechanisms were transferred from the TE to FE after ICP etching process, and were backed to TE after high temperature annealing as discussed above. Therefore, we could analyze the current transport mechanisms in terms of the ideality factor (η) and the characteristic energy (E_{00}).

On the other hand, to confirm hydrogen effects of Schottky diodes with different annealing treatments and to define current transport mechanisms, the diodes will be measured at different temperatures. The current voltage temperature characteristics for B1, B2, B3 and B4 sample depend on the temperature and show in Fig.3-20, Fig. 3-21, Fig.3-22 and Fig.3-23, respectively. The ideality factor and barrier height are extracted by Eq.(2-11), and detailed discussions of these samples are shown in

Fig.3-24 and Fig.3-25, respectively. In ideality factor and barrier height, the better current voltage temperature characteristics of Schottky diodes are observed by annealing at higher temperature. The ideality factor and barrier height strongly depend on the measured temperature. According to current voltage temperature characteristics of these samples measured, we can fit and extract the relationship between specific contact resistance and temperature as shown in Fig.3-26. These results indicated agreement with above discussion what a strongly temperature-dependent trend of specific contact resistance including that of the non-treated sample (R1) observed and this current transport mechanism remains thermionic emission (TE). However, there is also a weak temperature-dependent trend of specific contact resistance including that of the non-annealed ICP-treated sample (R2). The field emission (FE) mechanism for R2 sample is dominant. Compared with non-annealed ICP-treated sample (R2), the specific contact resistance for B1 sample is slightly temperature dependent, but not obvious than that for R1 sample. Therefore, we can hypothesize that the current transport mechanism of the B1 sample is dominant between TE and FE, thus thermionic field emission (TFE) dominated. The other samples with annealing temperature higher than 500°C in H₂ ambient (B2, B3 and B4) as well as the non-treated sample (R1) show a similar trend at different measured temperatures. Thus, the current transport mechanism for these samples was characterized as TE with a strongly temperature-dependent factor as shown in Eq.(2-3). To confirm which mechanism for Schottky diodes with different annealing treatments, the characteristic energy (E_{00}) can be utilized and defined. As discussed above same issues, the lower value of the characteristic energy (E_{00}) indicates the current transport mechanism was pure thermionic emission (TE), and it was much more temperature sensitive. In this mechanism, the thermionic emission current is small at low temperature, and

electrons in the metal do not exhibit sufficient energy to overcome the Schottky barrier height and to enter the semiconductor. Electrons may emit the Schottky barrier height at low temperature, and the current transport mechanisms are strongly dependent temperature. From Eq.(2-19), we can also determine the effective Richardson constant A^* by the plot of $\ln I/T^2$ versus $1/T$, and the Richardson contact of Schottky contact with/without annealing H_2 treatments is shown in Fig.3-27. As above-mentioned discussion, the current transport mechanisms can also be confirmed from the characteristic energy E_{00} , and be described by Eq.(2-1). A comparison of characteristic energy (E_{00}) with thermal energy $k_B T$ shows TE is dominant when $k_B T \gg E_{00}$ and FE is dominant when $k_B T \ll E_{00}$. The characteristic energy (E_{00}) and the ideality factor (η) of Schottky diodes with hydrogen annealing effects derived from Eq. (2-11) and was described as a function of annealing temperature as listed in Table 3-3. The temperature dependent for field emission (FE) in specific contact resistance is weaker than that for thermionic emission (TE). A weak relationship of specific contact resistance to temperature can be expected in the FE mechanism. The specific contact resistance of sample with annealing temperature at 400°C in H_2 ambient (B1 sample) for FE mechanism is characterized by Eq.(2-9) and shows in Fig.3-26. We have found that a weak temperature-dependent trend of specific contact resistance in this sample. This result may attribute to the damages where ICP etching process formed on the n -GaN surface cause electron in the metal to emit or tunnel to semiconductor. This phenomenon would result in higher ideality factor and lower barrier height as discussed above section. However, these defects by ICP etching process can be eliminated by annealing temperature more than 500°C in H_2 ambient. The strongly temperature dependent trend for B2, B3 and B4 sample in specific contact resistance is obvious in Fig.3-26. Lower defects states density for these

samples will be anticipated and thermionic emission (TE) mechanism is dominant by annealing temperature higher than 500°C in H₂ ambient

3.2.3 Capacitance frequency characteristics

As discussed above section, we have described qualitative analysis of Schottky diodes with ICP treatment and utilized different annealing treatments to improve the diodes characteristics, to reduce the leakage current and to confirm the current transport mechanisms. However, we can not understand that how many defects states in these samples to affect the diodes characteristics. In this section, we apply the capacitance-frequency method to characterize and define defects quantities for Schottky diodes with/without different annealing treatments. The variation in measured capacitance may be due to interfacial defects or deep level defects [71].

Fig.3-28 shows the interfacial states capacitance characteristics of Schottky diode for non-treated sample (R1) and non-annealed ICP-treated sample (R2). The frequency dispersion in the interfacial states can be observed clearly. According to Eq.(2-26), there is one plateau region in the C_p -frequency relation with certain relaxation time. Yet, in Fig.3-28, the data manifests two plateau regions in the frequency range non-treated sample (R1) around 100Hz to 2KHz and 100KHz to 300KHz, respectively. There may be different types of state in the semiconductor. This interfacial states capacitance can be considered to be the overall effects of different kinds of interfacial centers [66]-[68]. We can do the best fitting procedure in different frequency ranges [63]. For each interfacial center, the interfacial states capacitance can be achieved from Eq.(2-27). In Fig.3-28, the dot line curve represents the best fitting procedure of the experimental data. In the frequency range 100Hz to 2KHz, the attracted m -type interface state density N_{ss-m} for non-treated sample (R1) is

$5.0 \times 10^{10} \text{ eV}^{-1} \text{ cm}^{-2}$. In the frequency range from 100KHz to 1MHz, the associated f -type interface state density N_{ss-f} for non-treated sample (R1) is $1.0 \times 10^{11} \text{ eV}^{-1} \text{ cm}^{-2}$. The relaxation time of m -type and f -type for non-treated sample (R1) is $1.9 \times 10^{-5} \text{ sec}$ and $2.7 \times 10^{-7} \text{ sec}$, respectively as listed in Table 3-4.

For samples after ICP etching process (R2), the results of the C_p versus frequency were shown in Fig.3-28. Comparing to non-treated sample (R1), there are three plateau regions in Fig.3-28. There may be some different types of interfacial centers of the GaN after ICP etching process. Since there are three plateau regions in Fig.3-28, we hypothesize that there were three types of interfacial states N_{ss-s} , N_{ss-m} and N_{ss-f} with interfacial states capacitances C_{p-s} , C_{p-m} and C_{p-f} , respectively in the frequency range from 100Hz to 1KHz, 1KHz to 100KHz and 100KHz to 1MHz, respectively. We fit the C_p -frequency for each range by Eq.(2-27) with $i=s, m, f$. The curves in this figure are the fitting results for each interfacial states capacitance. The fitting results are listed in Table 3-4. A small amount of interfacial state (N_{ss-f}) is arisen in the non-treated sample (R1), and can be also observed. There are different types of interfacial states arisen for the GaN samples after ICP etching process. In this case, the s -type of interfacial states (N_{ss-s}) becomes dominated, and the interfacial states density is around $4.3 \times 10^{12} \text{ eV}^{-1} \text{ cm}^{-2}$ for non-annealed ICP-treated sample (R2). By the way, the m - and f -type of interfacial states is around $8.2 \times 10^{11} \text{ eV}^{-1} \text{ cm}^{-2}$ and $2.4 \times 10^{11} \text{ eV}^{-1} \text{ cm}^{-2}$. It is known that the annealing process can reduce the defects densities [69]. The result of the C_p -frequency as ICP etching sample which are annealing at 400°C in N_2 ambient in 30 min (A1 sample) as shown in Fig.3-29. In this figure, we can also distinguish three types of interfacial states which are s -, m - and f -type. These interfacial states density can be defined and are $3.4 \times 10^{12} \text{ eV}^{-1} \text{ cm}^{-2}$, $2.6 \times 10^{11} \text{ eV}^{-1} \text{ cm}^{-2}$ and $1.3 \times 10^{11} \text{ eV}^{-1} \text{ cm}^{-2}$, respectively. The s -type interfacial states density for A1

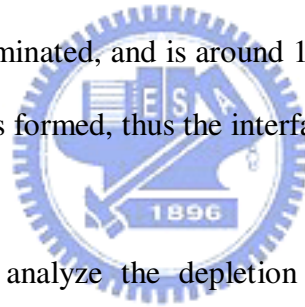
sample is higher than the other ones, this is, *s*-type defect is dominant in this case. Figure 3-30 shows the results of the C_p -frequency with annealing temperature at 500°C (A2 sample). Compared with R1 and A1 sample, we found that the interfacial capacitance reduces and the plateau region is not so clear at low frequency for A2 sample. The interfacial states density of *s*-, *m*- and *f*-type are $1.9 \times 10^{11} \text{ eV}^{-1} \text{ cm}^{-2}$, $1.1 \times 10^{11} \text{ eV}^{-1} \text{ cm}^{-2}$ and $6.0 \times 10^{10} \text{ eV}^{-1} \text{ cm}^{-2}$ for A2 sample, respectively. The *s*-type defect is dominant for Schottky diode with annealing temperature 500°C in N₂ ambient (A2 sample). However, we saw that *s*-type interfacial state for A2 sample is less than one order of magnitude that for A1 sample. This result indicates that improvement of Schottky diodes with ICP etching damage by annealing at 500°C in N₂ ambient is better than that by annealing at 400°C. With 600°C annealing process in N₂ ambient as shown in Fig.3-31, the *f*-type interfacial state reduce to $1.3 \times 10^{11} \text{ eV}^{-1} \text{ cm}^{-2}$, and is quite near the value of the non-treated sample ($1.0 \times 10^{11} \text{ eV}^{-1} \text{ cm}^{-2}$, R1). The quantities of *s*- and *m*-type interfacial states around $3.0 \times 10^{10} \text{ eV}^{-1} \text{ cm}^{-2}$ and 5.8×10^{10} are both less than that of the *f*-type around $1.3 \times 10^{11} \text{ eV}^{-1} \text{ cm}^{-2}$. Thus, the N₂ annealing process at 600°C is effective to remove both of the *s*-type and the *m*-type of interfacial states. Yet, a small amount of interfacial defects in the *f*-type is increased, and it can be observed as the annealing temperature is increased from 500°C to 600°C. Thus, the *f*-type interfacial state becomes dominated for the ICP-treated samples after annealing in N₂ ambient in 600°C (A3). In conclusion, the interfacial states density versus annealing temperature is shown in Fig.3-32. The interfacial state for *s*-type is generated after the ICP-etched process, and is decreased as the annealing temperature is increased. There is a great decrease as the annealing temperature reaches from 400°C to 600°C in N₂ ambient. The interfacial state for *m*-type also is decreased as the annealing temperature is increased from 400°C to 600°C. The *f*-type interfacial state

with non-treated sample (R1) is all around $1.0 \times 10^{11} \text{ eV}^{-1} \text{ cm}^{-2}$ in this figure. A small amount of N_{ss-f} is decreased as the temperature is increased from 400°C to 500°C , but it is increased as the temperature is increased from 500°C to 600°C . This embedded f -type interfacial state can not be reduced effectively via the annealing process in N_2 ambient. The improvement of Schottky diodes characteristics for reducing the defects can be demonstrated by annealing temperature more than 600°C in N_2 ambient.

Figure 3-33 shows the C_p -frequency results for ICP etching samples followed by 400°C annealing process in H_2 ambient. Comparing 400°C annealing process in N_2 ambient (A1 sample), the lower interfacial state capacitance for B1 sample with annealing process in H_2 ambient at low frequency can observe as shown in Fig.3-34. Thus, the lower s -type interfacial state for B1 sample can be anticipated and the detailed extraction value for interfacial states density and relaxation time is listed in Table 3-4. In fact, the quantities of s - and m -type interfacial defect around $2.8 \times 10^{11} \text{ eV}^{-1} \text{ cm}^{-2}$ and $2.5 \times 10^{11} \text{ eV}^{-1} \text{ cm}^{-2}$ are both below those of f -type interfacial states. The f -type interfacial defect is dominated and is around $4.8 \times 10^{11} \text{ eV}^{-1} \text{ cm}^{-2}$. The s -type defect density ($3.4 \times 10^{12} \text{ eV}^{-1} \text{ cm}^{-2}$) for Schottky diodes by annealing in H_2 ambient at 400°C is less than one order of magnitude that for by in N_2 ambient ($2.8 \times 10^{11} \text{ eV}^{-1} \text{ cm}^{-2}$). Annealing under H_2 ambient is more effective for reducing the defects than that under N_2 ambient. Therefore, the improvement of Schottky diodes characteristics by annealing in H_2 ambient is more effective than that by annealing in N_2 ambient. In H_2 ambient, the ICP induced damage may be reduced to a lower level by H_2 diffusing and chemically reacting with the defects [72]-[74].

The interfacial states and capacitance decrease as the annealing temperature is increased to 500°C in H_2 ambient (B2 sample) as shown in Fig.3-35. The interfacial states density of s -, m - and f -type are $5.0 \times 10^{10} \text{ eV}^{-1} \text{ cm}^{-2}$, $4.2 \times 10^{10} \text{ eV}^{-1} \text{ cm}^{-2}$ and

$1.3 \times 10^{11} \text{ eV}^{-1} \text{ cm}^{-2}$ for B2 sample, respectively. Yet, as the temperature reaches 600°C in H_2 ambient, a dramatic increase of the *s*-type interfacial capacitance and states density can be observed as shown in Fig.3-36 and Table 3-4. A small amount of the interfacial states of *m*- and *f*-type is increased to $6.8 \times 10^{10} \text{ eV}^{-1} \text{ cm}^{-2}$ and $1.6 \times 10^{11} \text{ eV}^{-1} \text{ cm}^{-2}$. In H_2 ambient, the interfacial states density for Schottky diodes with different annealing treatments are shown in Fig.3-37. Besides *s*-type defect, the interfacial state density for the other type defects decrease with annealing temperature increasing in H_2 ambient. However, the *s*-type defect reduce by annealing temperature increasing to 500°C , and increase by annealing temperature at 600°C . This result is attributed to the H_2 may diffuse and react chemically [72]-[74], some hydrogen related defects may be formed, thus they increase the interfacial states. The *s*-type interfacial defect becomes dominated, and is around $1.1 \times 10^{12} \text{ eV}^{-1} \text{ cm}^{-2}$. There may be some hydrogen-related defects formed, thus the interfacial state density is increased in this case.



On the other hand, to analyze the depletion width and barrier height, the capacitance voltage method is employed. The capacitance voltage characteristics of Schottky diodes with or without ICP treatment is measured at a frequency 1MHz and shows in Fig.3-38. The dot line indicate the fitting curve by Eq.(2-24). According to above discussed in Section 2.1.4, the barrier height for samples with different annealing treatments is extracted and listed in Table 3-5. The detailed capacitance voltage curve for N_2 and H_2 treated sample is shown in Fig.3-39 and Fig.3-40, respectively. The depletion width of Schottky diodes with different treatments are also analyzed and listed in Table 3-5. The barrier height depends on the depletion width as annealing at different temperatures in N_2 or H_2 ambient.

Compared with barrier height measured by *I-V* method, *I-V-T* method and *C-V*

method by reported several groups [75]-[79], the $\phi_B(I-V)$ and $\phi_B(I-T-V)$ are lower than $\phi_B(C-V)$ due to thermionic emission and near-flatband conditions. The $\phi_B(C-V)$ yields the flat band by extracted from C-V method, but the $\phi_B(I-V)$ and $\phi_B(I-T-V)$ is analyzed at zero bias by I-V method. The $\phi_B(I-V)$ and $\phi_B(I-T-V)$ are considered as the current transport mechanism due to thermionic or field emission and without image force lowering effect [29]. The $\phi_B(C-V)$ is extrapolated from the plot of $1/C^2$ versus applied bias voltage and corresponds to near-flatband conditions, this is the barrier lowering is close to zero. On the other hand, $\phi_B(C-V)$ can not affect with the barrier shape between metal and semiconductor due to defined from the edge of depletion layer. In contract, $\phi_B(I-V)$ and $\phi_B(I-T-V)$ is sensitive to the barrier shape. Higher barrier height and depletion width accompany with annealing temperature increasing. These results are attributed to reduce the surface defects by annealing in higher temperature. Greater depletion width means that electrons can't easily emit or tunnel into semiconductor by surface states, thus the higher barrier is observed. The depletion width of Schottky diodes with different surface treatments by applying reverse bias is shown in Fig.3-41.

3.2.4 Summary

The current transport mechanisms of Ni-Au on *n*-GaN and the thermal stability of Schottky diodes by surface treatments were investigated and fabricated. The current transport mechanisms of non-treated *n*-type GaN (R1 sample) was TE based on the finding that the ideality factor was approximately unity and the characteristic energy was approximately zero. The current transport mechanism was FE based on the finding that the ideality factor and characteristic energy were high due to the ICP

etching processes. This indicated the presence of the barrier through which carrier tunneling could take place. Thus, the surface state between GaN and metal could occur by ICP etching and cause carrier tunneling from metal to GaN. However, the current transport mechanisms changed from FE to TE by annealing at 600°C in N₂ ambient or 500°C in H₂ ambient for 30 min, that is, the current transport mechanism dominates TE or between TE and FE. These results showed that the ICP damages were reduced to a low level and the Schottky diodes characteristics recovered by annealing 600°C in N₂ ambient or 500°C in H₂ ambient for 30 min in low ideality factor as shown in Fig.3-42, in high barrier height as shown in Fig.3-43 and in interfacial states density for N_{SS-s}, N_{SS-m} and N_{SS-f} as shown in Fig.3-44, Fig.3-45 and Fig.3-46, respectively. Figure 3-42 indicates that the ideality factor of Schottky diodes with ICP etching damage (R2 sample) is higher than that of the others and it decrease with annealing temperature increasing in N₂ or H₂ ambient. The Schottky barrier height can be also enhanced by annealing temperature increasing and shows in Fig. 3-43. We have demonstrated Schottky diodes characteristics improved by annealing treatment, whether in N₂ or H₂ ambient. The *s*-type interfacial defects can be reduced by annealing temperature increasing to 600°C in N₂ ambient or 500°C in H₂ ambient. The *m*-type interfacial defects can be recovered to non-treated *n*-type GaN (R1 sample) by annealing at high temperature in N₂ ambient or in H₂ ambient. In *f*-type interfacial defects, annealing in N₂ ambient is more effective than that in H₂ ambient. However, the interfacial defects of the Schottky diode with ICP induced defect (R2 sample) by ICP etching process is dominant *s*-type, and non-treated sample (R1 sample) is dominant *f*-type as listed in Table3-6. The worse characteristics of Schottky diodes with ICP induced defect is observed due to *s*-type interfacial defects dominated. Therefore, to reduce *s*-type interfacial defects is anticipated. In this work, we found

that the *s*-type interfacial defects can be reduced about one to two order of magnitude by annealing at 500°C in H₂ ambient. The interfacial defects is *f*-type indicating the ICP induced defects nearly recovered to non-treated sample (R1), this is the defects result from epitaxial growth such as dislocation or the others. Besides, the *s*-type defect increases by annealing temperature at 600°C in H₂ ambient. This result may be attributed to the H₂ may diffuse and react chemically [72]-[74], some hydrogen related defects may be formed, thus they increase the interfacial states [80]-[85]. There may be some hydrogen-related defects formed, thus the interfacial state density is increased in this case. Annealing in H₂ ambient is much more effective for removing ICP induced defects rather than that in N₂ ambient.



Table 3-1 Different surface treatment process conditions

No.	Annealing temperature (°C)	Ambient	ICP treatment
R1	No	No	Without
R2	No	No	With
A1	400	N ₂	With
A2	500	N ₂	With
A3	600	N ₂	With
A4	700	N ₂	With
B1	400	H ₂	With
B2	500	H ₂	With
B3	600	H ₂	With
B4	700	H ₂	With

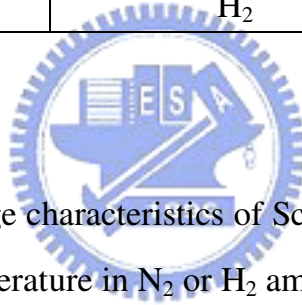


Table 3-2 Current voltage characteristics of Schottky diodes by annealing at different temperature in N₂ or H₂ ambient

No.	Ideality factor, η	Saturation current, I_s	$V_{BI-100\mu m}$ (Volt)	Barrier height, Φ_{B0} (eV)
				I-V
R1	1.17	1.0×10^{-9}	6.9	0.71
R2	3.04	6.1×10^{-5}	0.8	0.17
A1	1.81	4.5×10^{-6}	0.9	0.24
A2	1.98	8.6×10^{-6}	0.9	0.17
A3	1.25	1.5×10^{-7}	4.4	0.48
A4	1.27	4.7×10^{-8}	5.0	0.55
B1	2.15	8.1×10^{-6}	0.7	0.25
B2	1.35	8.3×10^{-8}	2.3	0.4
B3	1.3	1.4×10^{-7}	3.0	0.45
B4	1.41	2.9×10^{-7}	3.1	0.43

Table 3-3 Current temperature characteristics of Schottky diodes by annealing at different temperature in N₂ or H₂ ambient

No.	A* (A · k ⁻² · cm ⁻²)	E ₀₀ (eV)	Barrier height, Φ_{B0} (eV)
			I-V-T
R1	17.30	0.01	0.72
R2	9 × 10 ⁻⁴	1.29	0.18
A1	8 × 10 ⁻⁴	1.37	0.24
A2	1 × 10 ⁻⁴	4.25	0.18
A3	0.26	0.07	0.48
A4	1.35	0.04	0.55
B1	2.4 × 10 ⁻³	1.29	0.27
B2	8.8 × 10 ⁻³	0.34	0.40
B3	0.10	0.10	0.43
B4	0.08	0.11	0.43

Table 3-4 Summary of the interfacial states characteristics for Schottky contact with/without by annealing in N₂ or H₂ ambient.

No.	N _{ss-s} (eV ⁻¹ cm ⁻²)	τ (sec)	N _{ss-m} (eV ⁻¹ cm ⁻²)	τ (sec)	N _{ss-f} (eV ⁻¹ cm ⁻²)	τ (sec)
R1	-	-	5.0 × 10 ¹⁰	1.9 × 10 ⁻⁵	1.0 × 10 ¹¹	2.7 × 10 ⁻⁷
R2	4.3 × 10 ¹²	1.0 × 10 ⁻³	8.2 × 10 ¹¹	4.0 × 10 ⁻⁵	2.4 × 10 ¹¹	3.2 × 10 ⁻⁷
A1	3.4 × 10 ¹²	2.6 × 10 ⁻³	2.6 × 10 ¹¹	6.5 × 10 ⁻⁵	1.3 × 10 ¹¹	2.7 × 10 ⁻⁷
A2	1.9 × 10 ¹¹	2.0 × 10 ⁻³	1.1 × 10 ¹¹	3.5 × 10 ⁻⁵	6.0 × 10 ¹⁰	2.7 × 10 ⁻⁷
A3	3.0 × 10 ¹⁰	1.5 × 10 ⁻⁴	5.8 × 10 ¹⁰	2.4 × 10 ⁻⁵	1.3 × 10 ¹¹	2.3 × 10 ⁻⁷
B1	2.8 × 10 ¹¹	1.0 × 10 ⁻³	2.5 × 10 ¹¹	7.1 × 10 ⁻⁵	4.8 × 10 ¹¹	2.7 × 10 ⁻⁷
B2	5.0 × 10 ¹⁰	6.0 × 10 ⁻⁴	4.2 × 10 ¹⁰	4.0 × 10 ⁻⁵	1.3 × 10 ¹¹	2.7 × 10 ⁻⁷
B3	1.1 × 10 ¹²	5.8 × 10 ⁻⁴	6.8 × 10 ¹⁰	1.0 × 10 ⁻⁵	1.6 × 10 ¹¹	2.7 × 10 ⁻⁷

Table 3-5 Barrier height for sample with different annealing treatments is extracted by different methods.

No.	Barrier height, Φ_{B0} (eV)	Barrier height, Φ_{B0} (eV)	Barrier height, Φ_{B0} (eV)	W (Å)
	I-V	I-V-T	C-V	C-V
R1	0.71	0.72	1.05	508
R2	0.17	0.18	0.97	203
A1	0.24	0.24	1.32	260
A2	0.17	0.18	1.55	203
A3	0.48	0.48	1.15	396
A4	0.55	0.55	1.28	423
B1	0.25	0.27	1.16	275
B2	0.4	0.4	1.02	368
B3	0.45	0.43	1.10	394
B4	0.43	0.43	1.10	382

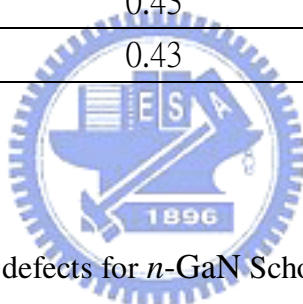


Table 3-6 Dominant type of defects for *n*-GaN Schottky diodes by different surface treatment

No.	Dominant type of defects
R1	<i>f</i> -type
R2	<i>s</i> -type
A1	<i>s</i> -type
A2	<i>s</i> -type
A3	<i>f</i> -type
B1	<i>f</i> -type
B2	<i>f</i> -type
B3	<i>s</i> -type

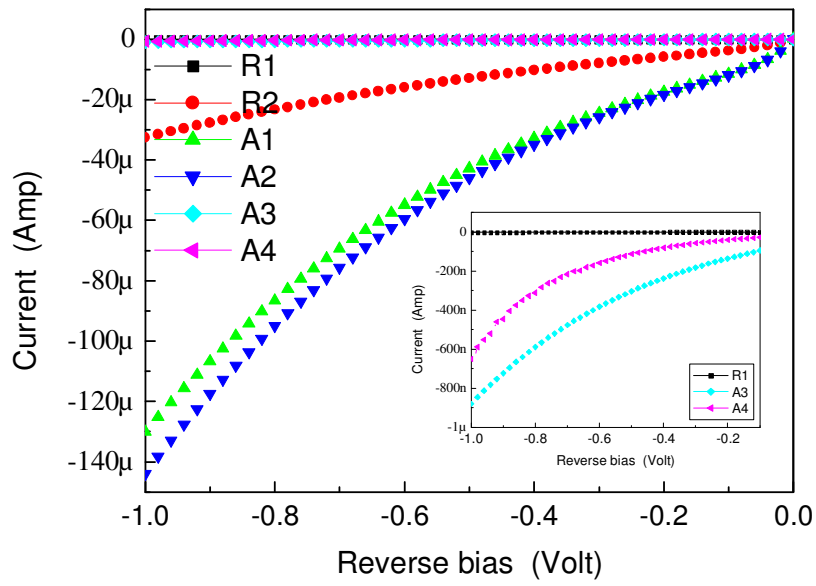


Fig. 3-1 Reverse current voltage characteristics of *n*-GaN Schottky diodes by annealing at different temperatures in N₂ ambient for 30 min

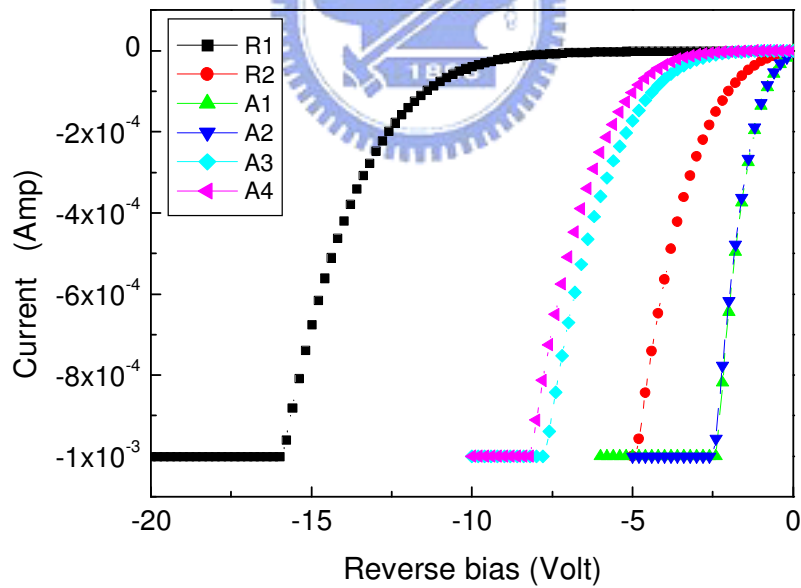


Fig. 3-2 Reverse breakdown voltage characteristics of Schottky diodes by different surface treatments

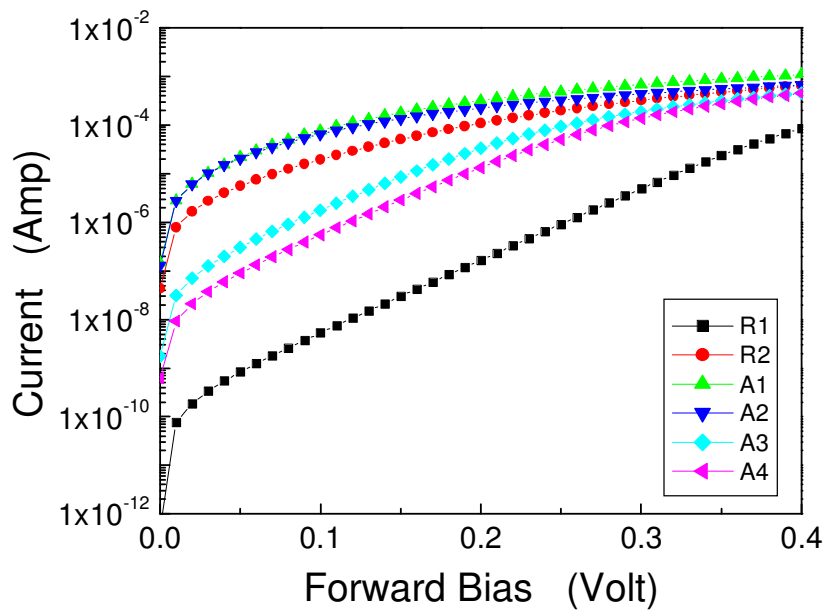


Fig. 3-3 Forward current voltage characteristics of *n*-GaN Schottky diodes by annealing at different temperatures in N₂ ambient for 30 min

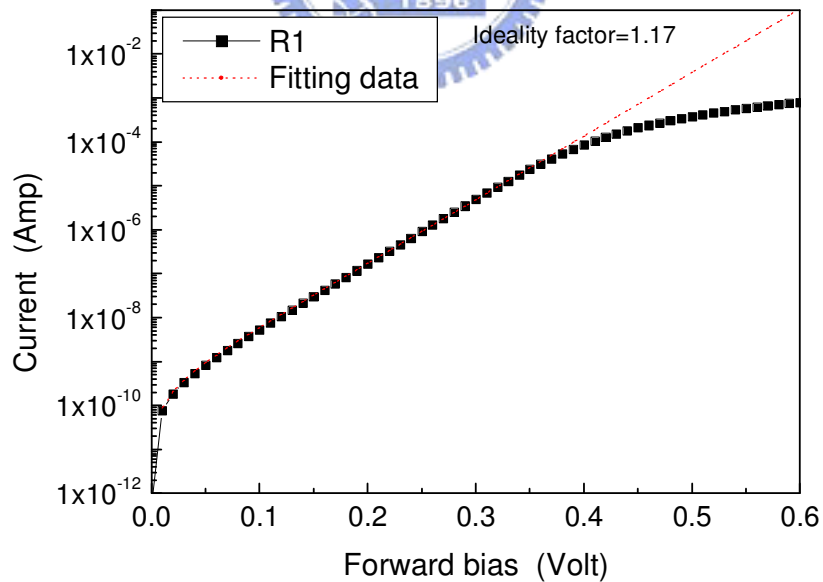


Fig. 3-4 Current voltage characteristics of *n*-GaN Schottky diodes without ICP etching treatment are fitting and analyzed by Eq. (2-11).

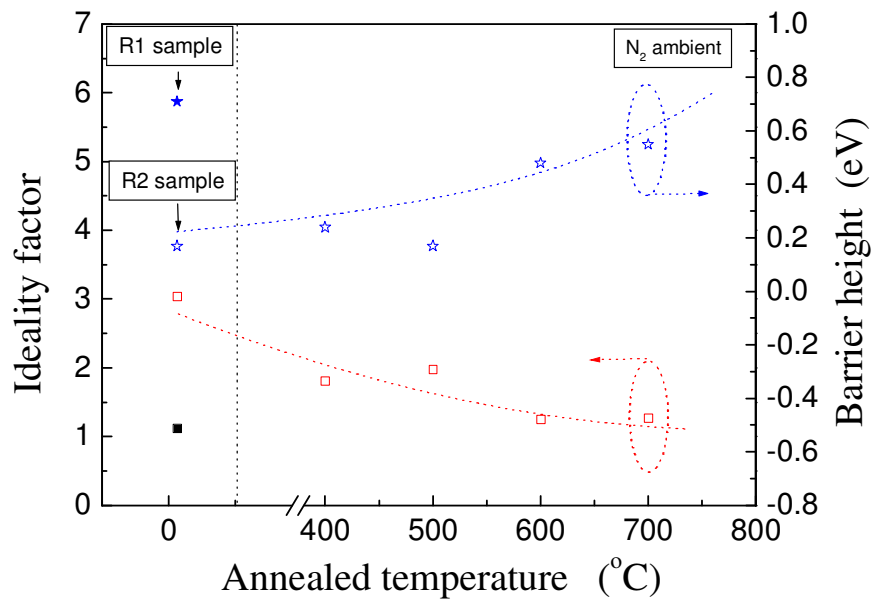


Fig. 3-5 Ideality factor and barrier height of Schottky diodes are analyzed by annealing at different temperatures in N_2 ambient. The solid shape donates Schottky diodes without ICP treatment (R1 sample), in contrast the void shape donates Schottky diodes with ICP treatment (R2 sample) by annealing at different temperatures.

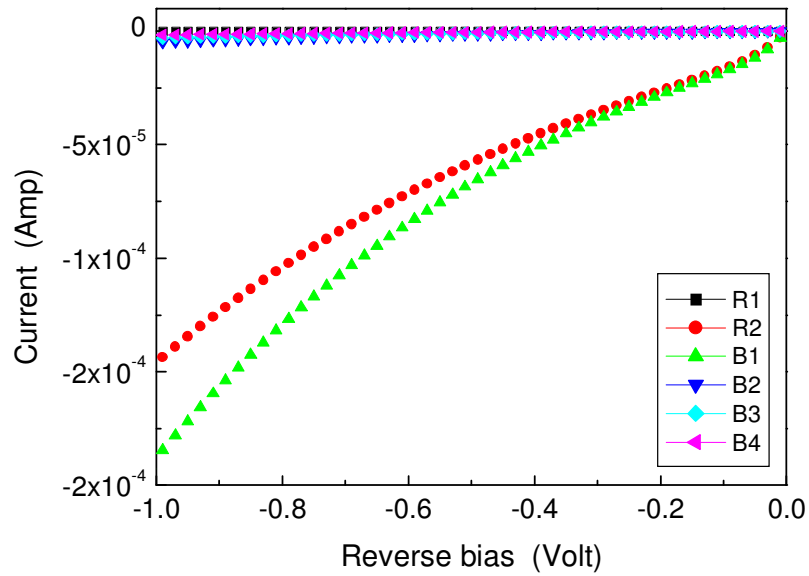


Fig. 3-6 Reverse current-voltage (I-V) characteristics of the Schottky diodes by annealing at different temperatures in H₂ ambient

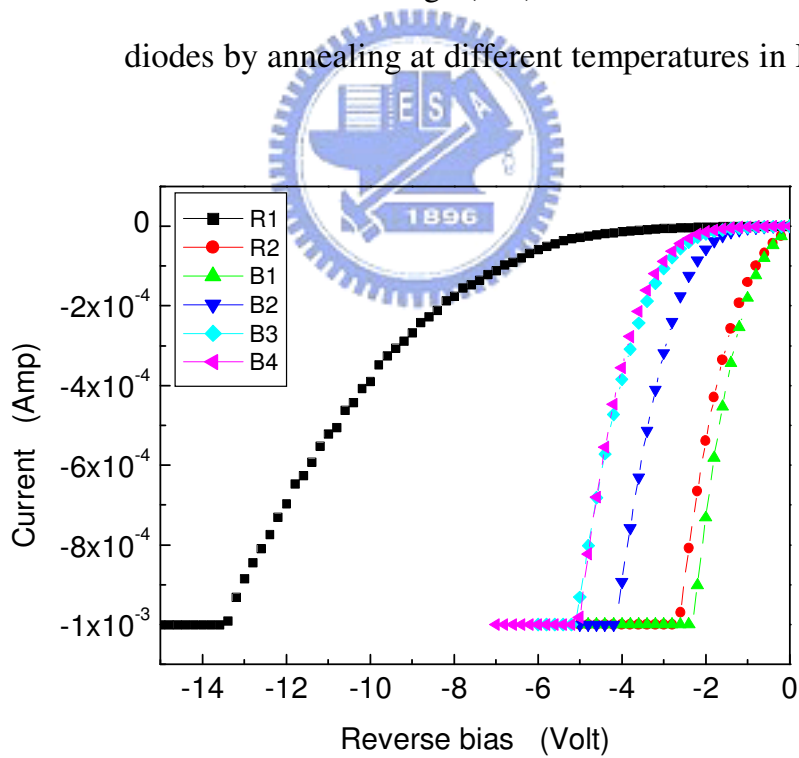


Fig. 3-7 Reverse breakdown voltage characteristics of the Schottky diodes by annealing at different temperatures in H₂ ambient

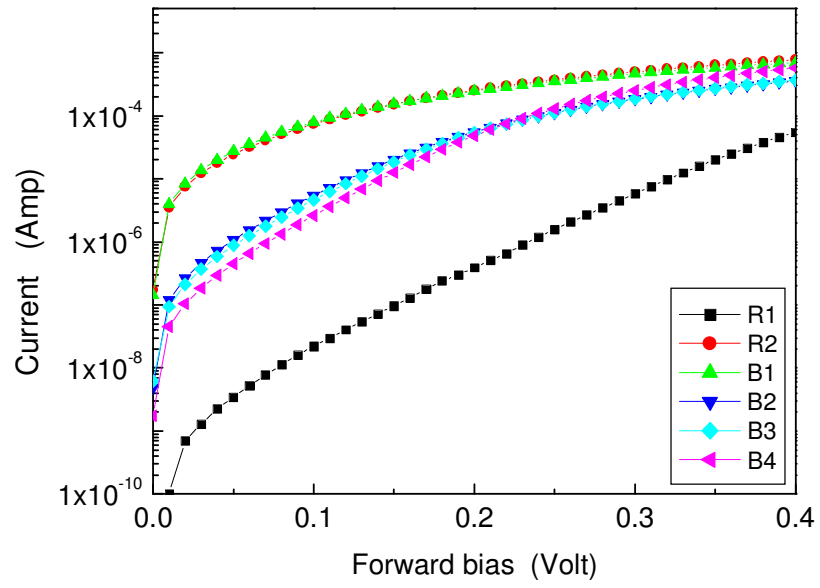
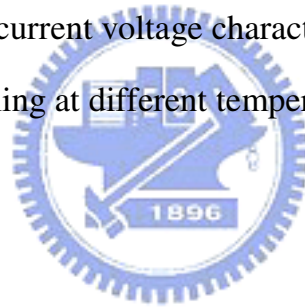


Fig. 3-8

Forward current voltage characteristics of Schottky diodes by annealing at different temperatures



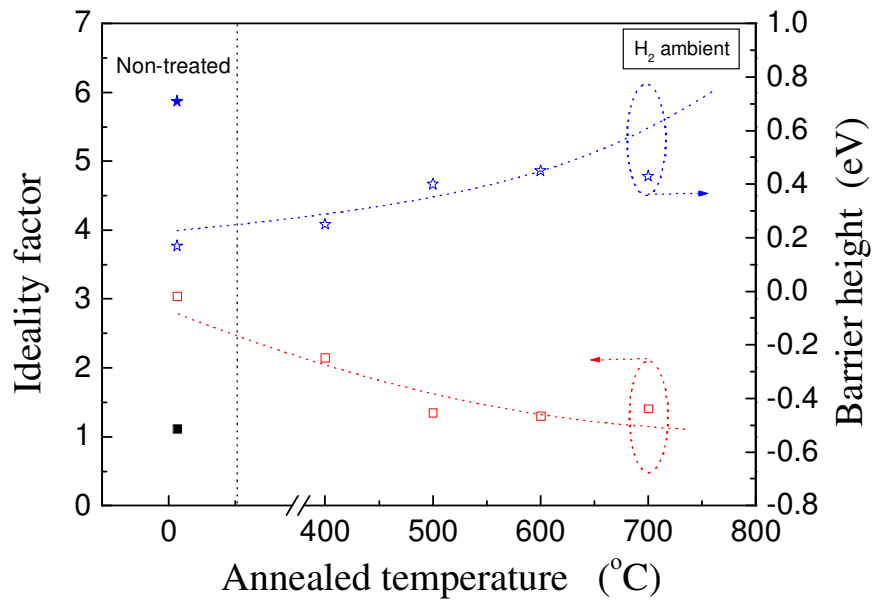


Fig. 3-9

Ideality factor and barrier height of Schottky diodes are analyzed by annealing at different temperatures in H_2 ambient. The solid shape donates Schottky diodes without ICP treatment (R1 sample), in contrast the void shape donates Schottky diodes with ICP treatment (R2 sample) by annealing at different temperatures.

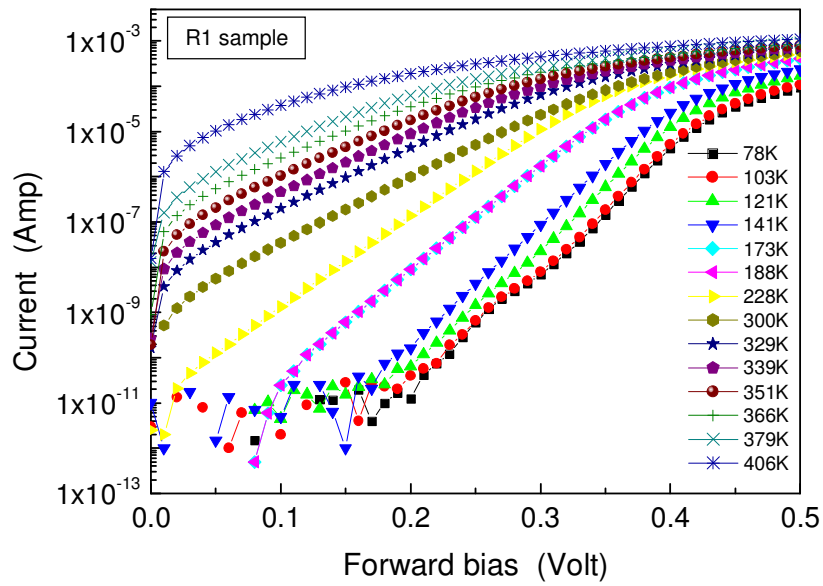


Fig. 3-10 Current-voltage temperature characteristics of Schottky diodes without ICP treatment (R1 sample) by measuring at different temperatures

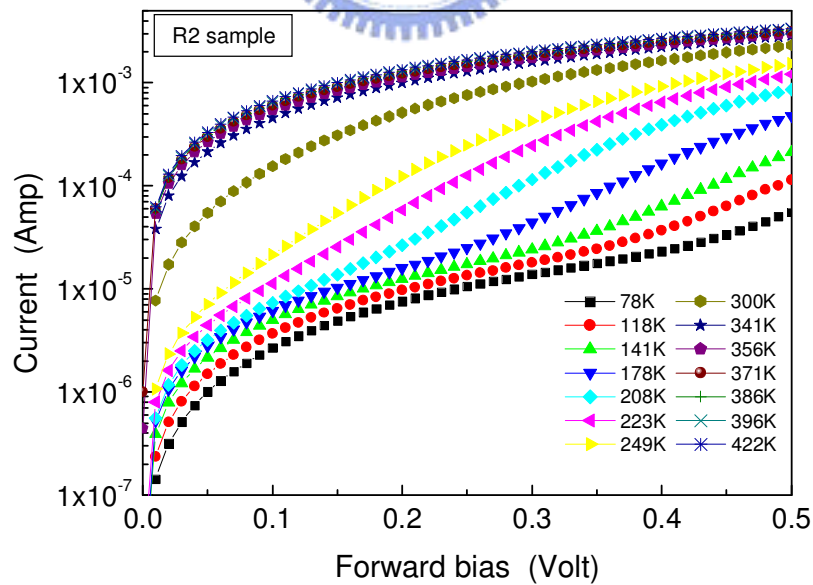


Fig. 3-11 Current-voltage temperature characteristics of Schottky diodes with ICP treatment (R2 sample)

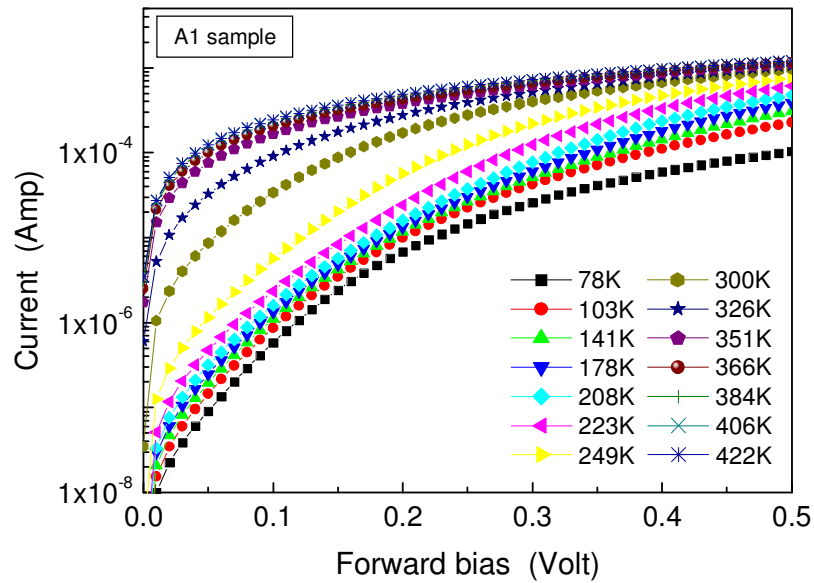


Fig. 3-12 Current-voltage temperature characteristics of Schottky diodes with annealing at 400°C in N₂ ambient (A1 sample)

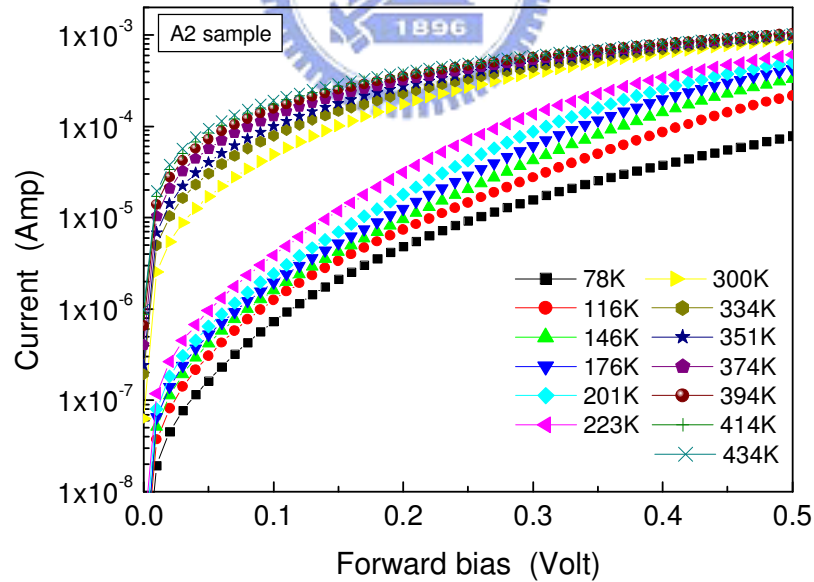


Fig. 3-13 Current-voltage temperature characteristics of Schottky diodes with annealing at 500°C in N₂ ambient (A2 sample)

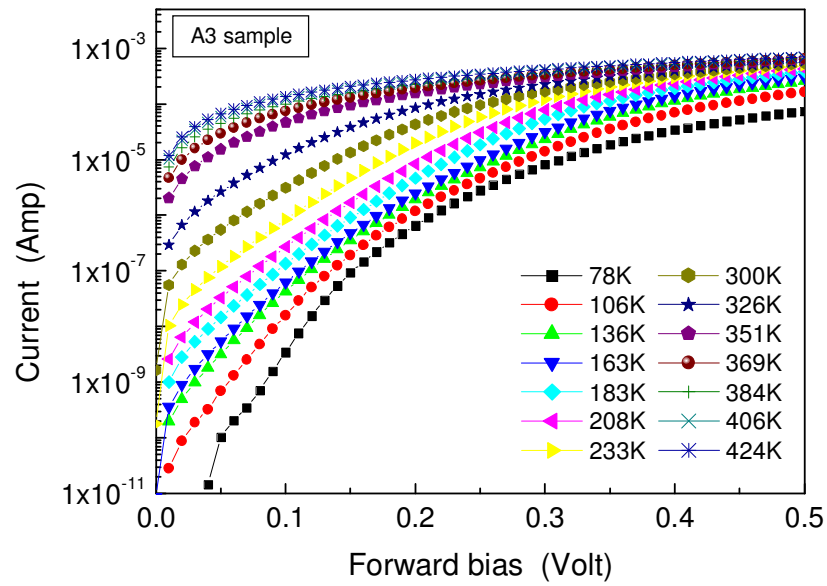


Fig. 3-14 Current-voltage temperature characteristics of Schottky diodes with annealing at 600°C in N₂ ambient (A3 sample)

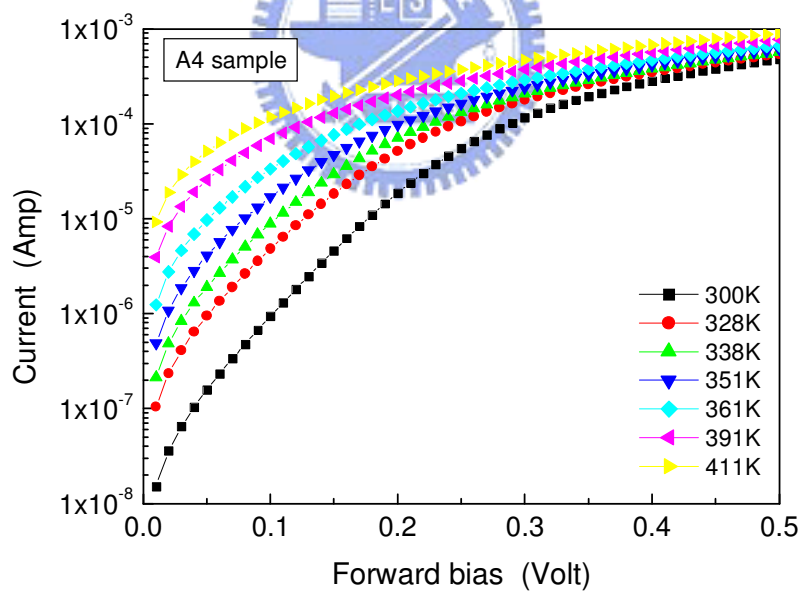


Fig. 3-15 Current-voltage temperature characteristics of Schottky diodes with annealing at 700°C in N₂ ambient (A4 sample)

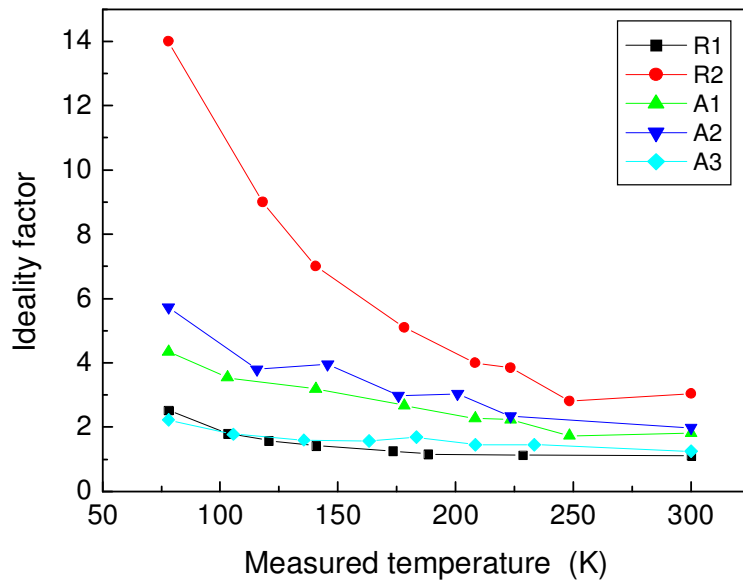


Fig. 3-16 Ideality factor is extracted by measuring at different temperatures for Schottky diodes with annealing in N_2 ambient.

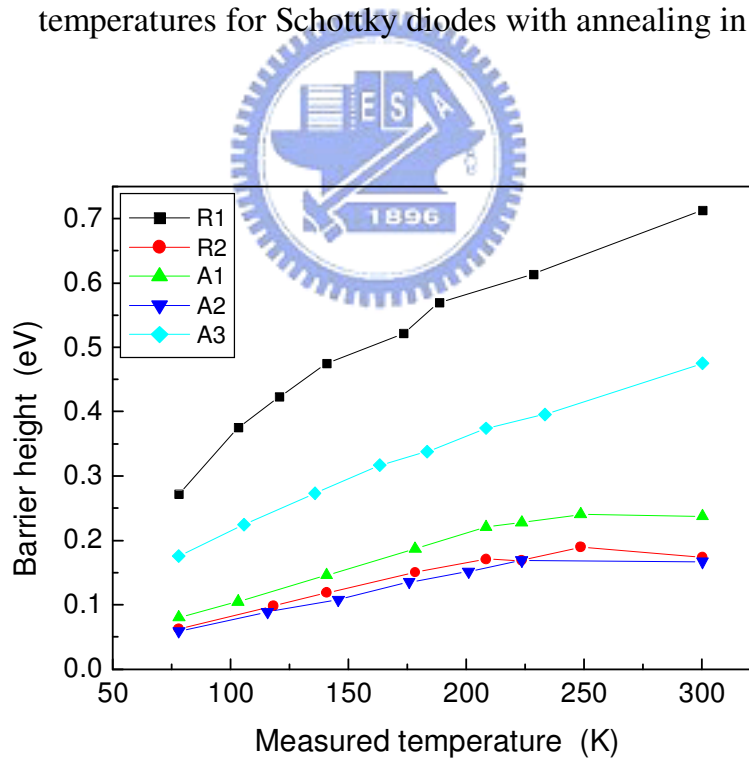


Fig. 3-17 Barrier height is extracted by measuring at different temperatures for Schottky diodes with annealing in N_2 ambient.

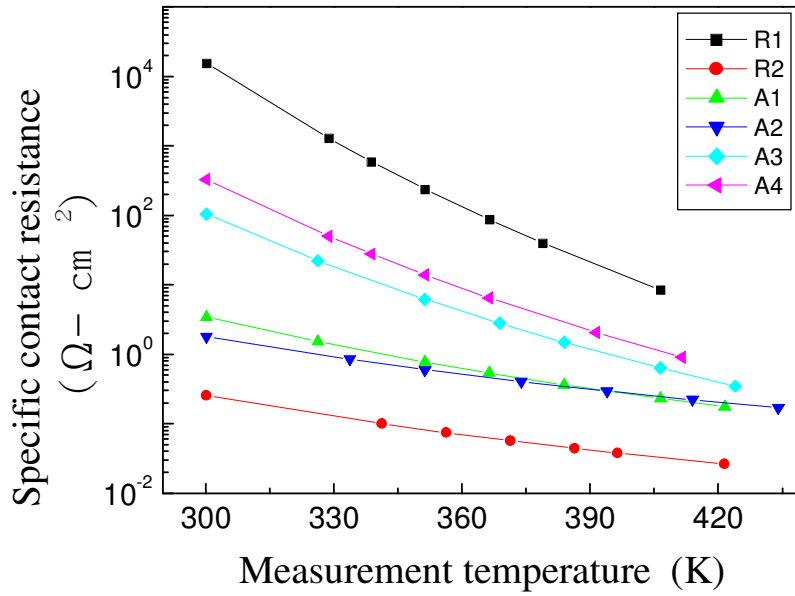


Fig. 3-18 Specific contact resistance of Schottky diodes with different surface treatment in N_2 ambient is indicated as a function of temperature.

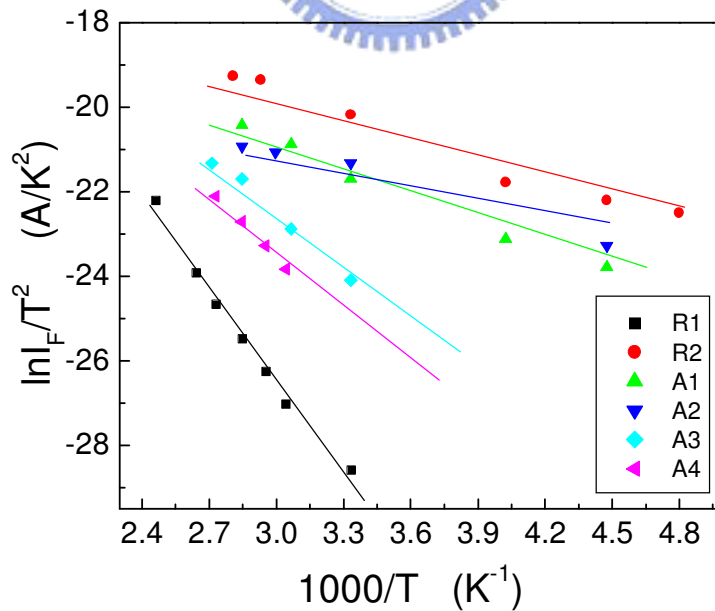


Fig. 3-19 Richardson plot of the Schottky diodes with different surface treatments in N_2 ambient.

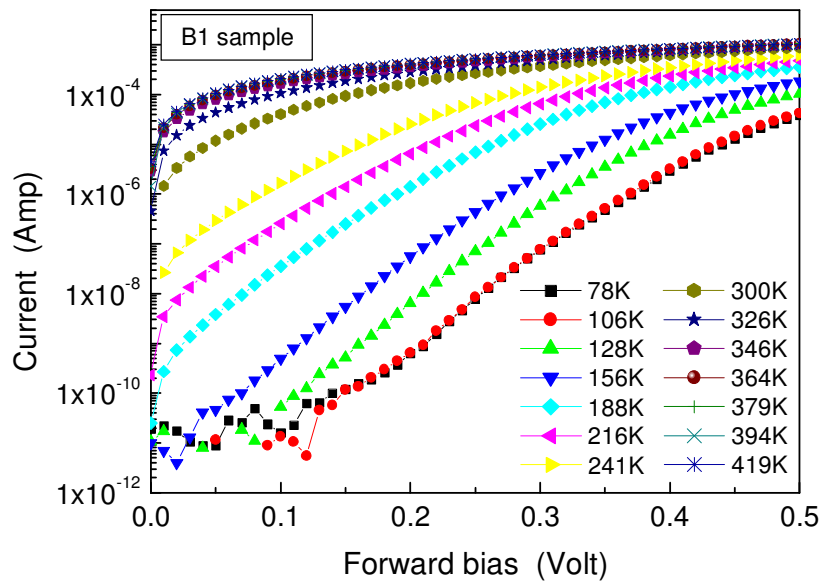
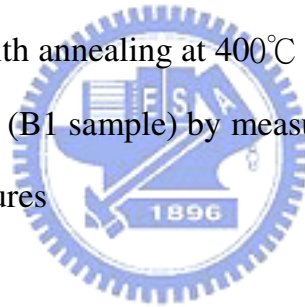


Fig. 3-20

Current-voltage temperature characteristics of Schottky diodes with annealing at 400°C in H_2 ambient after ICP treatment (B1 sample) by measuring at different temperatures



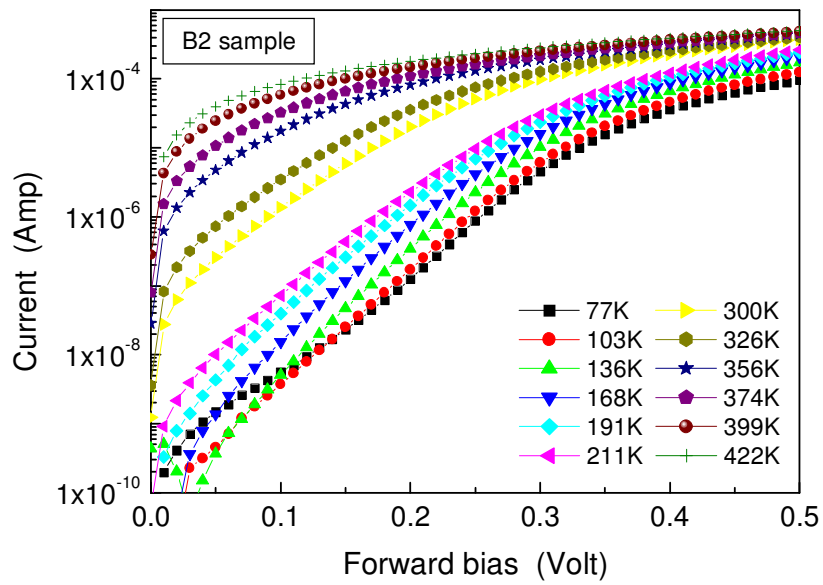


Fig. 3-21 Current-voltage temperature characteristics of Schottky diodes with annealing at 500°C in H₂ ambient (B2 sample)

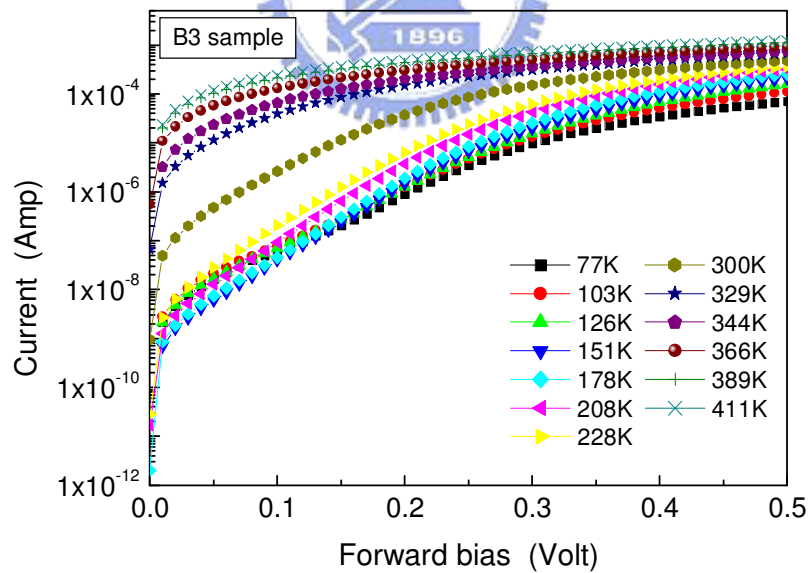


Fig. 3-22 Current-voltage temperature characteristics of Schottky diodes with annealing at 600°C in H₂ ambient (B3 sample)

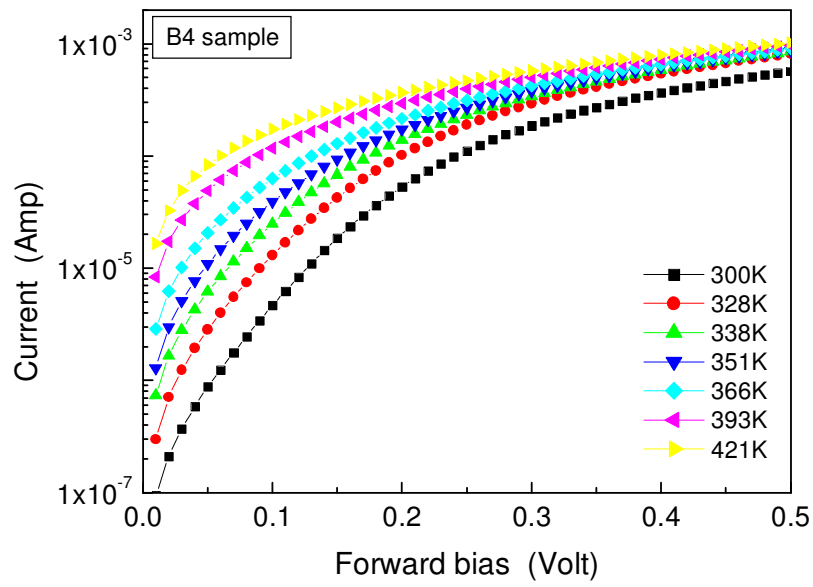


Fig. 3-23 Current-voltage temperature characteristics of Schottky diodes with annealing at 700°C in H₂ ambient (B4 sample)

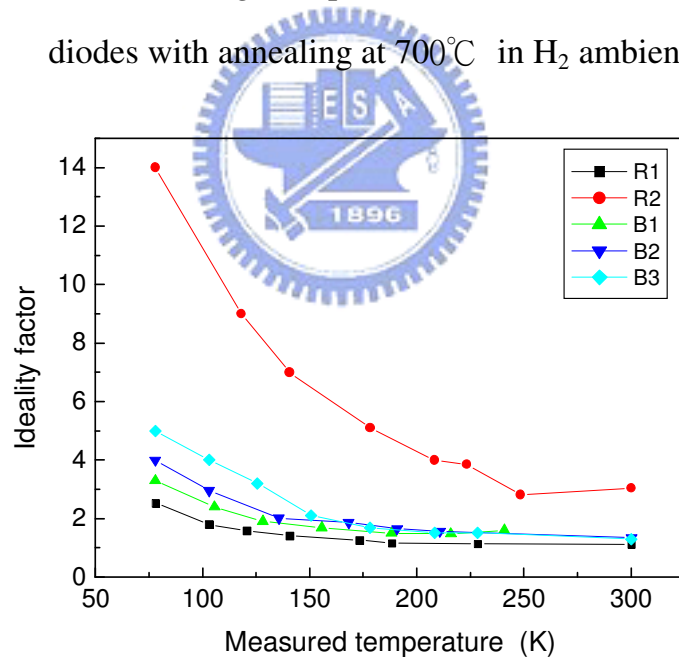


Fig. 3-24 Ideality factor is extracted by measuring at different temperatures for Schottky diodes with annealing in H₂ ambient.

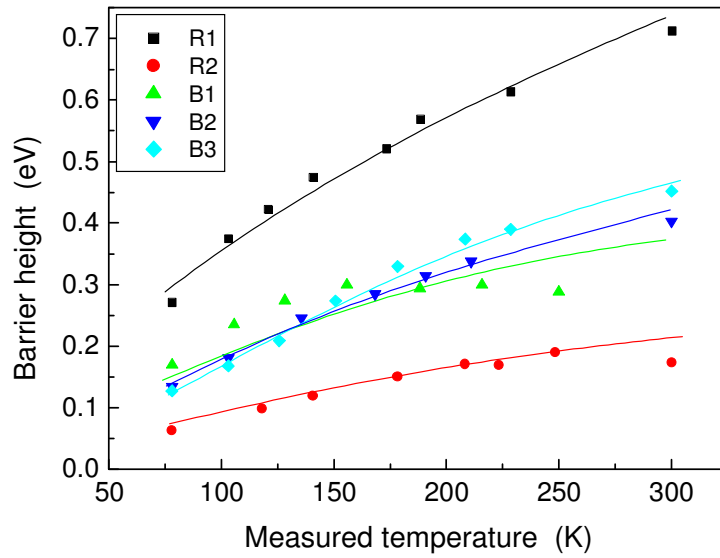


Fig. 3-25 Barrier height is extracted by measuring at different temperatures for Schottky diodes with annealing in H₂ ambient.

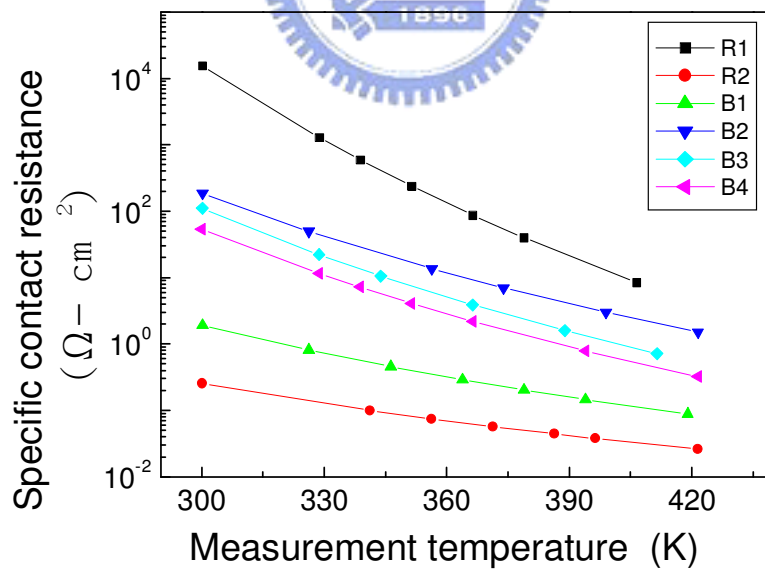


Fig. 3-26 Specific contact resistance of Schottky diodes with different surface treatment in H₂ ambient is shown as a function of temperature.

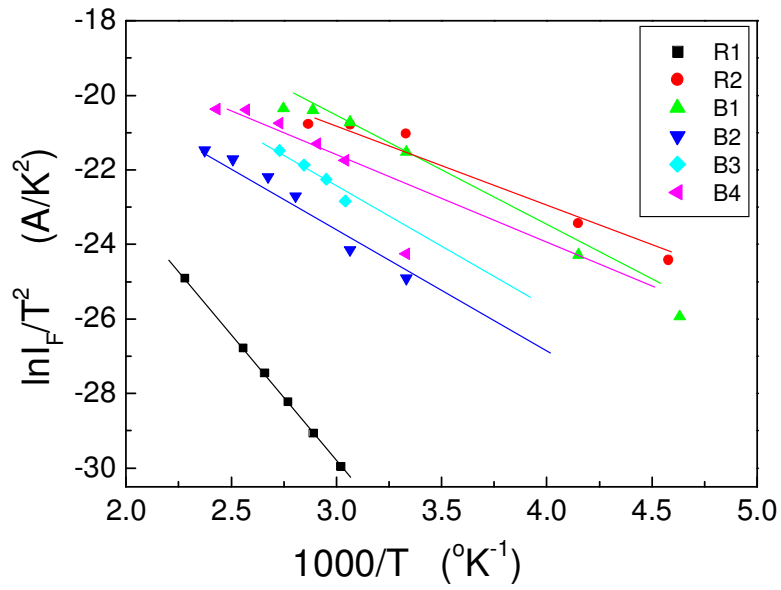


Fig. 3-27 Richardson plot of the Schottky diodes with different surface treatments in H_2 ambient.

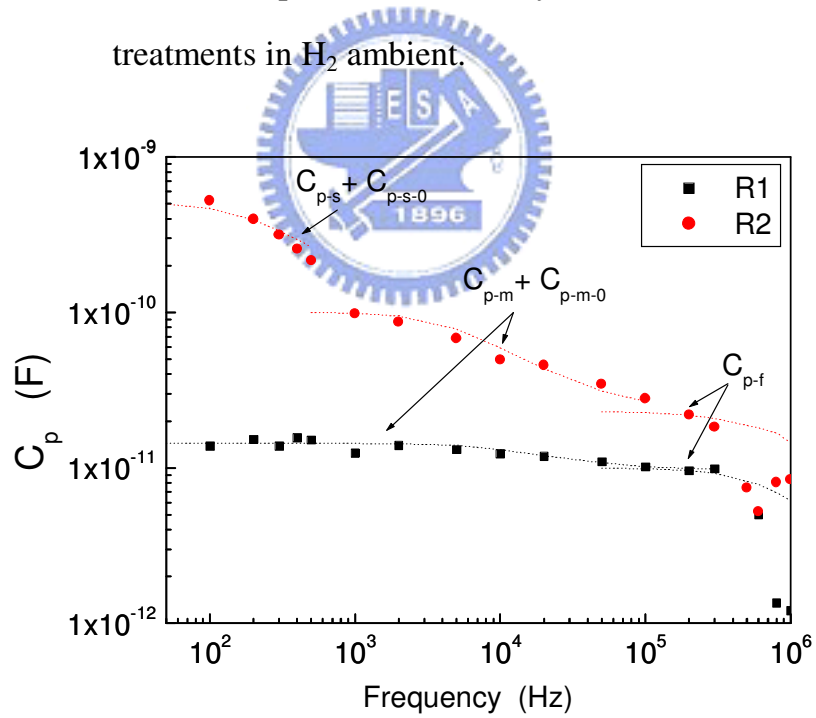


Fig. 3-28 Frequency dependence of the interfacial states capacitance of the Schottky diodes for non-treated sample (R1) and non-annealed ICP-treated sample (R2). The dot line curve represents the fitting result of the experimental data.

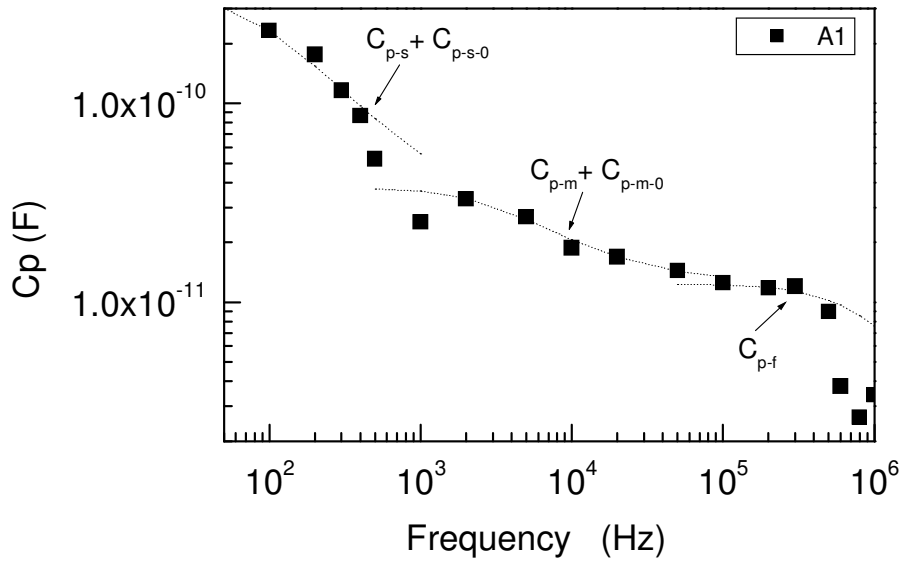


Fig. 3-29 Frequency dependence of the C_p results of the Schottky diodes with annealing at 400°C in N_2 ambient after ICP etching process. The dot line curve represents the fitting results.

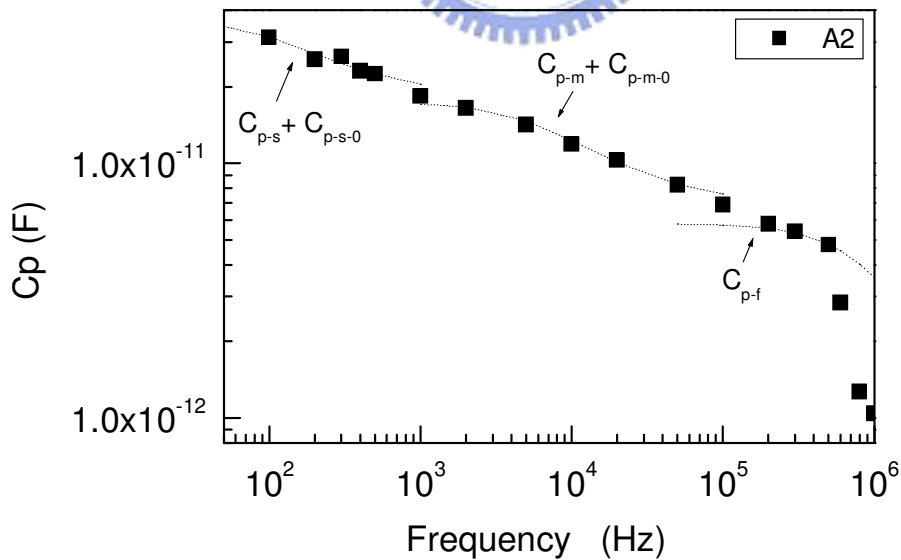


Fig. 3-30 Frequency dependence of the C_p results of the Schottky diodes with annealing at 500°C in N_2 ambient after ICP etching process. The dot line curve represents the fitting results.

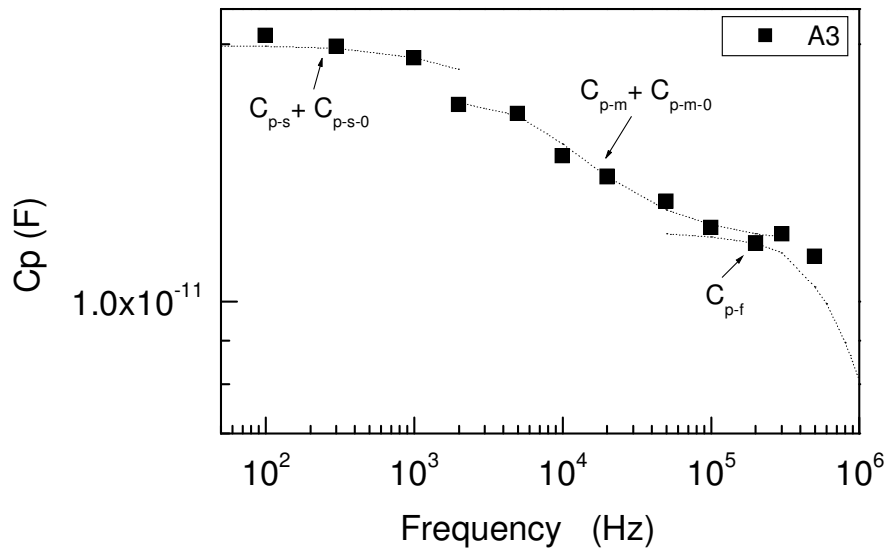
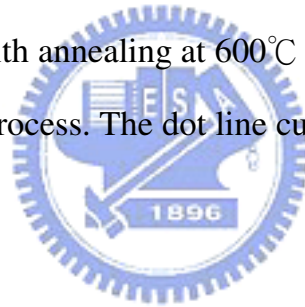


Fig. 3-31

Frequency dependence of the C_p results of the Schottky diodes with annealing at 600°C in N_2 ambient after ICP etching process. The dot line curve represents the fitting results.



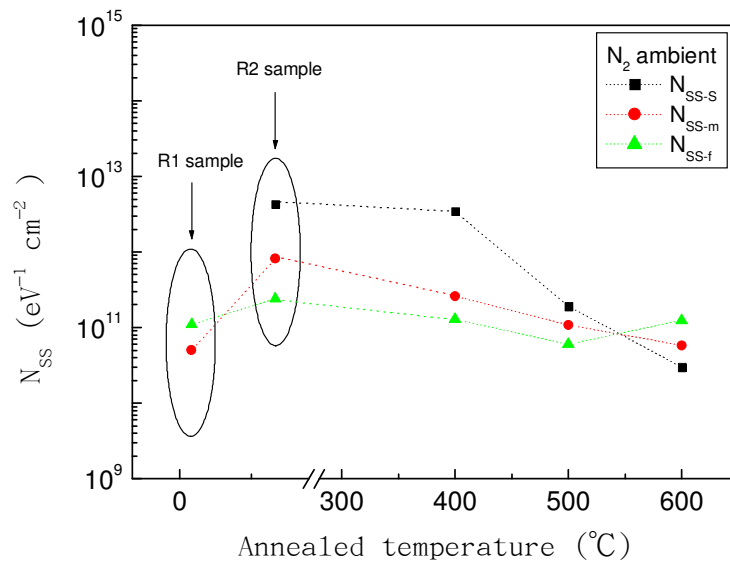


Fig. 3-32 Compared with different types of interfacial states by annealing in N_2 ambient, the interfacial states density as a function of temperature is observed

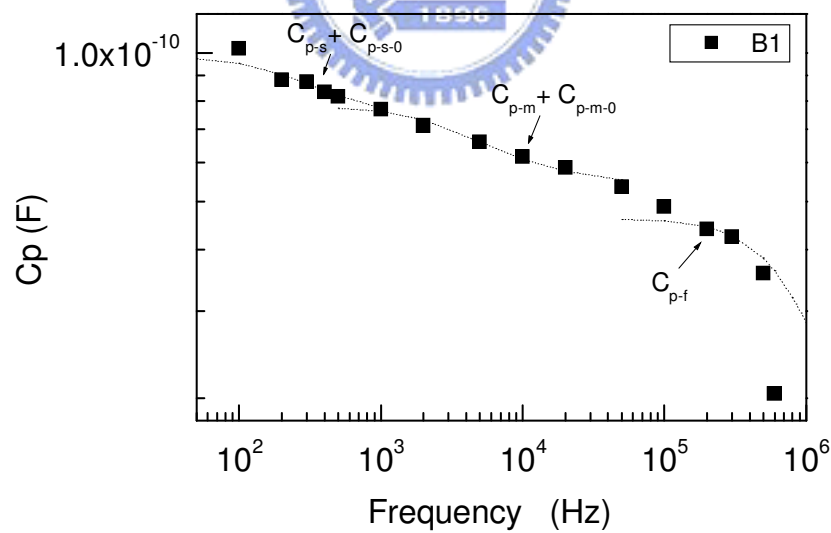


Fig. 3-33 Frequency dependence of the C_p results of the Schottky diodes with annealing at $400^\circ C$ in H_2 ambient after ICP etching process. The dot line curve represents the fitting results.

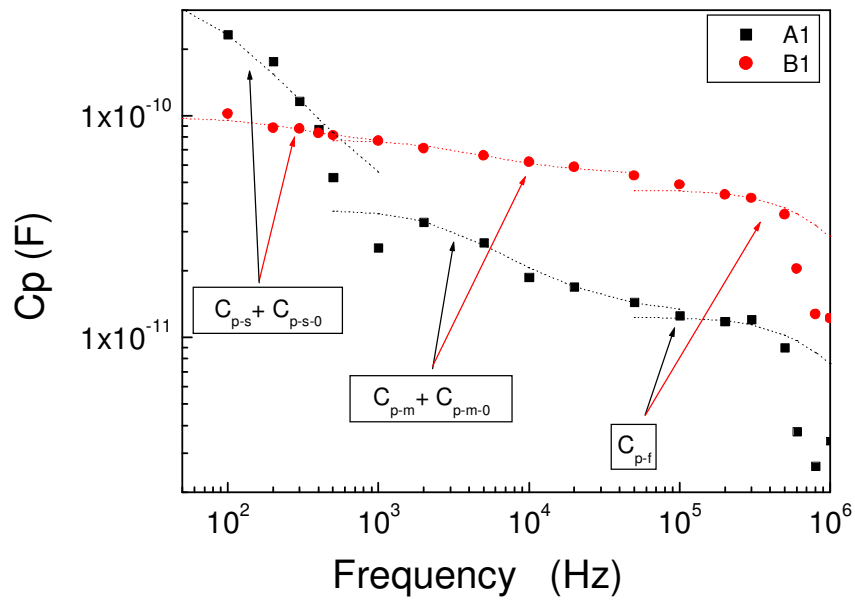


Fig. 3-34 Interfacial state capacitance of A1 and B1 sample by annealing at 400°C

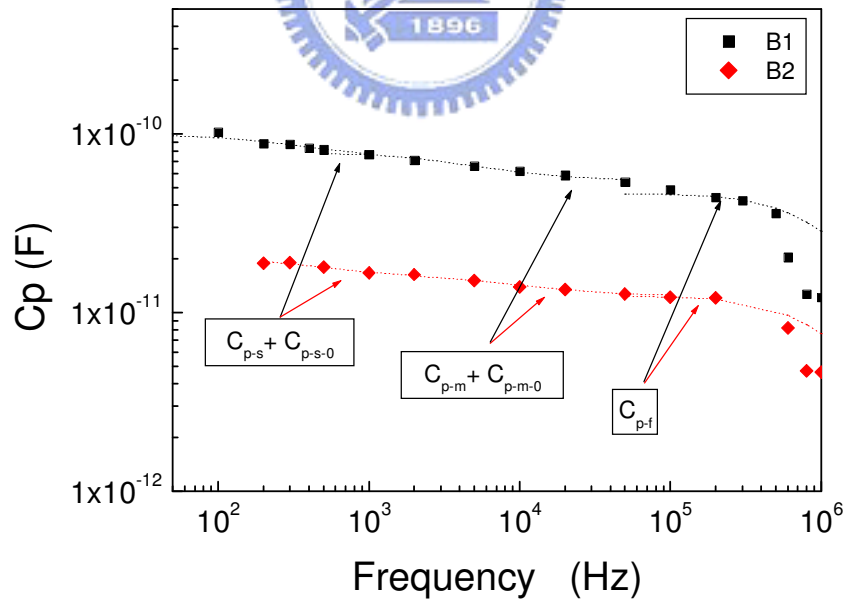


Fig. 3-35 Interfacial state capacitance of B1 and B2 sample by annealing in H_2 ambient

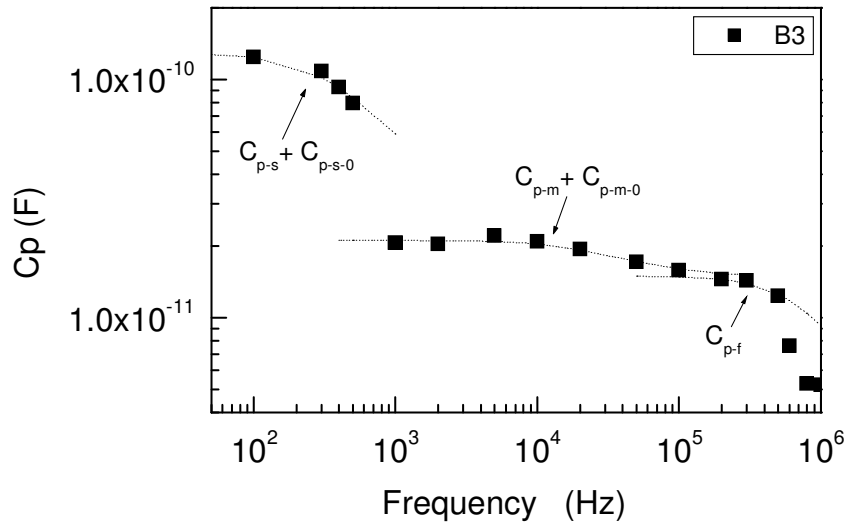


Fig. 3-36 Frequency dependence of the C_p results of the Schottky diodes with annealing at 600°C in H_2 ambient after ICP etching process. The dot line curve represents the fitting results.

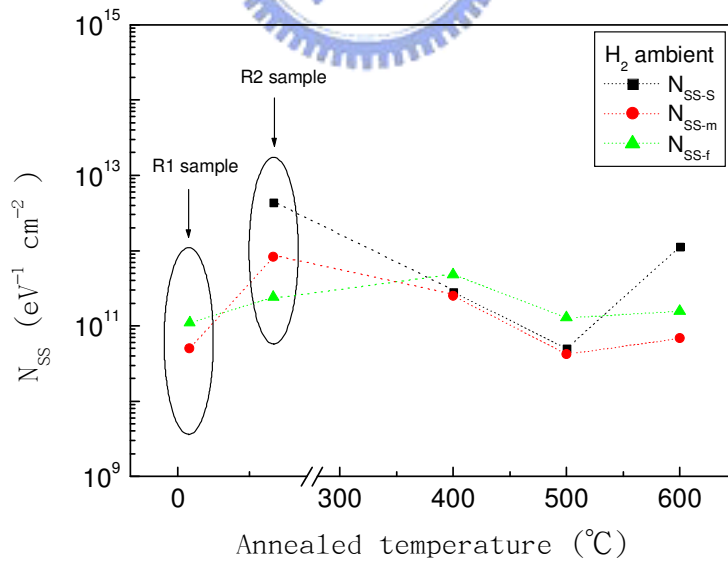


Fig. 3-37 Compared with different types of interfacial states by annealing in H_2 ambient, the interfacial states density as a function of temperature is observed.

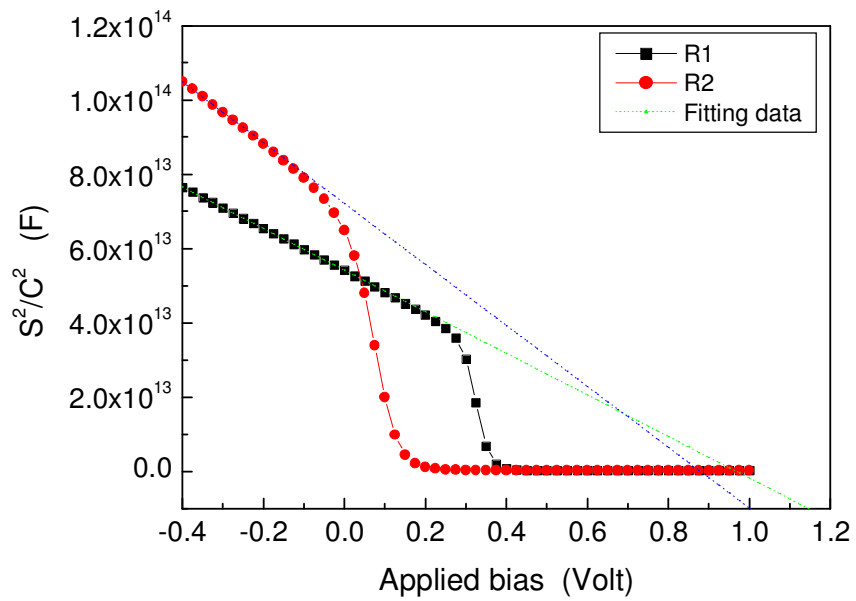


Fig. 3-38 Capacitance voltage characteristics of Schottky diodes with/without ICP treatment. The dot line represents fitting data.

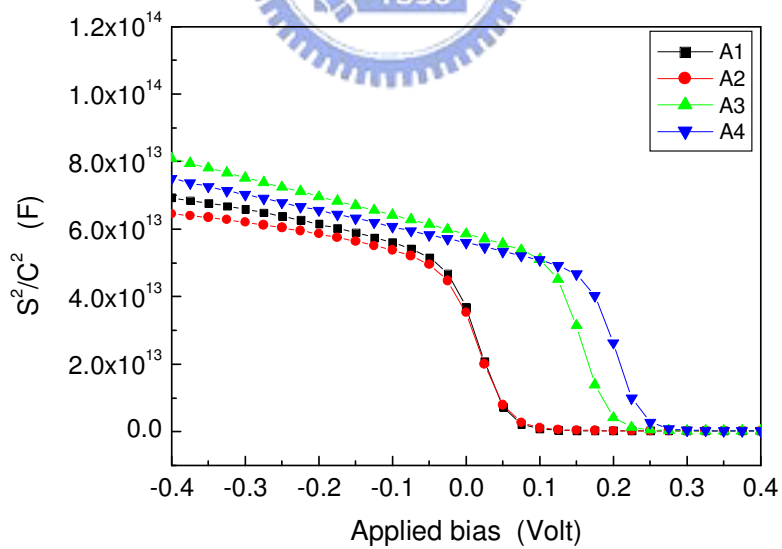


Fig. 3-39 Capacitance voltage characteristics of Schottky diodes with annealing in N_2 ambient at a frequency 1MHz

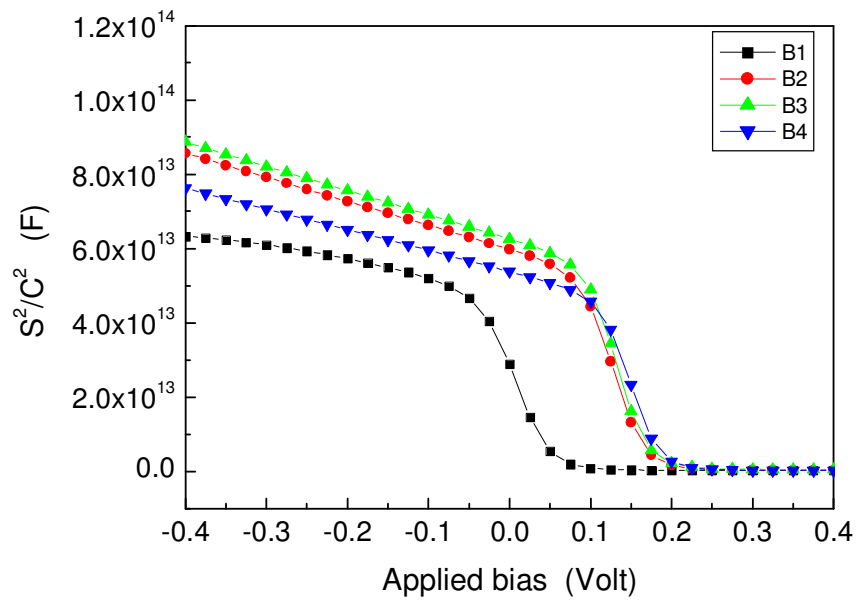


Fig. 3-40 Capacitance voltage characteristics of Schottky diodes with annealing in H_2 ambient at a frequency 1MHz

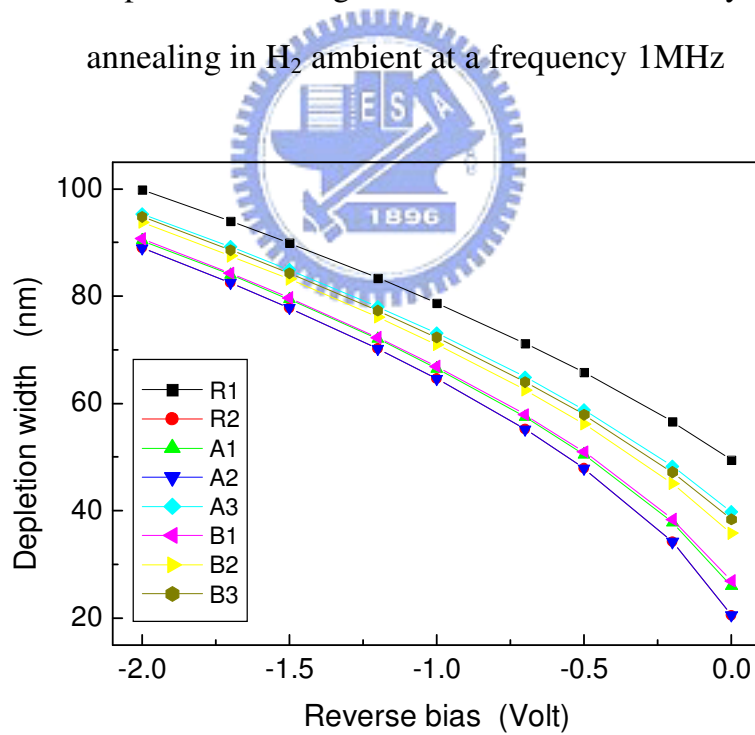


Fig. 3-41 Depletion width of Schottky diodes with different surface treatments

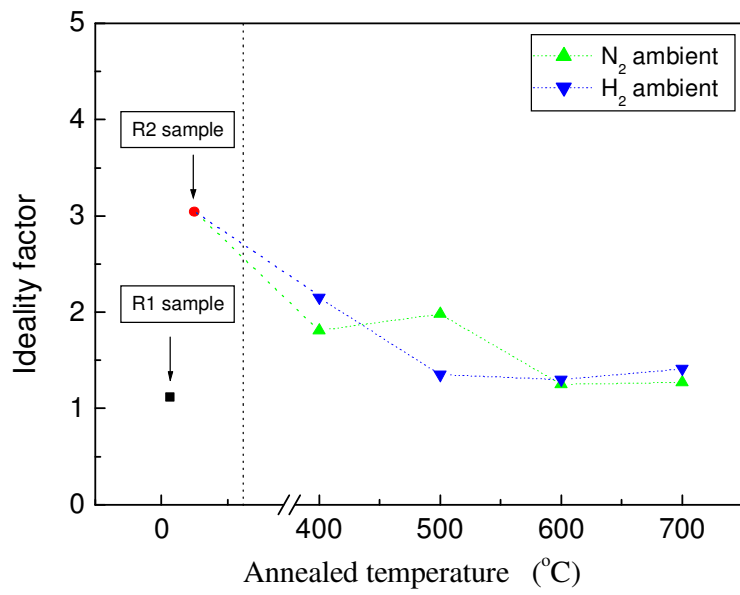


Fig.3-42 Ideality factor is dependent of annealing temperature for different surface treated sample

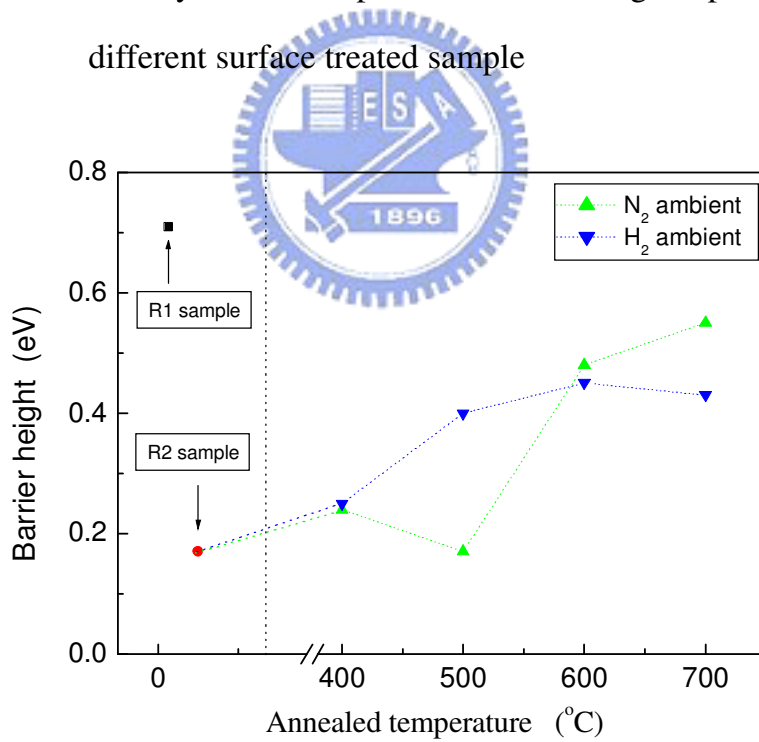


Fig.3-43 Barrier height is dependent of annealing temperature for different surface treated sample

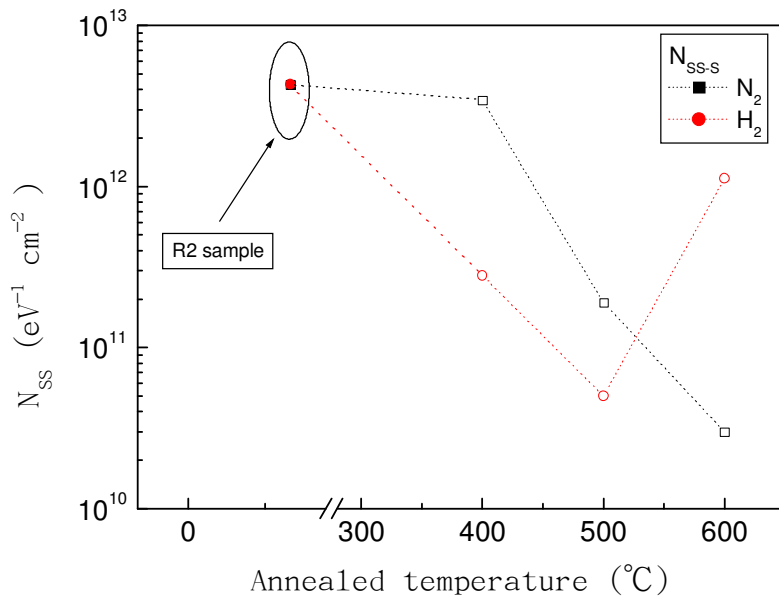


Fig.3-44 s -type interfacial defects is dependent of annealing temperature in N_2 or H_2 ambient.

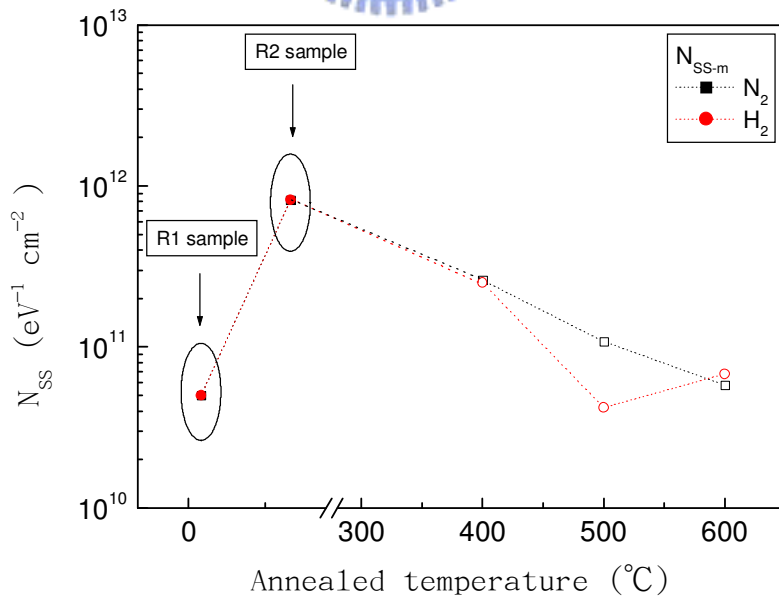


Fig.3-45 m -type interfacial defects is dependent of annealing temperature in N_2 or H_2 ambient.

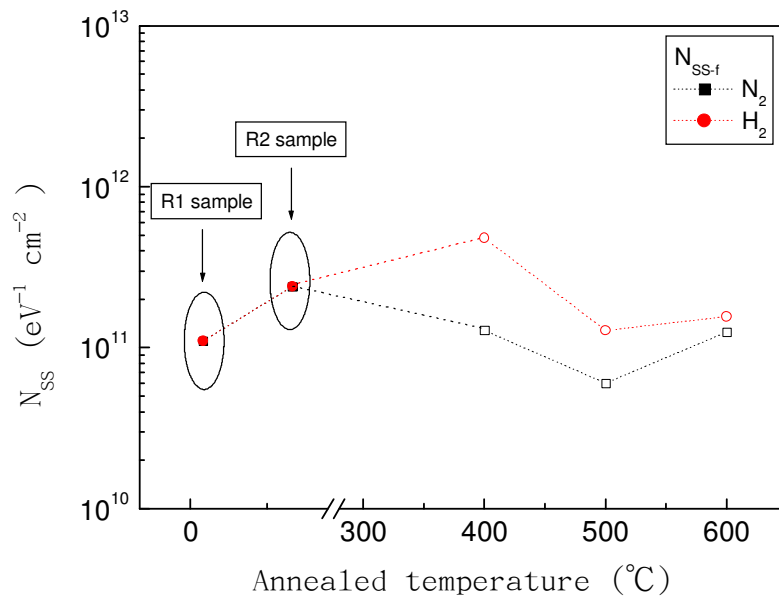


Fig.3-46 f -type interfacial defects is dependent of annealing temperature in N₂ or H₂ ambient.



Chaper 4 Investigation of interfacial states for metal-semiconductor-metal photodetectors (MSM-PDs)

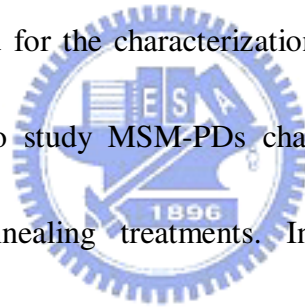
4.1 Introduction

The GaN is wide direct band gap material for fabrication of optoelectronic devices in the visible and the ultraviolet (UV) spectrum. Ultraviolet photodetectors (UV-PDs) with sharp cutoff for visible spectral range is essential to apply in spectroscopy, flame sensing, etc such as photoconductive detector, *p-n* junction PDs, *p-i-n* PDs, Schottky PDs and metal-semiconductor-metal (MSM-PDs). By above mentioned discussion, the results of Schottky diodes with different surface treatments can be applied to metal-semiconductor-metal photodetectors (MSM-PDs). The planar interdigitated electrodes MSM-PDs which is equivalent to a back-to back pair of Schottky diodes consists of a semiconductor and metal electrodes. A metal-semiconductor-metal photodetector (MSM-PDs) can be utilized as a high efficiency photogenerated diode. The MSM-PD is an excellent candidate for fabrication simplicity, geometrical convenience, only a single dopant bulk of the semiconductor, high efficiency and high speed. The MSM-PDs optical and electrical characteristics depend on these parameters such as responsivity and leakage current. The response speed is limited by transit time and RC time due to finger width, length and spacing of interdigitated electrodes. In this work, we have studied the MSM-PDs with different surface treatment to define interfacial states effects in internal gain.

4.2 Surface treatment by annealing in N₂ or H₂ ambient

4.2.1 Internal gain effects for MSM-PDs by surface treatment

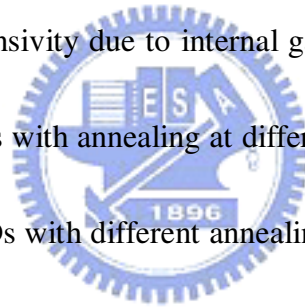
As discussion in Chapter 3, the ICP-induced defects can be reduced to a low level by annealing at temperatures higher than 600°C in N₂ ambient or 500°C in H₂ ambient for 30 min. In H₂ ambient, H₂ may diffuse and chemically react with the defects, changing their electrical properties. Annealing under H₂ ambient is more effective for reduced the defects than that under N₂ ambient. The current transport mechanism changes with the variation of ICP-induced defects. The characteristic energy as well as ideality factor can be used for the characterization. In this study, we apply these results of Schottky diodes to study MSM-PDs characteristics by these interfacial states from ICP or by annealing treatments. In Fig.4-1, the current-voltage characteristics of MSM-PDs without surface treatment (R1 sample) are analyzed by illuminated different photon energies ($h\nu$). The detailed process conditions are listed in Table3-1. As light with photon energy is higher than bandgap energy (GaN~3.4eV) illuminated into MSM-PDs and applied reverse bias, the photogenerated current can be observed. Due to absorption coefficient as discussion in Section 2.2.2.2 (Fig.2-10), the greatest absorption occurs at a cutoff wavelength 360nm for GaN material. In contrast, photocurrent can't be generated as photon energy ($h\nu$) is less than energy bandgap (E_g). Figure 4-2 indicated that the current-voltage characteristics of



MSM-PDs with ICP etching treatment show less than photogenerated current by photon energy ($h\nu$) is more than energy bandgap (E_g). This result may attribute to ICP-induced defects to increase interfacial states density and to cause larger leakage current due to a short absorption length, higher absorption coefficient and absorption lifetime [86]. The light is absorbed on the surface due to interfacial defects states from ICP induced damage. In general, the light could be absorbed in the depletion region between metal and semiconductor by applying reverse bias voltage, and photocarriers are generated. However, as surface states on the semiconductor exist, the light is absorbed on the surface by these surface states, hence short absorption length is observed. On the other hand, the lower barrier height and narrow depletion width (as described in section 3.2.3) is expected for MSM-PDs with ICP etching process (R2 sample), and resulted in less photogenerated current. According to Eq.(2-36) and Eq. (2-37), the responsivity is extracted for MSM-PDs with or without ICP etching treatment as shown in Fig. 4-3.

In order to reduce defects states, the annealing processes methods are employed after samples with ICP etching treatment. The responsivity of MSM-PDs with different annealing temperatures in N_2 ambient is analyzed in Fig.4-4. Compared with MSM-PDs without annealing treatment (R1 and R2 sample), the responsivity MSM-PDs for annealed treated samples (A1, A2 and A3 sample) is around higher one

order of magnitude than the others. This result is opposite to above-mentioned discussion, the Schottky diodes characteristics can be improved by annealing at higher temperature such as higher barrier height, lower ideality factor and interfacial states density (Fig.3-5 and Fig.3-32). In our knowledge, the defects form leakage current and lower devices properties. However, the MSM-PDs with annealing temperature about 400°C in N₂ ambient have greater responsivity in Fig.4-4. The external quantum efficiency of MSM-PDs with annealing treatment after ICP etching process is more than unity. This is contrast to real. Many reports [87]-[96] have discussed that MSM-PDs have higher responsivity due to internal gain. Thus we found and defined the internal gain of MSM-PDs with annealing at different temperatures in N₂ ambient. The internal gain of MSM-PDs with different annealing treatments in N₂ ambient at a wavelength of 370nm by Eq.(2-57) as shown in Fig.4-5. In Eq. (2-57) indicates that s is the finger spacing (20um), w the finger width (10um) for MSM-PDs, r the optical power of reflectance (=0.18 for GaN), α the absorption coefficient around $2 \times 10^4 \text{ cm}^{-1}$ for GaN at a wavelength of 370nm, d the depletion width as shown in Fig.3-41. The greatest internal gain for MSM-PDs with annealing at 400°C in N₂ ambient by applying reverse bias -1.5 Volt and -2 Volt is around 660 and 1733, respectively. To compare with different annealing ambients, the H₂ ambient is employed. The responsivity and internal gain of MSM-PDs with different annealing treatments in H₂



ambient are shown in Fig.4-6 and Fig.4-7, respectively. The internal gain of MSM-PDs with annealing at 400°C in H₂ ambient is more than that with the others. However, as above-mentioned discussion, the interfacial states density for ICP-induced defects can be reduced by annealing temperature more than 500°C in N₂ or H₂ ambient. In other word, the ICP-induced defects by annealing at 400°C in N₂ or H₂ ambient don't been reduced. Thus, the MSM-PDs by ICP etching process and annealing at 400°C in N₂ or H₂ ambient may induce more and more photogenerated carriers and responsivity due to these ICP-induced defects. Carrano et. al [87] had proposed MSM-PDs with high internal gain due to defects or interfacial states between metal and semiconductor and electron can emit or tunnel via these defects states to enhance photogenerated carrier pairs. In this case, we found that the MSM-PDs with greater defects states (A1 and B1 sample) has higher photocurrent, responsivity and internal gain due to these defects states. This result is agreement with Carrano's report. Although Schottky diodes characteristics by annealing at high temperature over 500°C in N₂ or H₂ ambient can be recoverd (i.e. higher barrier height and lower ideality factor), by using surface treatment may not assist with MSM-PDs characteristics in responsivity.

On the other hand, we discussed that the different geometrical structures for MSM-PDs to confirm relationship between internal gain and interfacial states density.

The responsivity characteristics of MSM-PDs with annealing at 400°C in N₂ ambient (A1 sample) is shown in Fig.4-8. The responsivity depends on the finger spacing and reverse bias. As applied reverse bias increasing, the MSM-PDs are operated in the high electric field to induce photogenerated carriers by interfacial states between metal and semiconductor. The internal gain of MSM-PDs with annealing at 400°C in N₂ ambient (A1 sample) is shown as a function of finger spacing and reverse bias as shown in Fig.4-9 and Fig.4-10, respectively. The internal gain is increased by applying reverse bias increasing and is exponential. Figure 4-11 indicates that internal gain of MSM-PDs with different annealing treatments. The MSM-PDs characteristics by annealing in N₂ ambient is better than that by in H₂ ambient. This result may be attributed to interfacial states create by annealing in N₂ ambient, and electrons can emit or tunnel via these states from metal into semiconductor to induce photogenerated carriers.



4.2.2 Persistent photoconductivity effects (PPC) for MSM-PDs with interfacial states

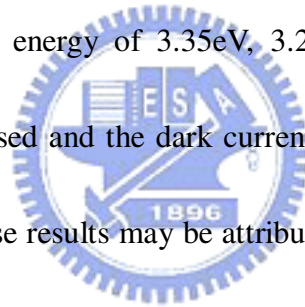
The persistent photoconductivity effects (PPC) in MSM-PDs with interfacial states by annealing treatment have been studied and observed. As light with photon energy ($h\nu$) higher than energy bandgap (E_g) is illuminated, the photocurrent

increases and becomes saturated after a period of time. The recombination phenomena between photogenerated carriers observed by continued illumination into the photocurrent saturated samples. The photogenerated electrons can occupy instable states and induce the photocurrent quenching after the saturation. After the incident light is turned off, the excess holes in the valence band recombine with free electrons which used to contribute to the dark current initially, resulting in the decreased dark current. It is necessary long recovery time that the electrons in the instable states tunnel out the potential barrier. As the photon energy ($h\nu$) less than energy bandgap (E_g), electrons are excited from deep levels or via interfacial states between metal and semiconductor to conduction band where they leak out to the instable states. Recently, many groups have reported the persistent photoconductivity effect (PPC) in n -GaN [97]-[110] and Mg doped p -GaN [111]-[113]. They found that the PPC effect is correlated to holes trap or vacancy, and discussed the trapping mechanism. In this work, we have studied the PPC effect in MSM-PDs with surface treatments.

In Fig.4-12, the dark current voltage characteristics with PPC phenomenon for MSM-PDs with annealing at 500°C in H₂ ambient (B2 sample) is observed by continued step by step measurement. The detailed measured process step with illuminated a photon energy ($h\nu$) 3.35eV for MSM-PDs is depicted in Table 4-1.

As photocurrent characteristics was measured by with illuminated a photon energy

3.35eV (Fig.13), and subsequent the dark current characteristics for MSM-PDs (B2 sample) was measured by without illumination. We found that the dark current and photocurrent could be increased due to by measuring method with continued step by step, hence the PPC phenomenon occurred in this case. The current-time characteristics with a constant reverse bias -2Volt and illuminated a photon energy of 3.35eV, 3.26eV and 3.1eV is utilized to confirm PPC effect as shown in Fig.4-13, Fig.4-14 and Fig.4-15, respectively. The initial dark current was measured by continued measurement to keep stable status, and the photocurrent was measured by incident light with a photon energy of 3.35eV, 3.26eV and 3.1eV provided. The photocurrent gradually increased and the dark current decreased with measured time is observed in the figure. These results may be attributed the presence of holes trap or acceptor-type trap states [100]-[105], [114]-[116]. When incident light is illuminated into the semiconductor, photoexcitation processes can occur due to emission of excited electrons in the metal over the barrier height (thermionic emission; TE) [117]-[119], or tunnel via surface energy level (field emission; FE), band to band excitation of electron hole pairs in the space charge region ($h\nu > E_g$) and pass through deep level ($h\nu > E_g$) as depicted in Fig.17 (a), (b), (c) and (d), respectively. The schematic photoexcitation process in the thermal equilibrium and higher reverse bias condition is illustrated in Fig.4-17, Fig.4-18. As the greater reverse bias applied, higher



probability for photocarriers emitted via deep level into conduction band is expected.

When the light was turned off, the excess holes in the valence band recombine with free electron from photoexcitation carriers, and recovered dark current to achieve stable status with a long time [120]. However, the recovered dark current can not attain to initial value by a long time after illuminated a photon energy of 3.35eV, 3.26eV and 3.1eV. Therefore, the excess holes occur in the valence band and more than photogenerated carriers can be induced due to these energy levels, resulting in greater internal gain and responsivity in MSM-PDs [89], [94]-[97], [103], [121], [122].



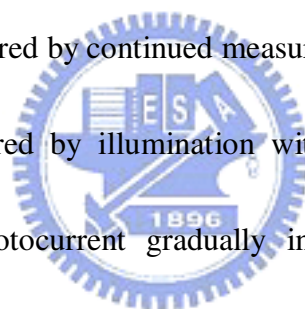
4.3 Summary

In summary, the higher responsivity and internal gain for metal semiconductor metal photodetectors (MSM-PDs) with different surface treatment have been demonstrated and fabricated. As light with photon energy is higher than bandgap energy (GaN~3.4eV) illuminated into MSM-PDs and applied reverse bias, the photogenerated current can be observed. The responsivity of MSM-PDs with or without ICP etching process at a cutoff wavelength of 360nm by applying reverse bias -1Volt is 0.02A/W and 0.001A/W, respectively. However, as the MSM-PDs with ICP etching process are annealed in N₂ or H₂ ambient, the higher responsivity and internal

gain can be observed. The responsivity of MSM-PDs with annealing at 400°C (A1sample), 500°C (A2 sample) and 600°C (A3 sample) in N₂ ambient by applying reverse bias -1Volt is 3.95A/W, 0.72A/W and 1.85A/W, respectively. The internal gain of MSM-PDs with annealing at 400°C (A1 sample), 500°C (A2 sample) and 600°C (A3 sample) in N₂ ambient at a photon energy of 3.35eV by applying reverse bias -1Volt is 195, 36 and 84, respectively. In general, photocurrent can't be generated as photon energy ($h\nu$) is less than energy bandgap (E_g). However, the higher responsivity and internal gain characteristics for MSM-PDs with ICP etching process and annealing in N₂ ambient at different temperatures are clearly observed. This result is attributed to interfacial states such as holes traps what capture or emit electrons or hole as applied higher reverse electrical field and illumination. Moreover, the internal gain for MSM-PDs with annealing in N₂ ambient at 400°C by applying higher -2Volt can achieve to 1734. On the other hand, the same results were in good agreement with the MSM-PDs with annealing at different temperatures in H₂ ambient.

The persistent photoconductivity effects (PPC) in MSM-PDs with interfacial states by annealing treatment have been studied and observed. As light was illuminated on the semiconductor surface, the photocurrent increases and becomes saturated after a period of time. The photogenerated electrons can occupy instable states and induce the photocurrent quenching after the saturation. After the incident

light is turned off, the excess holes in the valence band recombine with free electrons which used to contribute to the dark current initially, resulting in the decreased dark current. It is necessary long recovery time that the electrons in the instable states tunnel out the potential barrier. As the photon energy ($h\nu$) less than energy bandgap (E_g), electrons are excited from deep levels or via interfacial states between metal and semiconductor to conduction band where they leak out to the instable states. We found that the dark current and photocurrent could be increased due to by measuring method with continued step by step, resulting in PPC phenomenon occurred. The initial dark current was measured by continued measurement to keep stable status, and the photocurrent was measured by illumination with a photon energy of 3.35eV, 3.26eV and 3.1eV. The photocurrent gradually increased and the dark current decreased with measured time is observed. These results may be attributed the presence of holes trap or acceptor-type trap states



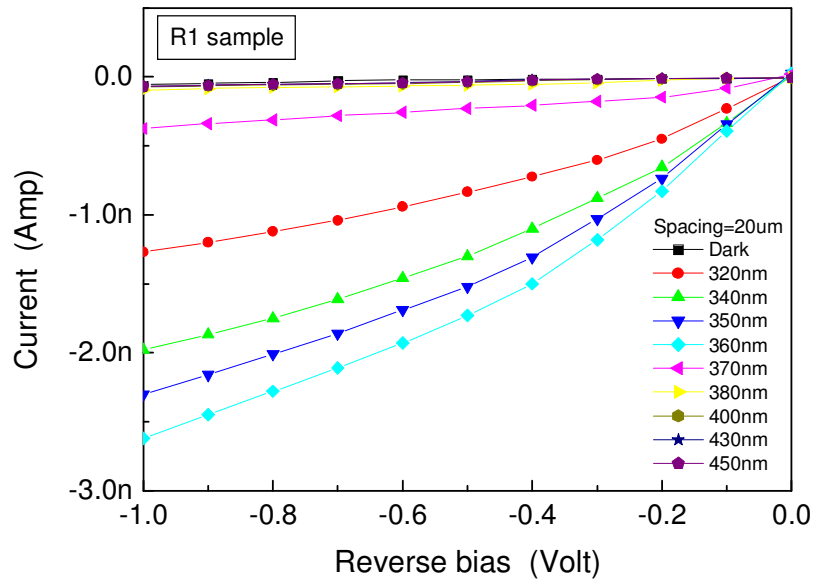


Fig. 4-1 Current voltage characteristics of MSM-PDs without surface treatment

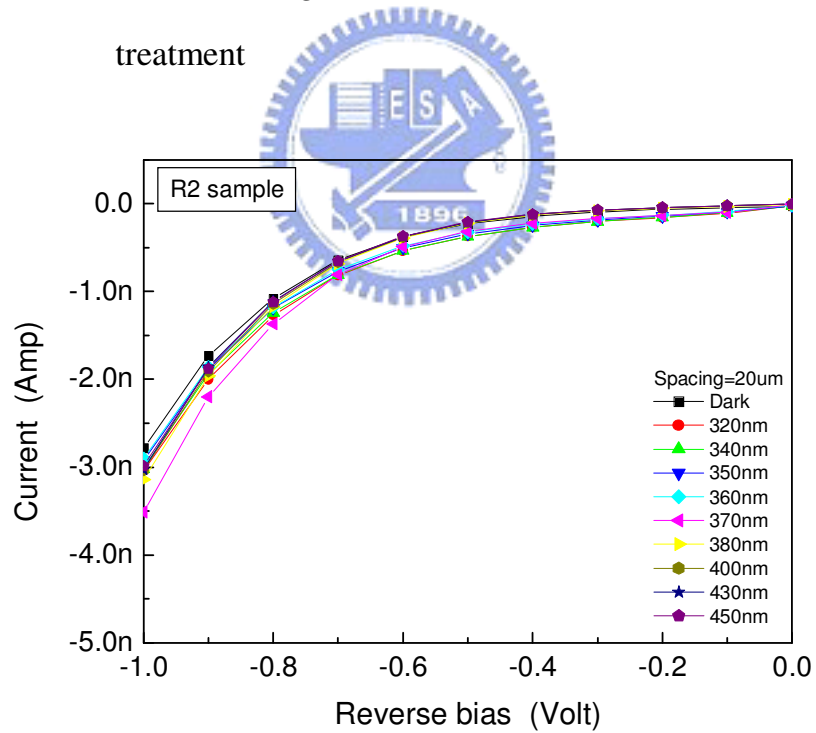


Fig. 4-2 Current voltage characteristics of MSM-PDs with ICP etching treatment

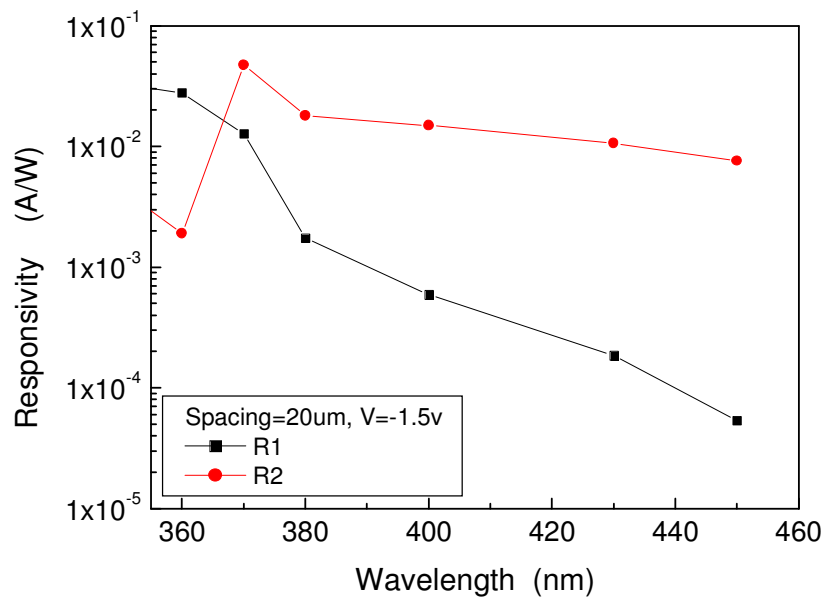


Fig. 4-3 Responsivity of MSM-PDs with/without ICP etching treatment

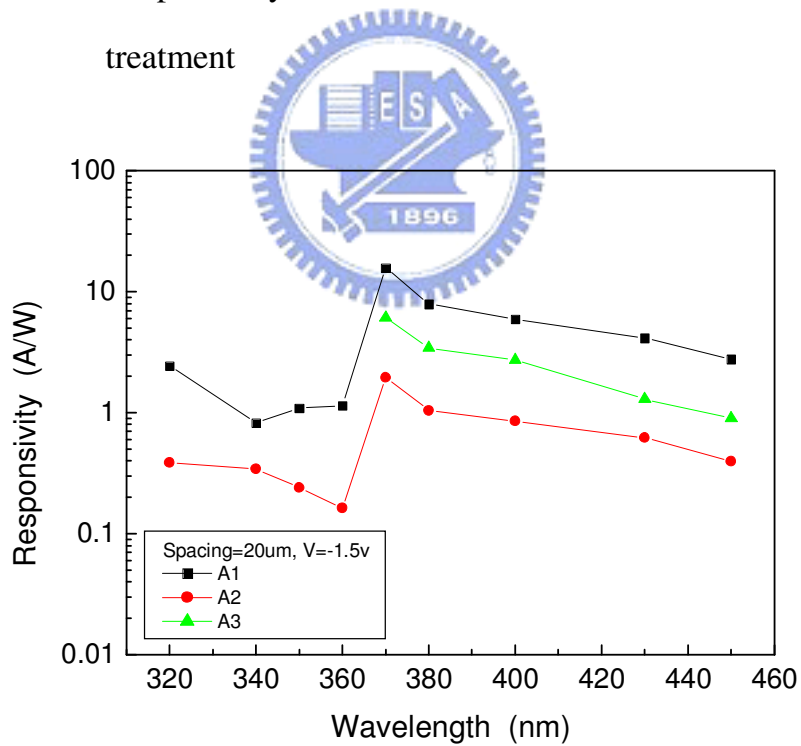


Fig. 4-4 Responsivity of MSM-PDs with different annealing temperatures in N₂ ambient

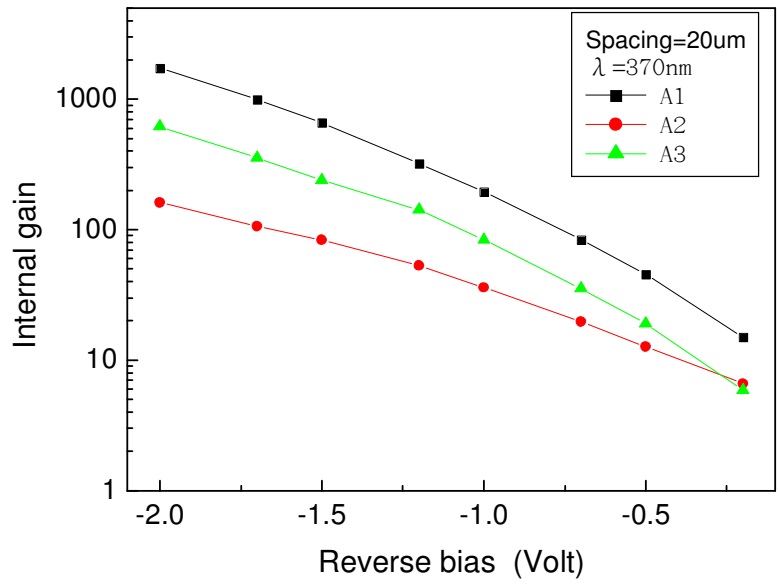


Fig. 4-5 Internal gain of MSM-PDs with annealing at different temperatures in N_2 ambient at a wavelength of 370nm

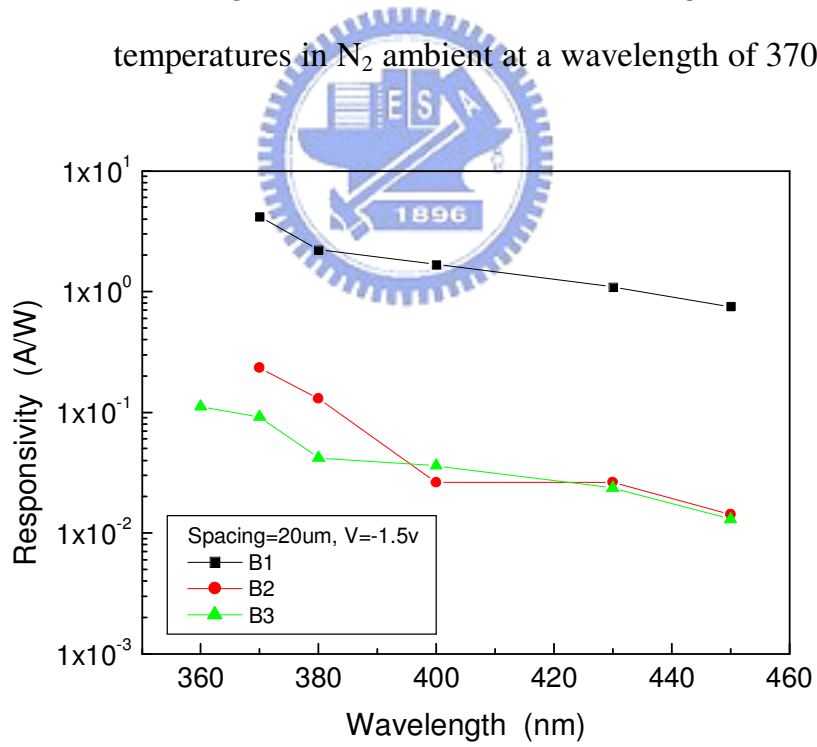


Fig. 4-6 Responsivity of MSM-PDs with annealing at different temperatures in H_2 ambient

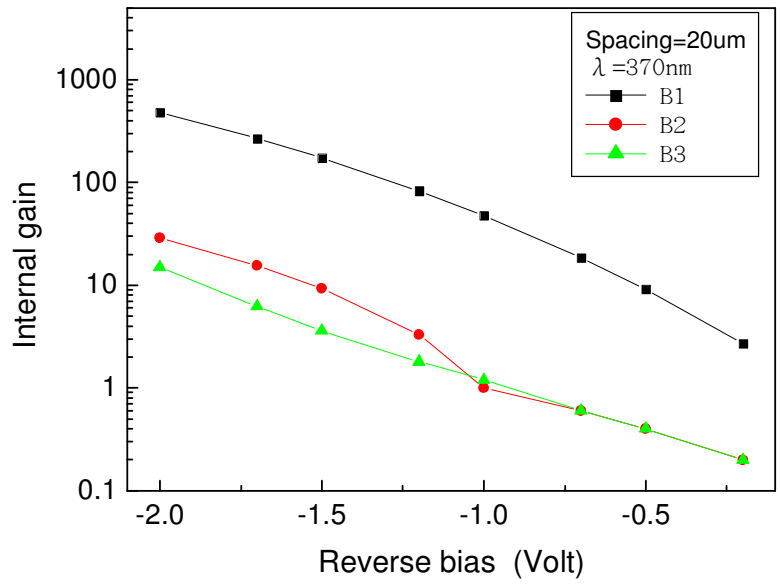


Fig. 4-7 Internal gain of MSM-PDs with annealing at different temperatures in H₂ ambient at a wavelength of 370nm

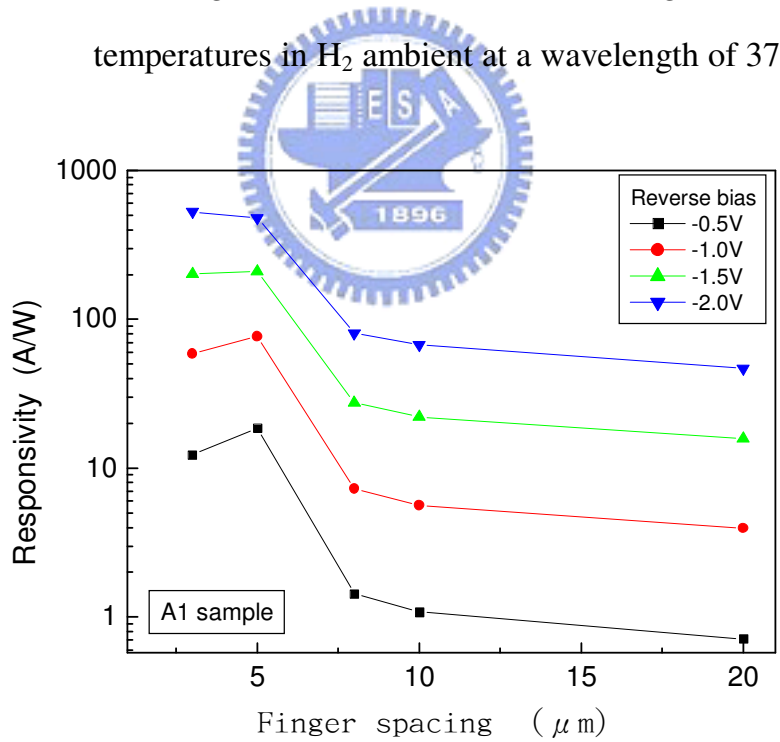


Fig. 4-8 Responsivity of MSM-PDs with annealing at 400°C in N₂ ambient (A1 sample) depend on the finger spacing and reverse bias at wavelength of 370nm.

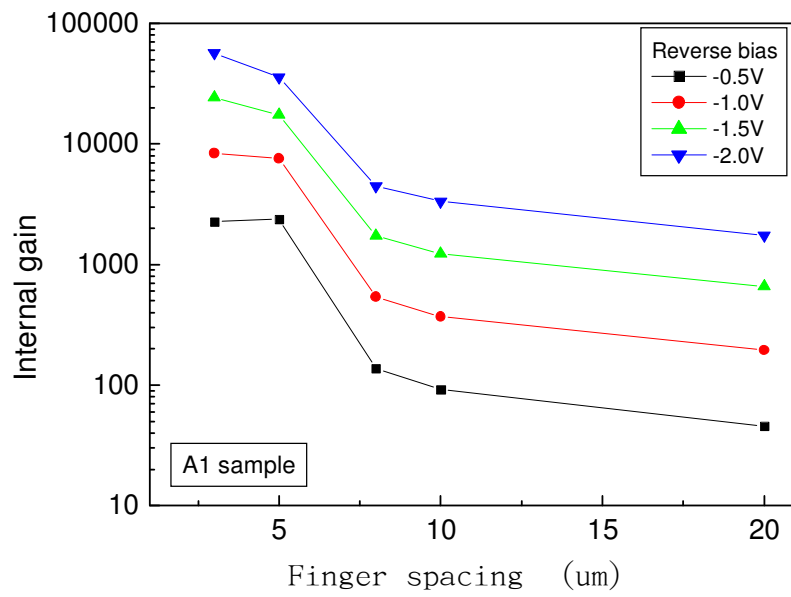


Fig. 4-9 Internal gain of MSM-PDs with annealing at 400°C in N₂ ambient (A1 sample) is depicted as a function of finger spacing at wavelength of 370nm..

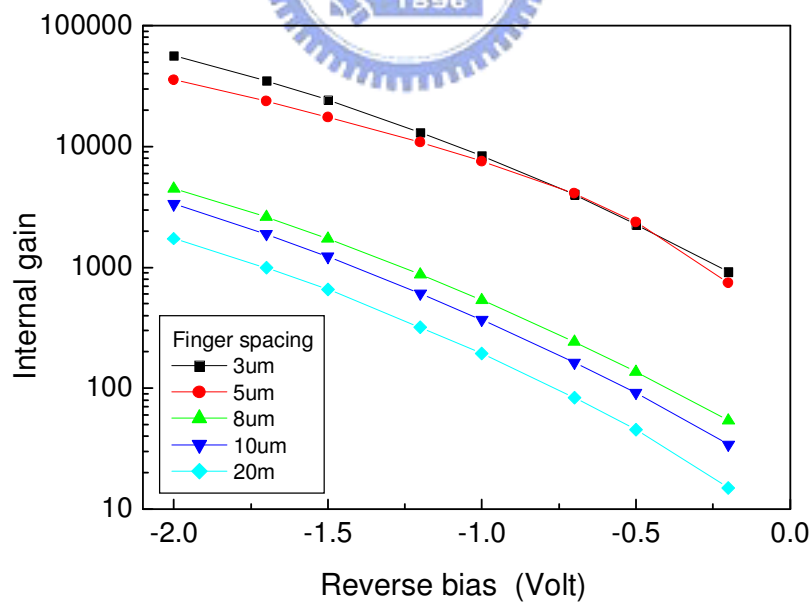


Fig. 4-10 Internal gain of MSM-PDs with annealing at 400°C in N₂ ambient (A1 sample) is depicted as a function of reverse bias at wavelength of 370nm.

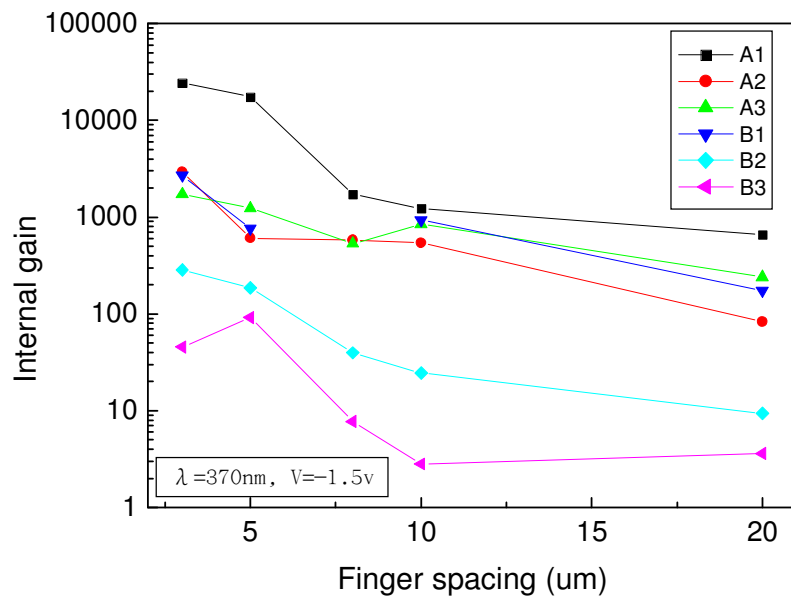


Fig. 4-11

Internal gain of MSM-PDs with annealing at different temperature is depicted as a function of finger spacing at wavelength of 370nm and reverse bias -1.5V.

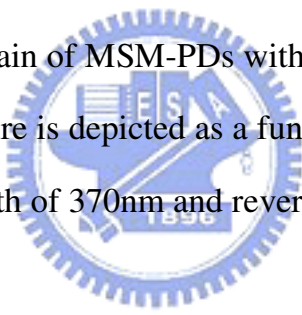
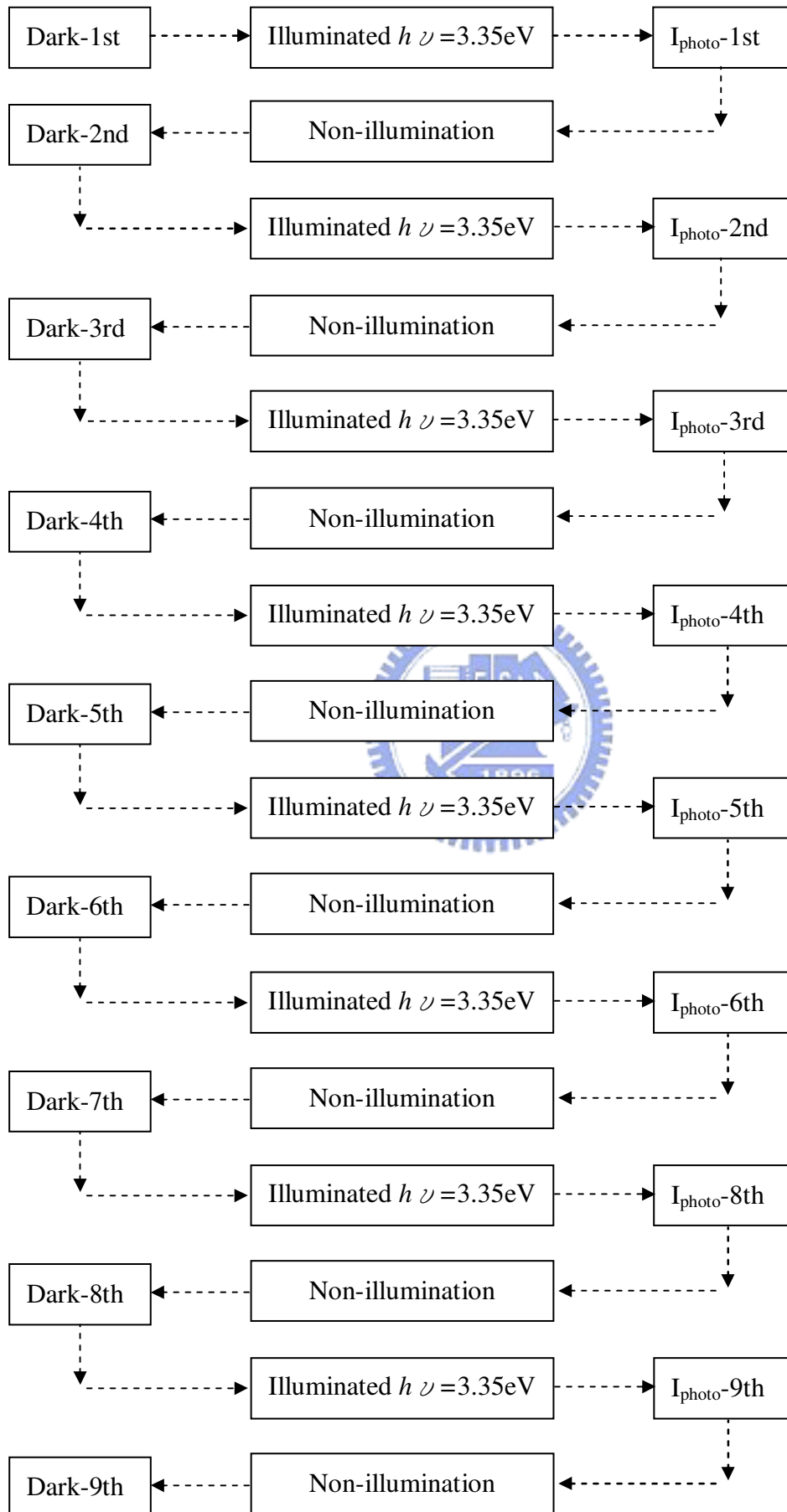


Table 4-1 The detailed process conditions for measured PPC effects



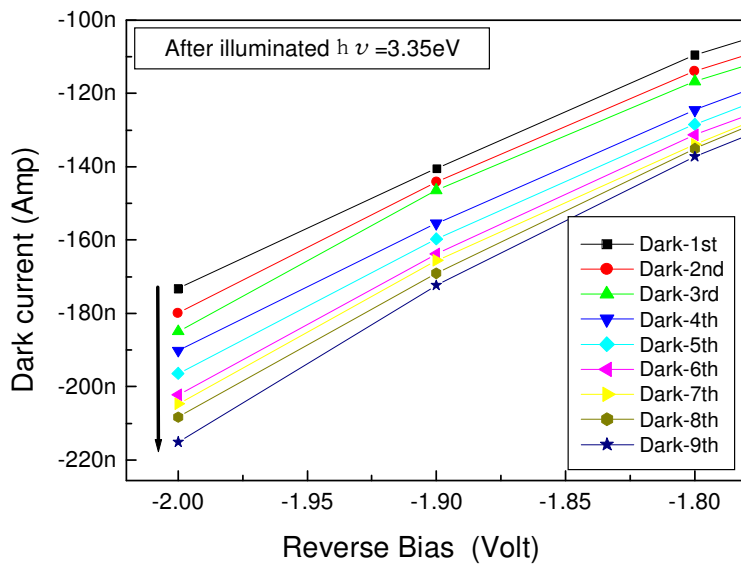


Fig.4-12 Dark current voltage characteristics for MSM-PDs with annealing at 500°C in H₂ ambient (B2 sample). After illuminated a photon energy of 3.35eV, the dark current subsequently was measured without illumination. The detailed measured process flow is described in Table 4-1.

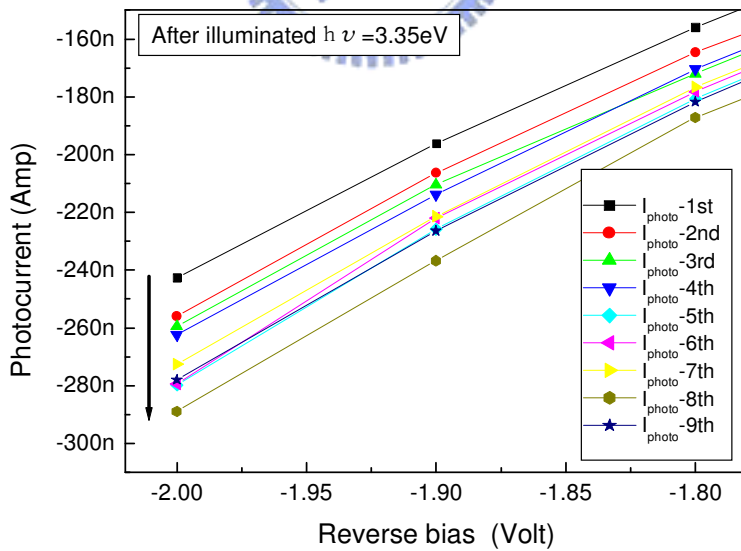


Fig.4-13 Photocurrent with applied reverse bias for MSM-PDs with annealing at 500 °C in H₂ ambient (B2 sample). After illuminated a photon energy of 3.35eV, the photocurrent subsequently was measured by utilized step by step.

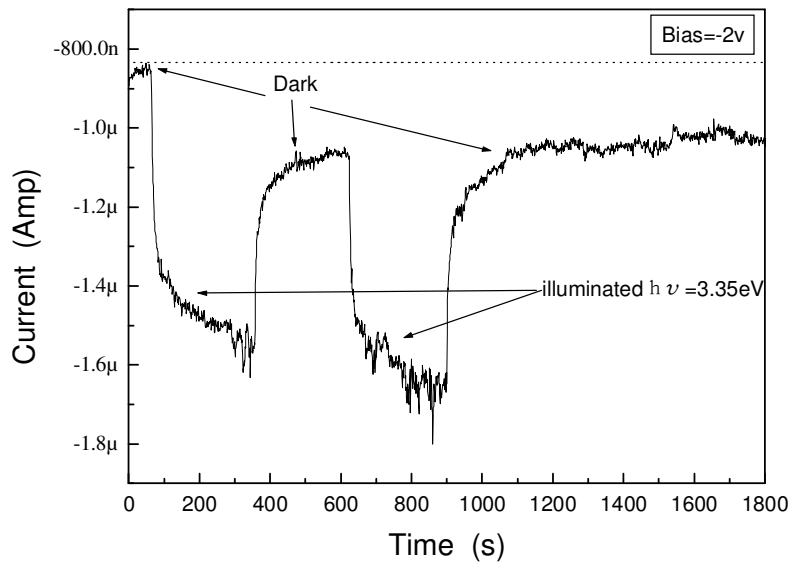


Fig.4-14 The current-time characteristics with a constant reverse bias -2Volt and illuminated a photon energy of 3.35eV.

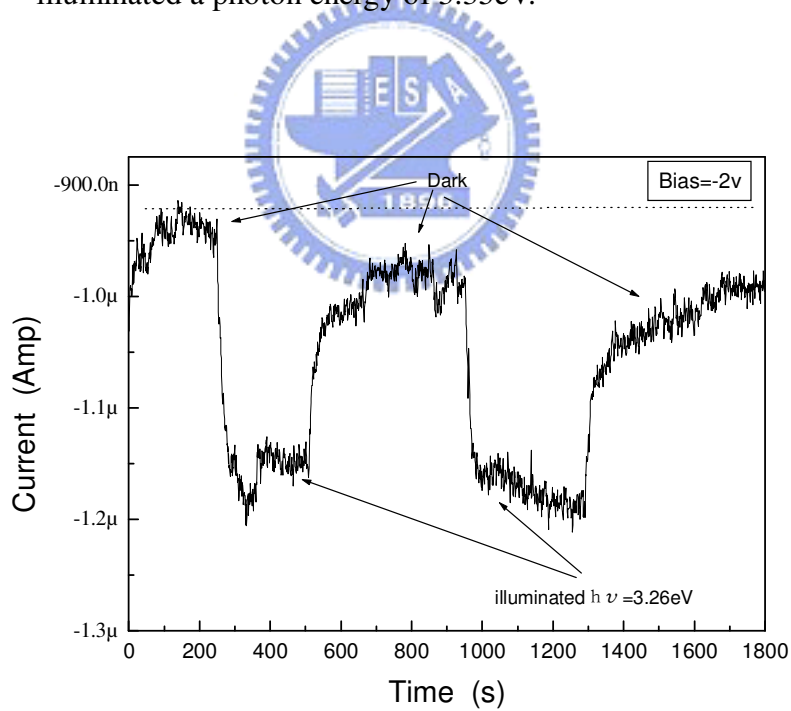


Fig.4-15 Current-time characteristics with a constant reverse bias -2Volt and illuminated a photon energy of 3.26eV.

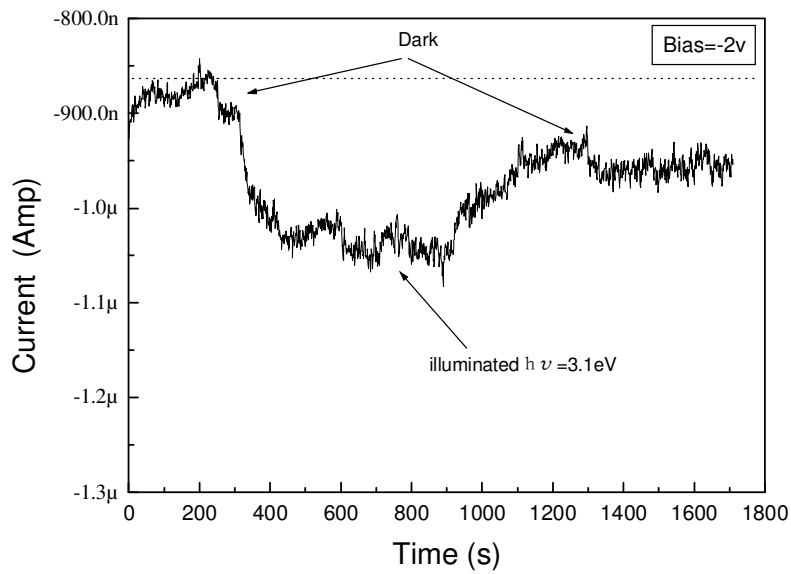


Fig.4-16 Current-time characteristics with a constant reverse bias -2Volt and illuminated a photon energy of 3.1eV.

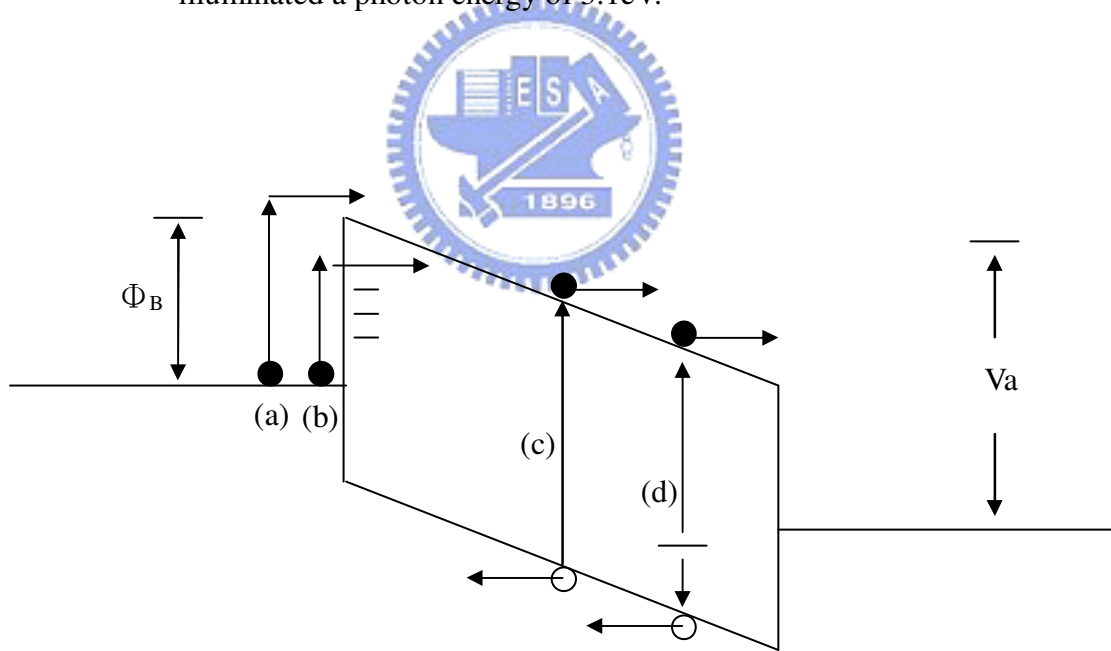


Fig.4-17 Schematic photoexcitation process (a) thermionic emission, (b) field emission, (c) band to band and (d) acceptor level or donor level to conduction band in the thermal equilibrium or applied lower reverse bias.

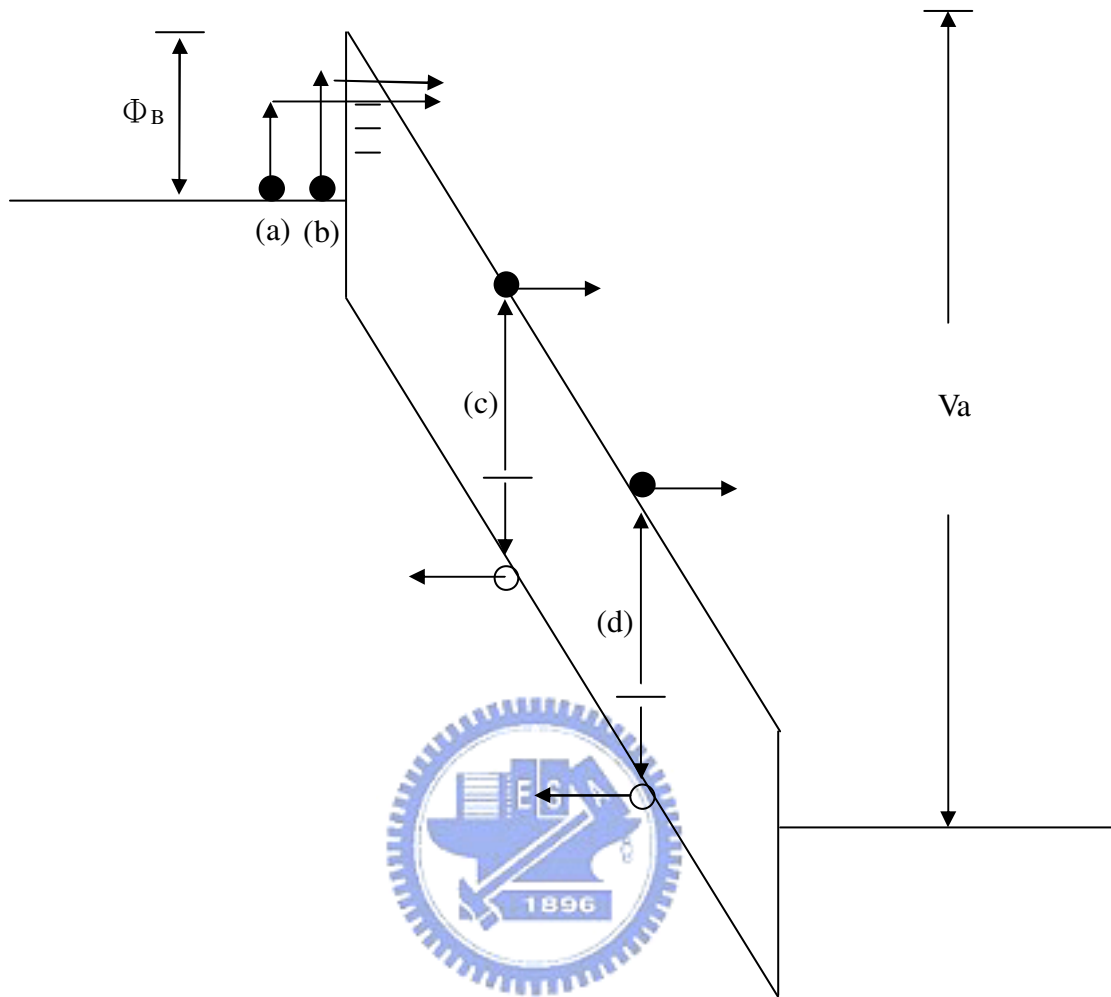


Fig.4-18 Schematic photoexcitation process (a) thermionic emission, (b) field emission, (c) band to band and (d) acceptor level or donor level to conduction band in the higher reverse bias.

Chapter 5 Application of interfacial states for *p-i-n*-photodiodes

Figure 5-1 shows the current-voltage (I-V) characteristics of AlGaIn-based photodiode devices with different annealing gases under the illumination ($0.13\mu\text{W}$) with at a wavelength of 330nm, and the photocurrents are also near a constant at various reverse biases. For the N_2 -treated and H_2 -treated sample, a lower dark current could be observed as shown in inset of Fig.5-1. For the Non-treated PDs, a dark and under illumination (330nm, $0.13\mu\text{W}$) current are increased with the reverse bias increased. Some leakage paths in parallel with the diode may be formed in the Non-treated sample. The ICP induced defects which turn the reverse bias leakage current of AlGaIn-based photodiode devices may create an increase of surface states density and sidewall damage [39].

Comparing to the N_2 -treated and H_2 -treated PDs, the photocurrents are rapidly increased with more than reverse bias voltage 6 Volt for H_2 -treated PDs. Therefore, the external quantum efficiency of the AlGaIn-based photodiode devices for the H_2 -treated PDs may increase more than two times of magnitude comparing to that for the N_2 -treated PDs. These results are attributed to hydrogen interacts with ICP induced defects or formation of dangling bonds on the sidewall or ICP damage areas, after the GaIn is annealed with hydrogen ambient. Hydrogen can create in a number of interfacial states such as bound at donors/acceptors or trapping and recombination centers due to H_2 diffusion and reaction chemically into sidewall or ICP damage areas [81]-[85]. When the bias increases, electrons can tunnel by trap levels, and may be induce more and more photocurrents [97]. To clarify the defects effect, with the illumination of photon energy less than the absorption edge, the results of the illuminated sample could be studied. Figure 5-2 shows the I-V characteristics illuminated with a wavelength of 360nm ($0.23\mu\text{W}$). In the dark and under the

illumination, the I-V curve of the N₂-treated PDs is almost the same. However, comparing to the Non-treated PDs and H₂-treated PDs, some currents under the illumination could be observed. Since the incident photon energy is less than the band gap, these currents could be characterized as the defect-assisted photocurrent or band bending effects. The photocurrent of the H₂-treated PDs at a wavelength of 360nm (0.23μW) is larger than that of the Non-treated PDs. These results are same as above mentioned, and are attributed to trapping and recombination centers due to H₂ diffusion and reaction chemically into the sidewall or ICP damage areas.

Figure 5-3 shows the I-V characteristics illuminated with a wavelength of 400nm (0.4μW). In the dark and under the illumination, the I-V curve of the Non-treated PDs and of N₂-treated PDs is almost the same. Yet, the photocurrent of the H₂-treated PDs is increased in a small amount. This result indicates H₂-induced defects may response at a wavelength of 400nm (3.1eV).

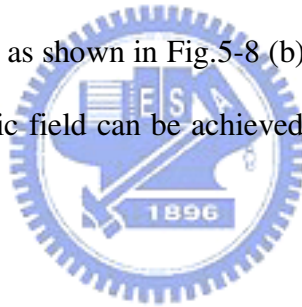
Figure 5-4 shows the spectral response of surface treated samples with different annealing gases under reverse bias voltage 8 Volt. The cutoff wavelength is around 330nm as the absorption of Al_{0.13}Ga_{0.87}N (3.7 eV) for these PDs. For the N₂-treated PDs, there is less surface defects as discussed above, and higher rejection ratio which is around three to four orders of magnitude in the spectral responsivity with annealing at 600°C in N₂ ambient could be achieved,. However, under higher reverse bias, the defect-assisted photocurrent may be enhanced, and it may increase the responsivity in the rejection band. The spectral responsivity at a wavelength of 330nm with annealing at 600°C in H₂ ambient is around 0.1 A/W. It is larger than that with in N₂ ambient, which is around 0.05 A/W. For the H₂-treated PDs, some extra defect levels around 3.4 eV (360nm) can be observed at reverse bias voltage 8 Volt. For the N₂-treated PDs, there is no such level in this case as shown in Fig.5-4.

In order to characterize the surface treated effects, the AlGaIn-based photodiode devices (PDs) with KOH treatment can be also achieved. Figure 5-5 shows the current-voltage (I-V) characteristics for AlGaIn-based photodiodes (PDs) without (“as grown PDs” sample) and with the KOH treatment (“KOH-treated PDs” sample), and the photocurrent of both PDs is also near a constant at various biases voltage. For the KOH-treated PDs, a lower dark current could be observed. For the as grown PDs, a dark current is increased with the reverse bias increased. Under illumination (330nm, 0.7 μ W), for the as grown PDs, the current is increased with bias. Some leakage paths in parallel with the diode may be formed in the as grown sample [23]. Comparing to a stable current for the KOH-treated PDs, these defects may be characterized as the surface defects. To clarify the defects effect, with the illumination of photon energy less than the absorption edge, the results of sample illuminated would be studied. Figure 5-6 shows the I-V characteristics illuminated with a wavelength of 400nm (2.8 μ W). The I-V curve of the KOH-treated PDs taken in the dark and under the illumination is almost the same. Yet, for the as grown PDs, some currents under the illumination could be observed. Since the incident photon energy is less than the band gap, these currents could be characterized as the defect-assisted photocurrent. Thus, lower surface defects could be expected for the KOH-treated PDs.

Figure 5-7 shows the spectral response of as grown and KOH-treated PDs under 0 Volt and reverse bias 10 Volt. The cutoff wavelength is around 335nm as the absorption of Al_{0.13}Ga_{0.87}N (3.7 eV) for both PDs. The responsivity is 0.023 A/W and 0.021A/W for both of as grown and KOH-treated PDs at a wavelength of 330nm. For the KOH-treated PDs, there is less surface defect as discussed above, and less responsivity in the rejection band at 0 Volt can be observed in the figure. Under higher reverse bias, the defect-assisted current may be enhanced, and it may increase the

responsivity in the rejection band. For the as grown PDse, some extra defect levels around 3.4 eV (360nm) can be observed at reverse bias voltage 10 Volt. For the KOH-treated PDs, there is no such level in this case as shown in Fig.5-7.

Figure 5-8 (a) shows the scanning electron microscopy (SEM) images of the AlGa_N-based photodiodes for the as grown PDs after it has been etched to n⁺-Ga_N region. Due to the worse protection of the photo resist during etching process or the worse property of AlGa_N and p-Ga_N, the sidewall with whisker-like features [123] for the as grown PDs can be observed on top of n⁺-Ga_N layer after ICP etched process. These whisker-like features may result from mix and edge dislocations [124], and of diameter are around 50-100nm. Thus, some leakage currents through these whisker-like features can be expected. After the KOH treatment, these whisker-like features can be removed [125] as shown in Fig.5-8 (b). Under the smoother surface on the edge, more uniform electric field can be achieved and less leakage current on the edge can be expected.



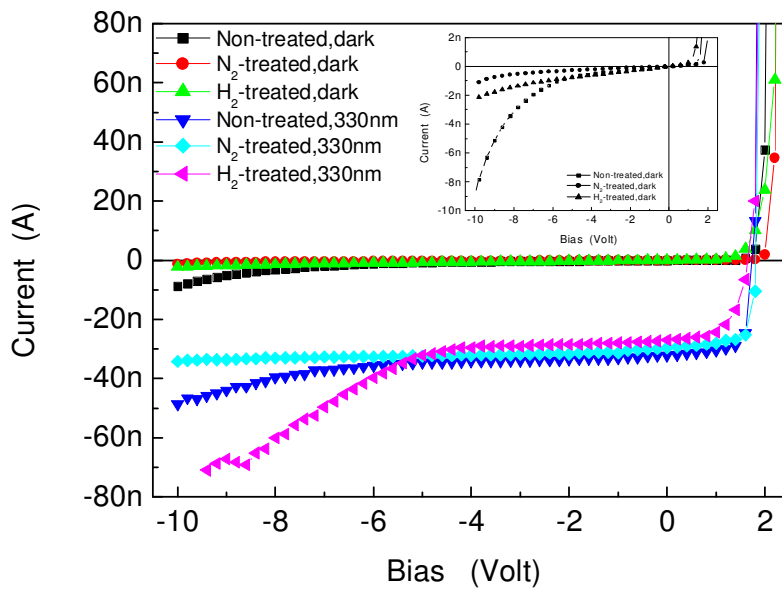


Fig. 5-1 Current-voltage (I-V) characteristics of AlGaIn-based photodiode devices (PDs) with annealing at different gases under the illumination ($0.13\mu\text{W}$) is at a wavelength of 330nm. The insert of figure shows a lower dark current.

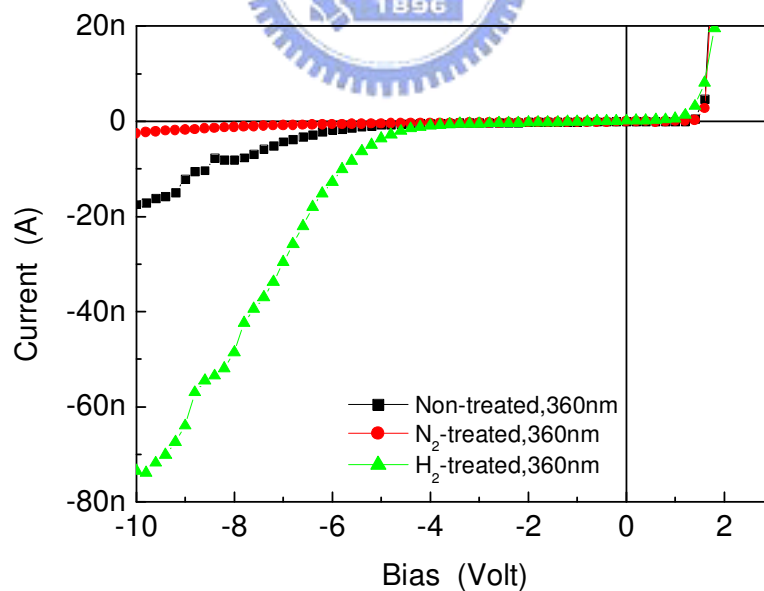


Fig. 5-2 Current-voltage (I-V) characteristics of different annealed treated samples illuminated with a wavelength of 360nm ($0.23\mu\text{W}$).

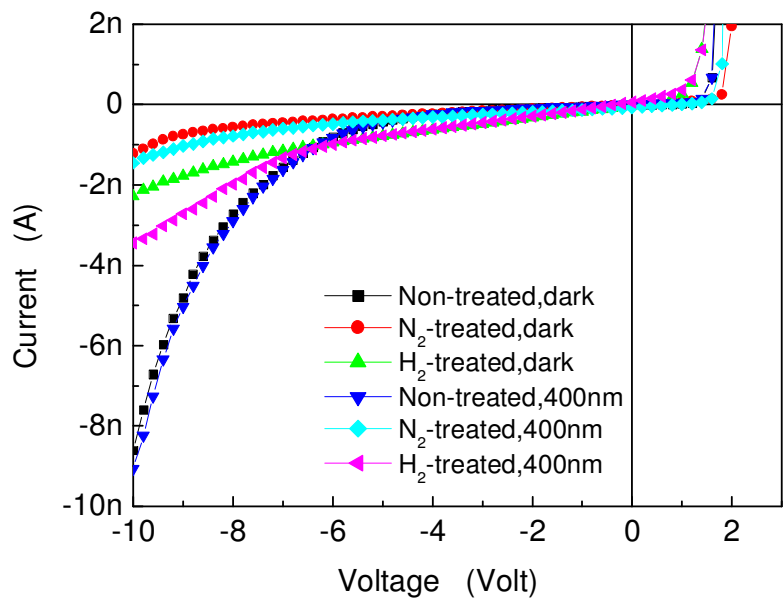


Fig. 5-3 Current-voltage (I-V) characteristics of different annealed treated samples illuminated with a wavelength of 400nm (0.4 μ W).

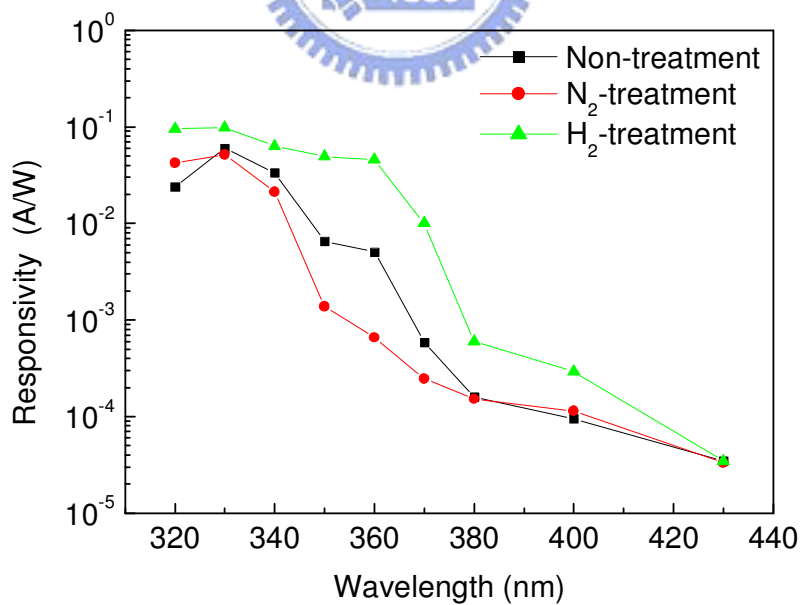


Fig. 5-4 Spectral response of surface treated samples with different annealing ambients under reverse bias voltage -8 Volt.

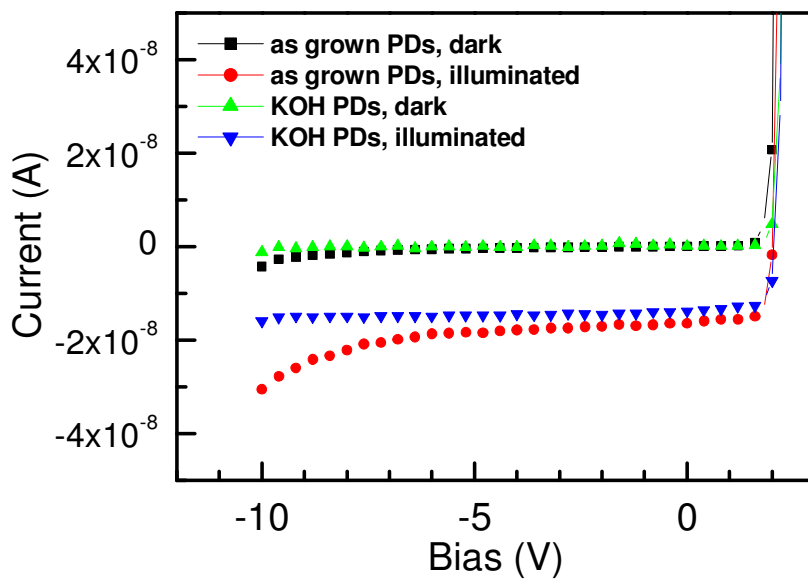


Fig. 5-5 Current-voltage characteristics for as grown and KOH-treated PDs under the illumination ($0.7\mu\text{W}$) with wavelength 330nm

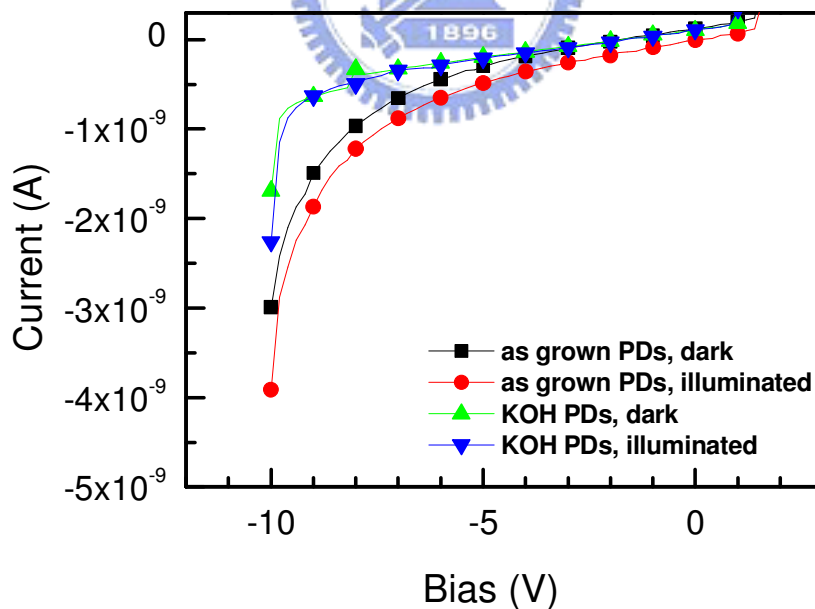


Fig. 5-6 Current-voltage characteristics for as grown and KOH-treated PDs under the illumination ($2.8\mu\text{W}$) with wavelength 400nm

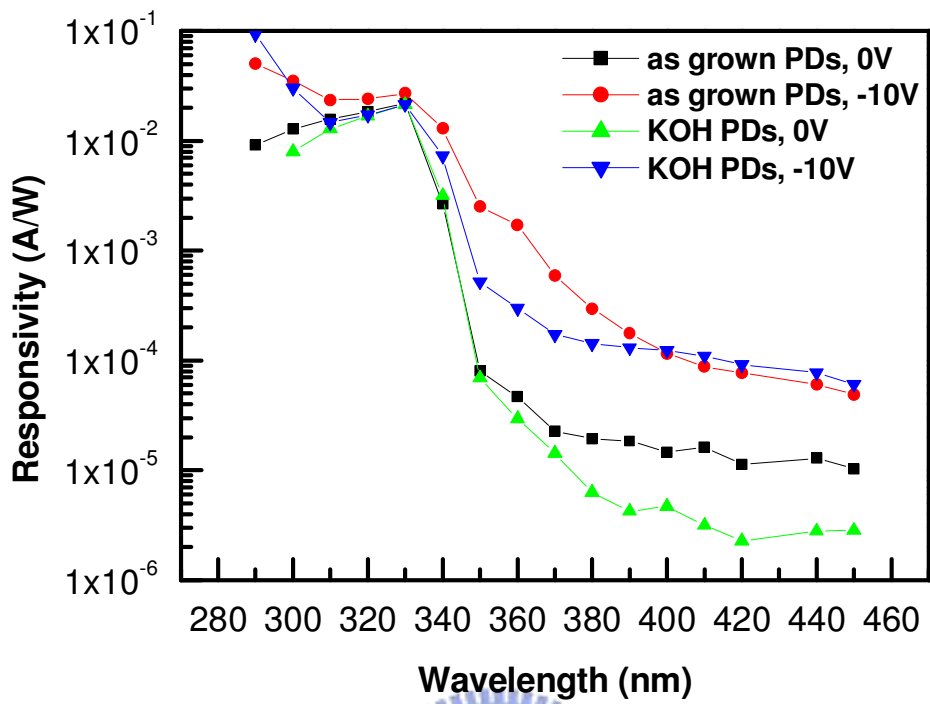


Fig. 5-7 Spectral responsivity for as grown and KOH-treated PDs at different biases



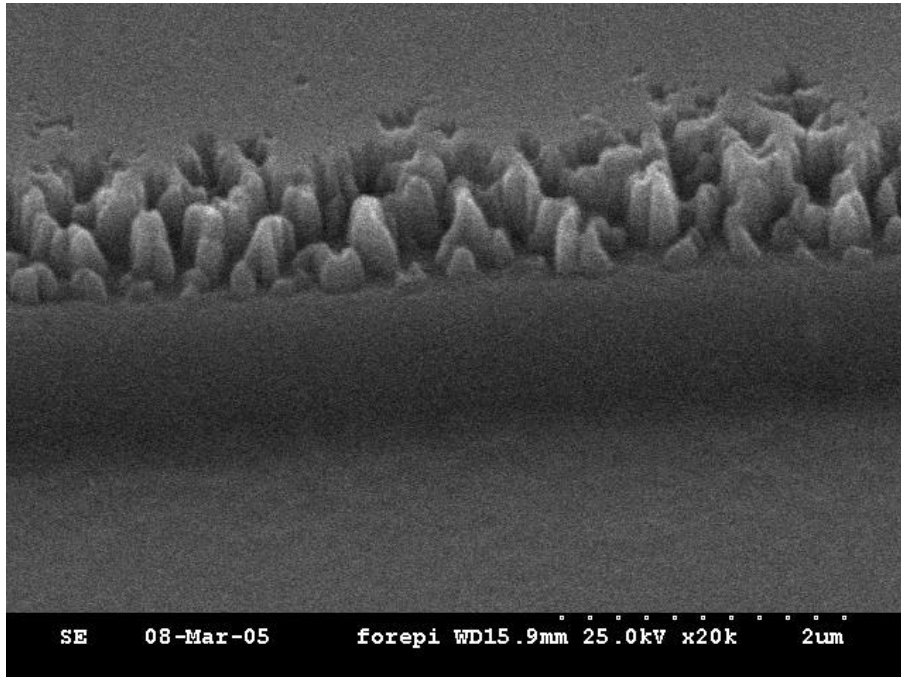


Fig. 5-8(a) Scanning electron microscopy (SEM) images of the AlGaN-based photodiodes for the as grown sample after it has been etched to n^+ -GaN region.

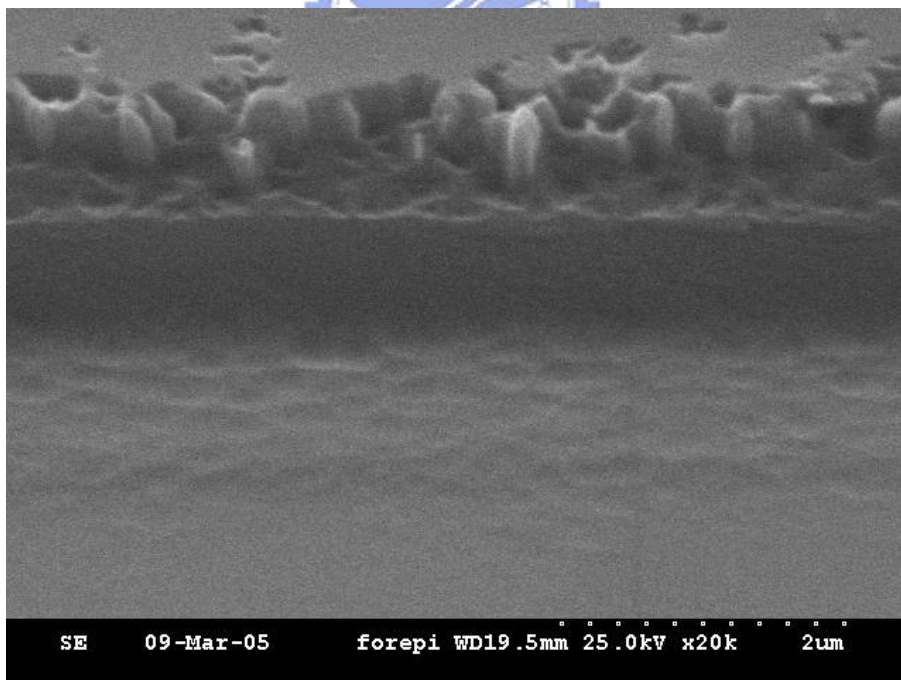


Fig. 5-8(b) Scanning electron microscopy (SEM) images of the AlGaN-based photodiodes for the KOH-treated sample after it has been etched to n^+ -GaN region.

Chapter 6 Conclusions and Future prospects

6.1 Conclusions

The properties of GaN interfacial defects and surface states effects have been characterized in my study. The current transport mechanisms and the thermal stability of Schottky diodes with surface treatments were investigated by employing current voltage temperature (I - V - T) methods. The current transport mechanisms are analyzed in terms of specific contact resistance (ρ_c), characteristic energy (E_{00}) and ideality factor (η) under different annealing temperatures. The current transport mechanisms of non-treated n -type GaN was TE based on the finding that the ideality factor was approximately unity and the characteristic energy was approximately zero. The current transport mechanism was FE based on the finding that the ideality factor and characteristic energy were high due to the ICP etching processes. This indicated the presence of the barrier through which carrier tunneling could take place. Thus, the surface state between GaN and metal could occur by ICP etching and cause carrier tunneling from metal to GaN. However, the current transport mechanisms can be changed from FE to TE by annealing at 600°C in N₂ ambient or 500°C in H₂ ambient for 30 min, that is, the current transport mechanism dominates TE or between TE and FE. These results showed that the ICP damages were reduced to a low level and the Schottky diodes characteristics recovered by annealing 600°C in N₂ ambient or 500°C

in H₂ ambient for 30 min in low ideality factor. We have demonstrated that the current transport mechanisms are directly dependent on the surface treated conditions, and annealing processes are an effective step in eliminating these defects.

On the other hand, we can also characterize the ICP-induced defects by capacitance-frequency (*C-f*) methods. The ICP-induced defects density on the GaN surface has been carried out by *C-f* measurements over a frequency range (100 Hz ~1MHz) at room temperature. The Schottky contacts are investigated by taking into account for the effects of an interfacial layer between the metal and semiconductor. Interfacial states density such as N_{SS-s} , N_{SS-m} and N_{SS-f} for Schottky diodes with different surface treatments is analyzed by capacitance-frequency (*C-f*) methods. The *s*-type interfacial defects can be reduced by annealing temperature increasing to 600°C in N₂ ambient or 500°C in H₂ ambient. The *m*-type interfacial defects can be recovered to non-treated *n*-type GaN (R1 sample) by annealing at high temperature in N₂ ambient or in H₂ ambient. In *f*-type interfacial defects, annealing in N₂ ambient is more effective than that in H₂ ambient. However, the interfacial defects of the Schottky diode with ICP induced defect (R2 sample) by ICP etching process is dominant *s*-type, and non-treated sample (R1 sample) is dominant *f*-type. The worse characteristics of Schottky diodes with ICP induced defect is observed due to *s*-type interfacial defects dominated. Therefore, to reduce *s*-type interfacial defects is anticipated. In this work, we found that the *s*-type interfacial defects can be reduced about one to two order of magnitude by annealing at 500°C in H₂ ambient. The interfacial defects is *f*-type indicating the ICP induced defects nearly recovered to non-treated sample (R1), this is the defects result from epitaxial growth such as dislocation or the others. Besides, the *s*-type defect increases by annealing

temperature at 600°C in H₂ ambient. This result may be attributed to the H₂ may diffuse and react chemically, some hydrogen related defects may be formed, thus they increase the interfacial states. There may be some hydrogen-related defects formed, thus the interfacial state density is increased in this case. Annealing in H₂ ambient is much more effective for removing ICP induced defects rather than that in N₂ ambient.

The higher responsivity and internal gain for metal semiconductor metal photodetectors (MSM-PDs) with different surface treatment have been demonstrated. The responsivity of MSM-PDs with or without ICP etching process at a cutoff wavelength of 360nm by applying reverse bias -1Volt is 0.02A/W and 0.001A/W, respectively. However, as the MSM-PDs with ICP etching process are annealed in N₂ or H₂ ambient, the higher responsivity and internal gain can be observed. The responsivity of MSM-PDs with annealing at 400°C, 500°C and 600°C in N₂ ambient by applying reverse bias -1Volt is 3.95A/W, 0.72A/W and 1.85A/W, respectively. The internal gain of MSM-PDs with annealing at 400°C, 500°C and 600°C in N₂ ambient at a photon energy of 3.35eV by applying reverse bias -1Volt is 195, 36 and 84, respectively. The higher responsivity and internal gain characteristics for MSM-PDs with ICP etching process and annealing in N₂ ambient at different temperatures are clearly observed. This result may attribute to interfacial states such as holes traps what capture or emit electrons or hole as applied high reverse electrical field and illumination. On the other hand, the same results were in good agreement with the MSM-PDs with annealing at different temperatures in H₂ ambient.

The persistent photoconductivity effects (PPC) in MSM-PDs with interfacial states by annealing treatment have been studied and observed. We found that the dark current and photocurrent could be increased due to by measuring method with continued step by step, resulting in PPC phenomenon occurred. The current-time

characteristics with a constant reverse bias -2V and illuminated a photon energy of 3.35eV, 3.26eV and 3.1eV is utilized to confirm PPC effect, respectively. The initial dark current was measured by continued measurement to keep stable status, and the photocurrent was measured by illumination with a photon energy of 3.35eV, 3.26eV and 3.1eV. The photocurrent gradually increased and the dark current decreased with measured time is observed. These results may also attribute to the presence of holes trap or acceptor-type trap states.

6.2 Future Prospects

The III-V Gallium nitride compound semiconductor have attracted a wide range of bandgaps and high temperature stability for optoelectronic and electronic devices such as light-emitting diodes (LEDs), laser diodes (LDs), photoconductive detectors, photovoltaic detectors in the blue-ultraviolet (UV) range of spectrum, and metal-semiconductor field-effect transistors (MESFETs), high electron mobility transistors (HEMTs) in the high temperature/high power electronic devices. In this dissertation, we found that the current transport mechanisms and the thermal stability of Schottky diodes with surface treatments by current voltage temperature (I - V - T) methods and define the interfacial state density of GaN and ICP-induced defects by capacitance-frequency (C - f) methods over a frequency range (100 Hz ~1MHz) at room temperature. For metal semiconductor metal photodetectors (MSM-PDs), the higher responsivity and internal gain for metal semiconductor metal photodetectors (MSM-PDs) with different surface treatment have been demonstrated. The internal gain effects have been interested in devices such as MSM-PDs and p - i - n -PDs due to presence of holes trap or acceptor-type trap states. In our knowledge, interfacial states density such as N_{SS-s} , N_{SS-m} and N_{SS-f} for Schottky diodes with different surface

treatments is analyzed by capacitance-frequency ($C-f$) methods. However, the representation of defects in semiconductor is foreign substitutional, self interstitial, vacancy, stacking fault and edge dislocation precipitate. In future, to confirm the interfacial states defects by ICP-etching process and defects in semiconductor will be investigated and realized. On the other hand, the optoelectric devices such as LED, photovoltaic detectors are fabricated by utilized ICP etching process to define and form p and n type layer. The ICP-induced defects exist in the optoelectric devices and affect the contact resistance and reliability. More mechanisms theories will be studied in the future.



Appendix A. References

- [1] Sang-Mook Kim, Young-Moon Yu, Jong-Hyub Baek, Seong-Ran Jeon, Hyo-Jin Ahn and Ja-Soon Jang, *J. Electrochem. Society*, 154, pp.H384, (2007).
- [2] Shui-Hsiang Su, Cheng-Chieh Hou, Meiso Yokoyama, Ruei-Shiang Shieh, and Shi-Ming Chenb, *J. Electrochem. Society*, 154, pp.J155, (2007).
- [3] Hyunsoo Kim, Jaehee Cho, Jeong Wook Lee, Sukho Yoon, Hyungkun Kim, Cheolsoo Sone, Yongjo Park and Tae-Yeon Seong, *Appl. Phys. Lett.*, 90, pp. 161110, (2007).
- [4] Dae-Seob Han, Ja-Yeon Kim, Seok-In Na, Sang-Hoon Kim, Ki-Dong Lee, Bongjin Kim, and Seong-Ju Park, *IEEE Photon. Technol. Lett.*, 18, pp.1406, (2006).
- [5] Yukio NARUKAWA, Junya NARITA, Takahiko SAKAMOTO, Kouichiro DEGUCHI, akao YAMADA and Takashi MUKAI', *Jpn. J. Appl. Phys.*, 45, pp. L1084, (2006).
- [6] Shingo MASUI, Kazutaka TSUKAYAMA, Tomoya YANAMOTO, Tokuya KOZAKI, Shin-ichi NAGAHAMA and Takashi MUKAI, *Jpn. J. Appl. Phys.*, 45, pp. L1223, (2006).
- [7] K. Kojima, M. Funato, Y. Kawakami, S. Nagahama, T. Mukai, H. Braun and U. T. Schwarz, *Appl. Phys. Lett.*, 89, pp.241127, (2006).

- [8] Shigefusa F. Chichibu, Takashi Azuhata, Mutsumi Sugiyama, Hisayuki Nakanishi, Takayuki Sota and Takashi Mukai, *J. Vac. Sci. & Technol.*, B19, pp.2177, (2001).
- [9] Xu Jintong, Tang Yinwen, Li Xiangyang, Gong Haimei, *Proc. of SPIE*, 5964, pp. 59640Z, (2005)
- [10] J. K. Sheu, M. L. Lee and W. C. Lai, *Appl. Phys. Lett*, 87, pp. 043501, (2005).
- [11] H. Jiang, N. Nakata, G. Y. Zhao, H. Ishikawa, C. L. Shao, T. Egawa, T. Jimbo and M. Umeno, *Jpn. J. Appl. Phys.*, 40, pp.L505, (2001).
- [12] Kyong-Seok Chaea, Dong-Wook Kima, Bong-Soo Kimb, Sung-Jin Somc, In-Hwan Leea, Cheul-Ro Lee, *J. Cryst. Growth*, 276, pp.367–373, (2005).
- [13] A. Teke, S. Dogan, F. Yun, M.A. Reshchikov, H. Le, X.Q. Liu, H. Morkoc, S.K. Zhang, W.B. Wang and R.R. Alfano, *Solid-State Electron.*, 47, pp.1401–1408, (2003).
- [14] Adarsh Singh, Mridula Gupta and R. S. Gupta, *Opt. Eng.*, 42, pp.2563, (2003).
- [15] Seikoh Yoshida and Joe Suzuki, *J. Appl. Phys.*, 85, pp.7931, (1999).
- [16] S. Lawrence Selvaraj, Tsuneo Ito, Yutaka Terada, and Takashi Egawab, *Appl. Phys. Lett.*, 90, pp.173506, (2007).
- [17] C.-T. Liang, Li-Hung Lin, J. Z. Huang, Zhi-Yao Zhang, Zhe-Hau Sun, and Kuang Yao Chen, N. C. Chen, P. H. Chang, and Chin-An Chang, *Appl. Phys.*

Lett., 90, pp.022107, (2007).

[18] H.S. Kim, G.-Y. Yeom, J.W. Lee and T.I. Kim, Thin Solid Films, 341, pp.180, (1999).

[19] Y. B. Hahn, Y. H. Im, J. S. Park, K. S. Nahm and Y. S. Lee, J. Vac. Sci. Technol., A19, pp.1277, (2001).

[20] R. Cheung, R. J. Reeves, S. A. Brown, E. van der Drift and M. Kamp, J. Appl. Phys., 88, pp.7110, (2000).

[21] F. A. Khan, L. Zhou, V. Kumar and I. Adesida, J. Vac. Sci. Technol., B19, pp.2926, (2001).

[22] R. Cheung, R. J. Reeves, B. Rong, S. A. Brown, E. J. M. Fakkeldij, E. van der Drift and M. Kamp, J. Vac. Sci. Technol., B17, pp.2759, (1999).

[23] H. Cho, C.B. Vartuli, C.R. Abernathy, S.M. Donovan, S.J. Pearton, R.J. Shul and J. Han, Solid-State Electron., 42, pp.2277, (1998).

[24] X.A. Cao, H. Cho, S.J. Pearton, G.T. Dang, A.P. Zhang, F. Ren, R.J. Shul and J.M. Van Hove: Appl. Phys. Lett., 75, pp.232, (1999).

[25] J.M. Lee, K.-M. Chang, S.W. Kim, C. Huh, I.H. Lee and S.J. Park: J. Appl. Phys., 87, pp.7667, (2000).

[26] M. Nakaji, T. Egawa, H. Ishikawa, S. Arulkumaran and T. Jimbo, Jpn. J. Appl. Phys., 41, pp.L493, (2002).

- [27] P. Hacke, T. Detchprohm, K. Hiramatsu and N. Sawaki, *Appl. Phys. Lett.*, 63, pp.2676, (1993).
- [28] J.D. Guo, M.S. Feng, R.J. Guo, F.M. Pan and C.Y. Chang, *Appl. Phys. Lett.*, 67, pp.2657, (1995).
- [29] L. Wang, M.I. Nathan, T-H. Lim, M.A. Khan and Q. Chen, *Appl. Phys. Lett.*, 68, pp.1267, (1996).
- [30] J.D. Guo, F.M. Pan, M.S. Feng, R.J. Guo, P.F. Chou and C.Y. Chang, *J. Appl. Phys.*, 80, pp.1623, (1996).
- [31] J. S. Jang, S.J. Park and T.Y. Seong, *J. Vac. Sci. & Technol.*, B17, pp.2667, (1999).
- [32] H. Hasegawa and S. Oyama, *J. Vac. Sci. & Technol.*, B20, pp.1647, (2002).
- [33] J. I. Chyi, C. M. Lee, C.C. Chuo, X. A. Cao, G. T. Dang, A. P. Zhang, F. Ren, S. J. Pearton, S. N. G. Chu, R. G. Wilson, *Solid-State Electron.*, 44, pp.613, (2000).
- [34] A. P. Zhang, G. Dang, F. Ren, X. A. Cao, H. Cho, E. S. Lambers, S. J. Pearton, R. J. Shul, L. Zhang, A. G. Baca, R. Hickman, J. M. Van Hove, *J Electrochem Soc* 147, pp.719, (2000).
- [35] J. M. Lee, S. W. Kim and S. J. Park, *J Electrochem Soc*, 148, pp.G254, (2001).
- [36] R. Cheung, S. Withanage, R. J. Reeves, S. A. Brown, I. Ben-Yaacov, C. Kirchner and M. Kamp, *Appl Phys Lett*, 74, pp.3185, (1999).

- [37] M. Achouche, A. Clei and J. C. Harmand, *J Vac Sci Technol*, B14, pp.2555, (1996).
- [38] X. A. Cao, A. P. Zhang, G. T. Dang, H. Cho, F. Ren, S. J. Pearton, R. J. Shul, L. Zhang, R. Hickman and J. M. Vand Hove, B17, pp.1540, (1999).
- [39] R. J. Shul, L. Zhang, A. G. Baca, C. G. Willison, J. Han, S. J. Pearton and F. Ren, *J. Vac. Sci. Technol.*, A18, pp.1139, (2000).
- [40] H. B. Michaelson, *J. Appl. Phys.*, 48, pp.4729, (1977).
- [41] E. V. Kalinina, N. I. Kuznetsov, A. I. Babanin, V. A. Dmitriev and A. V. Shchukarev, *Diamond and related materials*, 6, pp.1528, (1977).
- [42] S. M. Sze, "Semiconductor Device Physics and Technology", pp.160, (1985).
- [43] S.M.Sze, "Physics of Semiconductor Devices" 2nd Edition, chapter 5.
- [44] S. C. Binari, H. B. Dietrich, G. Kelner, L. B. Rowland, K. Doverspike and D. K. Gaskill, *Electron. Lett.*, 30, pp. 909, (1994).
- [45] G. L. Chen, F. C. Chang, K. C. Shen, J. Ou, W. H. Chen, M. C. Lee, M. J. Jou and C. N. Huang, *Appl. Phys. Lett.*, 80, pp.595, (2002).
- [46] C. T. Lee, Y. J. Lin and D. S. Liu, *Appl. Phys. Lett.*, 79, pp.2573, (2001).
- [47] C. I. Wu, A. Kahn, A. E. Wichenden, D. Koleske and R. L. Henry, *J. Appl. Phys.*, 89, pp.425, (2001).
- [48] X.A.Cao, S.J.Pearnton, g.Dang, A.P.Zhang, F.Ren, J.M.Van Hove, *Appl. Phys.*

Lett. 75, pp.4130, (1999).

[49] A. C. Schmitz, A. T. Ping, M. A. Khan, Q. Chen, J. W. Yang and I. Adesida, J.

Electron. Mater. 27, pp. 255, (1998).

[50] D. K. Schroder, "SEMICONDUCTOR MATERIAL AND DEVICE CHARACTERIZATION", second edition, (1998).

[51] R.Hull., R.M.Osgood, J. H. Sakaki and A.Zunger, "Nitride Semiconductors and Devices", (1999).

[52] L.S.Yu, Q.Z.Liu, Q.J.Xing, D.J.Qiao and S.S.Lau, J. Appl. Phys., 84, pp.2099, (1998).

[53] A.Y.C.Yu, Solid-State Electron., 13, pp.239, (1970).

[54] Y. Kribes, I. Harrison, B. Tuck, T. S. Cheng and C. T. Foxon, Semicon. Sci. Technol, 12, pp.913, (1997).

[55] Z.Q.Shi and W.A.Anderson, J.Appl.Phys., 72, pp.3803, (1992).

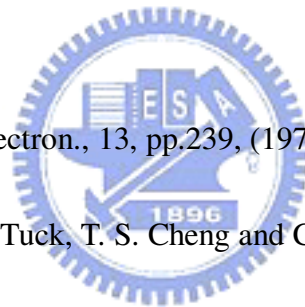
[56] H. Norde, J Appl. Phys., 50, pp.5052, (1979).

[57] R. M. Cibils and R. H. Buitrago, J. Appl. Phys., 58, pp.1075, (1985).

[58] K. Sato and Y. Yasumura, J. Appl. Phys., 58, pp.3655, (1985).

[59] J. C. Manificier, N. Brortryb, R. Ardebili and J. P. Charles, J. Appl. Phys., 64, pp.2502, (1988).

[60] S. Kar and W. E. Dahlke, Solid-State Electron., 15, pp.221, (1972).



- [61] A. Deneuveille, J. Appl. Phys., 45, pp.3079, (1974).
- [62] A. Singh, Solid-State Electron., 28, pp.223, (1985).
- [63] A. Singh, P. Cova, and R. A. Masut, J. Appl. Phys., 74, pp.6714, (1993).
- [64] H. H. Tseng and C. Y. Wu, J. Appl. Phys., 61, pp.299, (1987).
- [65] Z. Chen, D. G. Park, F. Stengal, S. N. Mohammad and H. Morkoc, Appl. Phys. Lett., 69, pp.230, (1996).
- [66] G. I. Roberts and C. R. Crowell, J. Appl. Phys., 41, pp.1767, (1970).
- [67] M. Beguwala and C. R. Crowell, Solid-State Electron., 17, pp.203, (1974).
- [68] H. L. F. Canque, J. Allison and M. J. Thompson, J. Appl. Phys., 54, pp.7025, (1983).
- [69] E. T. Yu and M. O. Manasreh, "III-V Nitride Semiconductor Application & Devices", pp.528, (2003).
- [70] K. Suzue, S.N. Mohammad, Z.F. Fan, W. Kim, O. Aktas, A.E. Botchkarev and H. Morkoc, J. Appl. Phys., 80, pp.4467, (1996).
- [71] Q. Z. Liu, L. S. Yu, S. S. Lau, J. M. redwing, N. R. Perkins and T. F. Kuech, Appl. Phys. Lett., 70, pp.1275, (1997).
- [72] J. Kim, F. Ren, B. P. Gila, C. R. Abernath and S. J. Pearton, Appl. Phys. Lett., 82, pp.739, (2003).
- [73] B. E. Deal, E. L. MacKenna and P. L. Castro, J. Electrochem. Soc., 116, pp.997,

(1969).

[74] S. Anand, S. Subramanian and B. M. Arora, *J. Appl. Phys.*, 72, pp.3535, (1992).

[75] E. Y. Chang, Y. L. Lai, K. C. Lin and C. Y. Chang, *J. Appl. Phys.*, 74, pp.5622,
(1993).

[76] H. Ishikawa, S. Kobayashi, Y. Koide, S. Yamasaki, S. Nagai, J. Umezaki and M.
Koike, *J. Appl. Phys.*, 81, pp.1315, (1997).

[77] K. Shiojima, J. M. Woodall, C. J. Eiting, P. A. Grudowski and R. D. Dupuis, *J.*
Vac. Sci. Technol., B17, pp.2030, (1999).

[78] Q. Z. Liu, L. S. Yu, F. Deng, S. S. Lau and J. M. Redwing, *J. Appl. Phys.*, 84,
pp.881, (1998).

[79] M. K. Hudait and S. B. Krupanidhi, *Solid-State Electron.*, 44, pp.1089, (2000).

[80] M. Schmeits, N. D. Nguyen and M. Germain, *J. Appl. Phys.*, 89, pp.1890,
(2001).

[81] N. M. Johnson, R.D. Burnham, R. A. Street and R. L. Thornton, *Phys. Rev. B*, 33,
pp.1102, (1986).

[82] H. J. Stein and S. Hahn, *J. Appl. Phys.*, 75, pp.3477, (1994).

[83] S. Gurumuthy, H. L. Bhat, B. Sundershesu, R. K. Bagai and V. Kumar, *Appl.*
Phys. Lett., 68, pp.2424, (1996).

[84] S.J.Pearton, S. Bendi, K. S. Jones, V. Krishnamoorthy, R. G. Wilson, F. Ren, R. F.

- Karlicek, Jr. and R. A. Stall, *Phys. Lett.* 69, pp.1879, (1996).
- [85] T. W. Kang, S. U. Yuldashev, D. Y. Kim and T. W. Kim, *Jpn. J. Appl. Phys.*, 39, pp.L25, (2000).
- [86] J. T. Torvik, J. I. Pankove, B. J. Van Zeghbroeck, *IEEE Trans. Electron. Dev.* 46, pp. 1326, (1999).
- [87] Z. M. Zhao, R. L. Jiang, P. Chen, D. J. Xi, B. Shen, R. Zhang and Y. D. Zheng, *J. Vac. Sci. Technol.*, B19, pp.286, (2001).
- [88] Y. K. Su, S. J. Chang, C. H. Chen, J. F. Chen, G. C. Chi, J. K. Sheu, W. C. Lai and J. M. Tsai, *IEEE sensors J.*, 2, pp.366, (2002).
- [89] S. K. Zhang, W. B. Wang, I. Shtau, F. Yun, L. He, H. Morkoc, X. Zhou, M. Tamargo and R. R. Alfano, *Appl. Phys. Lett.* 81, pp.4862, (2002).
- [90] S. W. Seo, K. K. Lee, S. Kang, S. Huang, W. A. Doolittle, N. M. Jokerst and A. S. Brown, *Appl. Phys. Lett.* 79, pp.1372, (2001).
- [91] H. Z. Xu, Z. G. Wang, M. Kawabe, I. Harrison, B. J. Ansell and C. T. Foxon, *J. Cryst. Growth*, 218, pp.1, (2000).
- [92] Z. M. Zhao, R. L. Jiang, P. Chen, D. J. Xi, Z. Y. Luo, R. Zhang, B. Shen and Z. Z. Chen, *Appl. Phys. Lett.*, 77, pp.444, (2000).
- [93] S. J. Chang, M. L. Lee, J. K. Sheu, W. C. Lai, Y. K. Su, C. S. Chang, C. J. Kao, G. C. Chi and J. M. Tsai, *IEEE Electron. Dev. Lett.*, 24, pp.212, (2003).

- [94] E. Monroy, F. Calle, E. Muñoz and F. Omnès, *Appl. Phys. Lett.*, 74, pp.3401, (1999).
- [95] E. Muñoz, E. Monroy, J. A. Garrido, I. Izpura, F. J. Sánchez, M. A. Sánchez-García, E. Calleja, B. Beaumont and P. Gibart, *Appl. Phys. Lett.*, 71, pp.870, (1997).
- [96] O. Katz, V. Garber, B. Meyler, G. Bahir and J. Salzman, *Appl. Phys. Lett.*, 79, pp.1417, (2001).
- [97] J. C. Carrano, T. Li, P. A. Grudowski, C. J. Eiting, R. D. Dupuis and J. C. Campbell, *J. Appl. Phys.*, 83, pp.6148, (1998).
- [98] S. J. Chung, O. -H. Cha, Y. S. kim, C. H. Hong, H. J. Lee, M. S. Jeong, J. O. White and E. -K. Suh, *J. Appl. Phys.*, 89, pp.5454, (2001).
- [99] R. H. Horng, D. S. Wu, S. C. Wei, S. H. Chan and C. Y. Kung, *Thin Solid Films*, 343-344, pp.642, (1999).
- [100] S. Cai, G. Parish, J. M. Dell and B. D. Nener, *J. Appl. Phys.*, 96, pp.1019, (2004).
- [101] J. Xu, D. You, Y. Tang, Y. Kang, X. Li, X. Li and H. Gong, *Appl. Phys. Lett.*, 88, pp.072106, (2006).
- [102] S. Cai, G. Parish, G. A. Umana-Membreno, J. M. Dell and B. D. Nener, *J. Appl. Phys.*, 95, pp.1081, (2004).

[103] F. Binet, J. Y. Duboz, E. Rosencher, F. Scholz and V. Härle, Appl. Phys. Lett, 69, pp.1202, (1996).

[104] O. Katz, G. Bahir and J. Salzman, Appl. Phys. Lett., 84, pp.4092, (2004).

[105] V. V. Ursaki, I. M. Tiginyanu, P. C. Ricci, A. Anedda, S. Hubbard and D. Pavlidis, J. Appl. Phys., 94, pp.3875, (2003).

[106] G. Beadie, W. S. Rabinovich, A. E. Wichenden, D. D. Koleske, S. C. Binari and J. A. Freitas, Jr, Appl. Phys. Lett, 71, pp.1092, (1997).

[107] H. M. Chen, Y. F. Chen, M. C. Lee and M. S. Feng, J. Appl. Phys., 82, pp.899, (1997).

[108] M. T. Hirsch, J. A. Wolk, W. Walukiewicz and E. E. Haller, Appl. Phys. Lett., 71, pp.1098, (1997).



[109] T. Y. Lin, H. C. Yang and Y. F. Chen, J. Appl. Phys., 87, pp.3404, (2000).

[110] X. Z. Dang, C. D. Wang, E. T. Yu, K. S. Boutros and J. M. Redwing, Appl. Phys. Lett., 72, pp.2745, (1998).

[111] X. Y. Guo, T. L. Williamson and P. W. Bohn, Solid States Communications, 140, pp.159, (2006).

[112] B. Poti, A. Passaseo, M. Lomascolo, R. Cingolani and M. D. Vittorio, Proceed. of SPIE, 5353, pp.97, (2004).

[113] J. Z. Li, J. Y. Lin, H. X. Jiang, A. Salvador, A. Botchkarev and H. Morkoc, Appl.

- Phys. Lett., 69, pp.1474, (1996).
- [114] M. Razeghi, P. Sandvik, P. Kung, D. Walker, K. Mi, X. Zhang, V. Kumar, J. Diaz, Mater. Sci. Eng., B74, pp.107, (2000).
- [115] D. Walker, E. Monroy, P. Kung, J. Wu, M. Hamiton, F. J. Sanchez, J. Diaz and M. Razeghi, Appl. Phys. Lett., 74, pp.762, (1999).
- [116] Z. C. Huang, D. B. Mott, P. K. Shu, R. Zhang, J. C. Chen and D. K. Wickenden, J. Appl. Phys., 82, pp.2707, (1997).
- [117] Y. Tian, S. J. Chua, H. Wang, Solid State Electron., 47. pp.1863. (2003).
- [118] C. A. Mead, Solid State Electron., 9, pp.1023, (1966).
- [119] J. J. Toriz-Garcia, P. J. Parbrook, D. A. Wood and J. P. R David, Electron Devices for Microwave and Optoelectronic Applications, 2001 Internal Symposium on, pp.131, (2001).
- [120] S. J. Chung, M. S. Jeong, O. H. Cha, C. -H. Hong, E. -K. Suh, H. J. Lee, Y. S. Kim and B. H. Kim, Appl. Phys. Lett., 76, pp.1021, (2000).
- [121] F. Omnès, N. Marengo, B. Beaumont, P. De mierry, E. Monroy, F. Calle and E. Muñoz, J. Appl. Phys., 86, pp.5286, (1999).
- [122] N. Vanhove, J. John , A. Lorenz, K. Cheng, G. Borghs and J.E> M. Harverkort, Appl. Surf. Sci., 253, pp.2930, (2006).
- [123]P. Visconti, M. A. Reshchikov, K. M. Jones, D. F. Wang, R. Cingolani, H.

Morkoc, R. J. Molnar, and D. J. Smith, *J. Vac. Sci. Technol.*, B19,
pp.1328, (2001).

[124]C. Youtsey, L. T. Romano and I. Adesida, *Appl. Phys. Lett.* 73, pp.797,
(1998).

[125] Z. H. Hwang, J. M. Hwang, H. L. Hwang and W. H. Hung, *Appl. Phys.*
Lett., 84, pp.3759, (2004).



Appendix B. Notation

- A contact or diode area, cm^2
- C junction capacitance, F
- C_M measured device capacitance and conductance with parallel model, F
- C_p interfacial states capacitance, F
- C_{sc} space charge capacitance, F
- C_{pi} *i-type* interfacial state capacitance ($i=s,m,f$), F
- C_{p-i-0} capacitance height of the plateaus region in the C_p -frequency relation, F.
- C_n electrons capture cross section
- C_p holes capture cross section,
- E electric field ($=V/L$)
- E_{00} characteristic energy, eV
- E_0 measure of tunneling probability in the TFE region, eV
- E_C energy at the bottom edge of the conduction band, eV
- E_V energy at the bottom edge of the valance band, eV
- E_F Fermi energy, eV
- E_g bandgap energy, eV
- f frequency, Hz
- G_M measured device conductance with parallel model
- $G(x)$ photon flux and is defined as a function of absorption depth in the semiconductor.
- I_S saturation current, Amp
- I_d dark current, Amp
- I_{ph} actual photocurrent, Amp
- I_p measured current, Amp
- J_R reverse saturation current density, Amp/cm^2

- J_{diff} diffusion current density, Amp/cm²
- J_{rec} recombination current, Amp/cm²
- J_S reverse current density, Amp/cm²
- J_{th} thermionic emission current, Amp/cm²
- J_{gen} generation current, Amp/cm²
- J_{gr} generation-recombination current, Amp/cm²
- K Boltzmann's constant ($=8.62 \times 10^{-5}$ eV/K)
- KT thermal voltage ($=0.0259$ eV at $T=300^\circ\text{C}$)
- K_S semiconductor dielectric constant $\left(K_{S|GaN} = \frac{\epsilon_S}{\epsilon_0} = 9.5 \right)$
- L finger length for MSM-PDs, cm
- N_{SS} interfacial states density, eV⁻¹ cm⁻²
- N_{ss-s} s -type interfacial states density, eV⁻¹ cm⁻² (s donate slow in low frequency range 100Hz to 1KHz)
- N_{ss-m} m -type interfacial states density, eV⁻¹ cm⁻² (m donate medium in medium frequency range 1KHz to 100KHz)
- N_{ss-f} f -type interfacial states density, eV⁻¹ cm⁻² (f donate fast in high frequency range 100KHz to 1MHz)
- N_d donor concentration, cm⁻³
- N_C effective density of states in the conduction band ($=2.59 \times 10^{18}$ cm⁻³ for GaN)
- N_V effective density of states in the valance band ($=1.79 \times 10^{19}$ cm⁻³ for GaN)
- N_t total concentration of trapping centers, cm⁻³
- n number of carriers in the thermal equilibration, cm⁻³
- n_i intrinsic carrier concentration ($=2.58 \times 10^{10}$ cm⁻³ for GaN)
- P_{inc} incident optical power (Watt)

- q electronic charge
- R_S series resistance, Ω
- S diode cross-sectional area, cm^2
- T temperature, K
- V applied bias voltage, Volt
- V_{bi} built in potential, Volt
- V_n energy of the Femi level of the semiconductor with respect to the bottom

of the conduction band.
$$V_n = \frac{E_C - E_F}{q} = \frac{KT}{q} \ln\left(\frac{N_C}{N_d}\right), \quad [V]$$

- W space charge region width, cm
- W finger width for MSM-PDs, cm
- Φ_m metal work function, eV
- Φ_s semiconductor work function, eV
- Φ_e effective barrier height, eV ($=\phi_{B0} - \Delta\phi_{B0}$)
- $\Delta\phi_{B0}$ barrier lowering at zero bias due to image force, eV
- χ_s semiconductor electron affinity, eV
- η ideality factor
- ρ_c specific contact resistance, $\Omega\text{-cm}^2$
- A^* Richardson's constant, $\text{A} \cdot \text{cm}^{-2}\text{K}^{-2}$
- h Planck's constant ($=6.625 \times 10^{-34}$ J-s= 4.135×10^{-5} eV-s)
- $h\nu$ photon energy, eV
- ν frequency of the light
- ϵ_0 permittivity of free space ($=8.85 \times 10^{-14}$ F/cm)
- ϵ_S permittivity of the semiconductor, F/cm
- m free electron mass ($=9.1 \times 10^{-31}$ kg)

m^* effective mass of the tunneling electron, kg

$$\text{Electrons} \left(\frac{m_n^*}{m_0} \right)_{\text{GaN}} = 0.22$$

$$\text{Holes} \left(\frac{m_p^*}{m_0} \right)_{\text{GaN}} = 0.8$$

τ relaxation time, second

τ_0 life time of minority carrier in the space charge region, second

ω angular frequency ($=2\pi f$)

η_{ext} external quantum efficiency

Γ_G internal gain

λ_c cutoff wavelength, nm

w finger width for MSM-PDs, cm

r optical power of reflectance at the surface

$$\left(r = \left(\frac{n_1 - n_2}{n_1 + n_2} \right)^2, n_{1\text{GaN}} = 2.5, n_{2\text{air}} = 1, r = 0.18 \right)$$

α absorption coefficient of material ($=2 \times 10^4 \text{ cm}^{-1}$ for GaN, $\lambda_c=370\text{nm}$)

$1/\alpha$ penetration depth, cm

d absorption depth, cm

D absorption depth, cm

t_r carrier transit time, second

n electrons concentration, cm^{-3}

p holes concentration, cm^{-3}

Appendix C. Detailed experimental discussion

C.1 Epitaxial growth for GaN

C.1.1 Schottky diodes and metal-semiconductor-metal photodetector (MSM-PDs)

In this experiment, GaN films were grown by metalorganic chemical vapor deposition (MOCVD). The GaN films were grown at one atmospheric partial pressure or low pressure. The sapphire with (0001) orientation (C-face) was used as a substrate. Trimethylgallium (TMG) and ammonia (NH₃) were used as Ga and N sources, respectively. The SiH₄ was used as Si dopant source to obtain n-type GaN. First, the substrate was heated to 1100°C in a stream of hydrogen. Then, the substrate temperature was lowered between 450°C and 600°C to grow the GaN nucleation layer. The thickness of the GaN buffer layer was controlled between 100 Å and 1200 Å. Next, the substrate temperature was elevated in the range of 1000°C and 1100°C to grow the GaN film. The total thickness of the GaN film was about 3~4 um. The growth time was about 60 minutes.

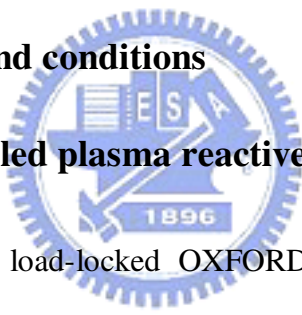
C.1.2 *p-i-n*-photodiodes

On the other hand, the visible-blind AlGaIn-based *p-i-n*-photodiodes structures consists of a low temperature GaN nucleation layer at 520°C, After this, the

growth temperature subsequently is elevated to 1120°C to epitaxy devices structure as the followings: 2µm of undoped GaN, 2µm of n⁺-GaN (2x10¹⁸ cm⁻³) as same mentioned described, 50nm of n-GaN (5 x10¹⁷ cm⁻³) as n contact layer, 300nm of undoped Al_{0.13}Ga_{0.87}N as intrinsic absorbed layer, and 50nm of p⁺-GaN (5 x10¹⁷ cm⁻³). In addition multiple quantum wells (MQWs), the LEDs structure is nearly same *p-i-n*-photodiodes structures. The MQWs layer comprises five periods of InGaN/GaN and is grown in the range of 750°C to 850°C.

C.2 Process procedure and conditions

C.2.1 Inductively coupled plasma reactive ion etching (ICP-RIE)



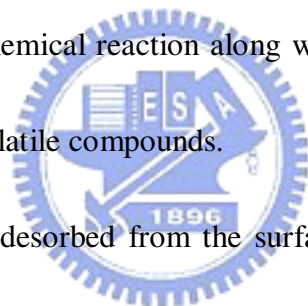
The ICP reactor was a load-locked OXFORD plasmalab system 100. Etch system with the ICP source. The plasma region was cylindrical. This low aspect ratio was contributed to the high plasma production efficiency, and it reduced the ratio of the plasma flux hitting the walls to the plasma flux hitting to the wafer. A circular array of magnetic line cusps was used to aid in plasma confinement and was improved uniformity. The plasma was driven by a coil, and was separated from the plasma by a dielectric window at 13.56 MHz.

The wafer was hold by an electrostatic chuck and helium which was used as heat transfer medium between the wafer and the chunk. The chunk could be rf biased at

13.56 MHz to control ion energies to the wafer independently from production of the plasma. The chuck was located many skin depths away from the coil, so that the wafer was not affected by the electromagnetic fields generated by the coil.

The plasma-assisted etching process proceeds in four steps. The process began with the generation of etchant species in the plasma.

1. The reactant was transported by diffusion through a stagnant gas layer to the surface.
2. The reactant was adsorbed to the surface.
3. This was followed by chemical reaction along with physical effects such as ion bombardment to form volatile compounds.
4. These compounds were desorbed from the surface, and were diffused into the bulk gas, and were pumped out by the vacuum system.



The ICP reactor was a load-locked OXFORD plasmalab system 100. Etch system with the ICP source was shown in Fig C.1.

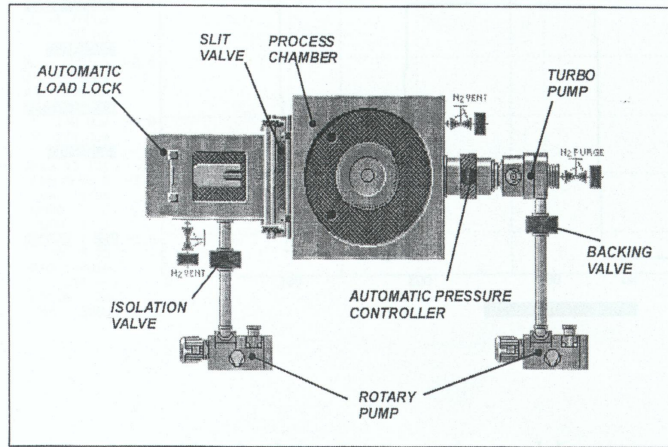


Fig.C.1 OXFORD Plasmalab System 100

C.2.2 Schottky diodes by ICP-RIE etching processes

The samples of Si doped GaN epitaxial layer were grown by using metalorganic chemical vapor deposition (MOCVD). The structure of the samples consisted of a 2- μm -thick n-type GaN layer on top of a 2- μm -thick undoped GaN layer on a c-face sapphire substrate. The Hall-effect measurements by using the Van der Pauw configuration revealed that the films were n-type, and the effective concentration was approximately $2 \times 10^{17} \text{ cm}^{-3}$, and the mobility was $450 \text{ cm}^2/\text{V s}$. Figure C.2 indicated that schematic process of Schottky diodes with ICP etching process. A multilayer of Cr/Al/Cr/Au ($150\text{\AA} / 3000\text{\AA} / 150\text{\AA} / 3000\text{\AA}$) for ohmic contacts was deposited on

n-GaN by the thermal evaporation in a vacuum below 2×10^{-6} Torr, with a purity of > 99.999 %, followed by the annealing process at 600°C for 20 min in N_2 ambient to achieve good ohmic contacts. The specific contact resistance (ρ_c) was around $1.2 \times 10^{-3} \Omega\text{cm}^2$. Samples were then exposed to certain inductively coupled plasma reactive ion etching (ICP-RIE) conditions. Then samples were exposed to ICP-RIE with Cl_2/Ar (30sccm/10sccm) gases. The pressure was 3m Torr, the coil power was 500W, and the platen power was 150W. To measure etch rates, the samples were patterned with AZ1500 (positive resist) photo-resist by spin coating. The etch depths were used to calculate etch deep, which were about 500 \AA by an Alpha-step stylus profilometer. Then the photo-resist was removed by acetone. After the ICP etching process, some certain damages were expected in GaN. This was followed by the annealing process at different temperatures from 400°C to 700°C with increasing 100°C in N_2 and H_2 ambient to remove the ion damage. After the annealing process, Schottky contacts were produced by the deposition of Ni/Au ($1000 \text{ \AA} / 3000 \text{ \AA}$) on the selected region with lift-off technology. The Schottky contacts area was $6 \times 10^{-4} \text{ cm}^2$. Prior to any processing, the samples were cleaned to remove the residual oxygen and carbon. The cleaning steps were described as follows:

1. In boiling aqua regia for 3 minutes.
2. Rinsing in acetone (ACE) by ultrasonic agitation for 3 minutes.

3. Rinsing in methanol (CH_3OH) for 3 minutes.
4. Rinsing in de-ionized water ($\text{DI, H}_2\text{O}$) for 3 minutes.



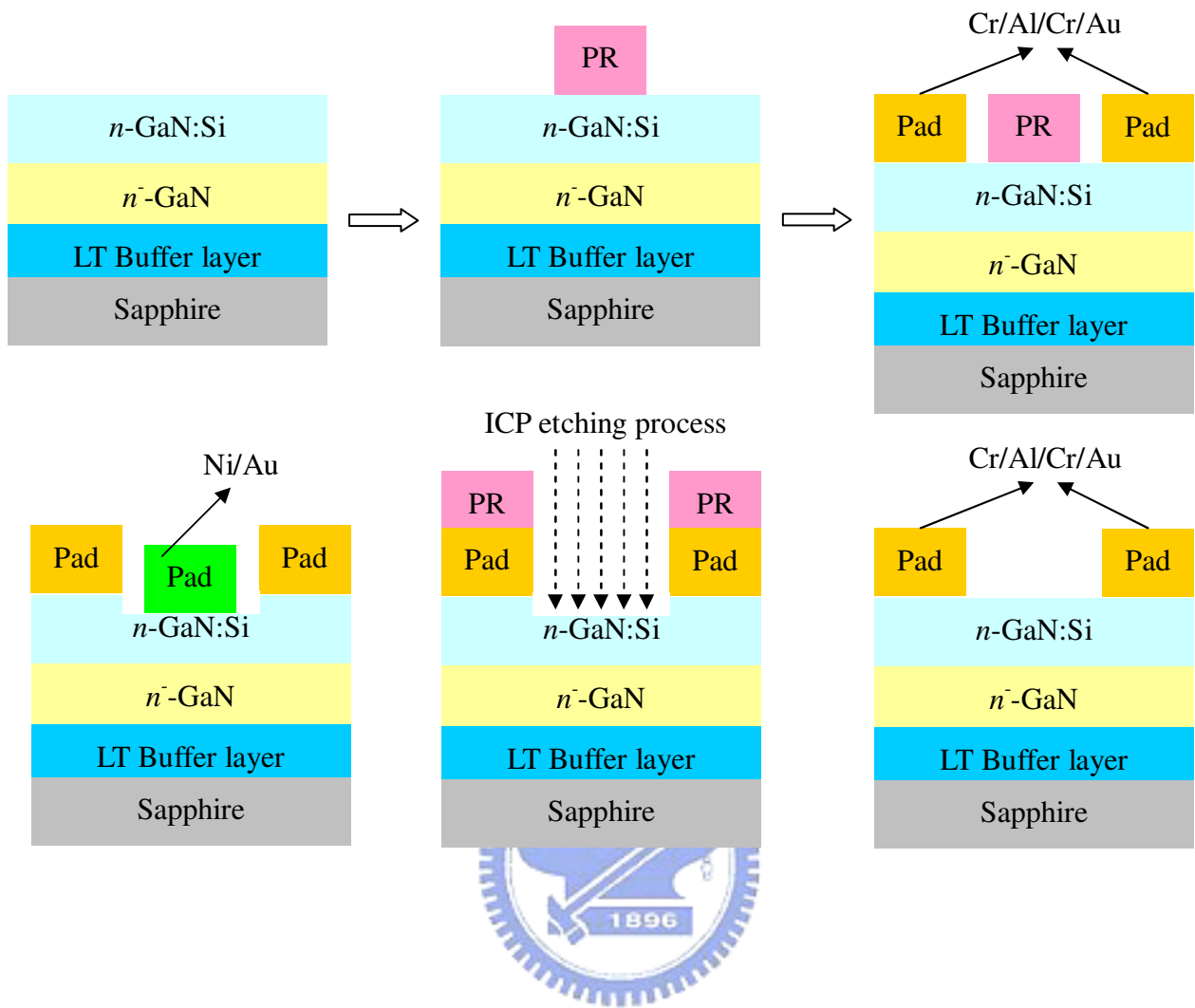


Fig.C.2 Fabrication process flow of Schottky diodes

C.2.3 AlGaN-based *p-i-n* photodiodes with different surface treatment

Visible-blind AlGaN-based photodiodes (PDs) were grown on sapphire substrates by using metalorganic chemical vapor deposition (MOCVD). The epitaxial structure consists of a sapphire substrate with a low temperature GaN nucleation layer, 2 μm of undoped GaN, 2 μm of n^+ -GaN ($2 \times 10^{18} \text{ cm}^{-3}$), 50nm of n -GaN ($5 \times 10^{17} \text{ cm}^{-3}$), 300nm of undoped $\text{Al}_{0.13}\text{Ga}_{0.87}\text{N}$, and 50nm of p^+ -GaN ($5 \times 10^{17} \text{ cm}^{-3}$). Samples are then etched to n^+ GaN region by using ICP etching process with standard photolithography process. Subsequently, the samples of the AlGaN-based photodiode devices were annealed with N_2 (as “ N_2 -treated PDs”) or H_2 (as “ H_2 -treated PDs”) ambient at 600°C for 30 minutes to reduce the ICP-induced defects after the ICP etching process. The p type ohmic contacts of the AlGaN-based photodiode devices were processed by evaporation of Ni/Au (5nm /8nm) with photolithography technology, and were annealed at 550°C for 10 min in air in a furnace. A SiO_2 layer was then deposited by plasma-enhanced chemical vapor deposition (PECVD) to serve as the anti-reflection coating as well as the surface passivation layer. The Ti/Al/Ti/Au metals were patterned as n -type contacts by standard lift-off process. The AlGaN-based photodiode devices structure with different surface treatments is shown in Fig. C.3.

On the other hand, samples were then immersed in the boiling KOH solution for 80s after ICP-etched process, and they were rinsed in the DI water and were dried by the nitrogen gas (as “KOH-treated PDs”). After that, the procedure for both of as-grown and KOH-treated PDs would be the same and as the followings. The Ni/Au contacts on the p-type layer were then formatted with the photolithography technology and were subsequently annealed in a furnace at 550°C for 10 min in air. A SiO₂ layer was then deposited by plasma-enhanced chemical vapor deposition (PECVD) to serve as the anti-reflection coating as well as the surface passivation layer. The Ti/Al/Ti/Au metals as the n-type contacts were then patterned by standard lift-off process. The diode area was 1×10^{-3} cm². The current-voltage (I-V) measurements of AlGaIn-based photodiode devices were characterized by a Hewlett-Packard 4156 semiconductor analyzer. The spectral responsivity of AlGaIn-based photodiode devices was measured by a Xenon arc lamp and a monochromator (SPX1000). All the optical systems were calibrated by using a UV-enhanced silicon photodiode.

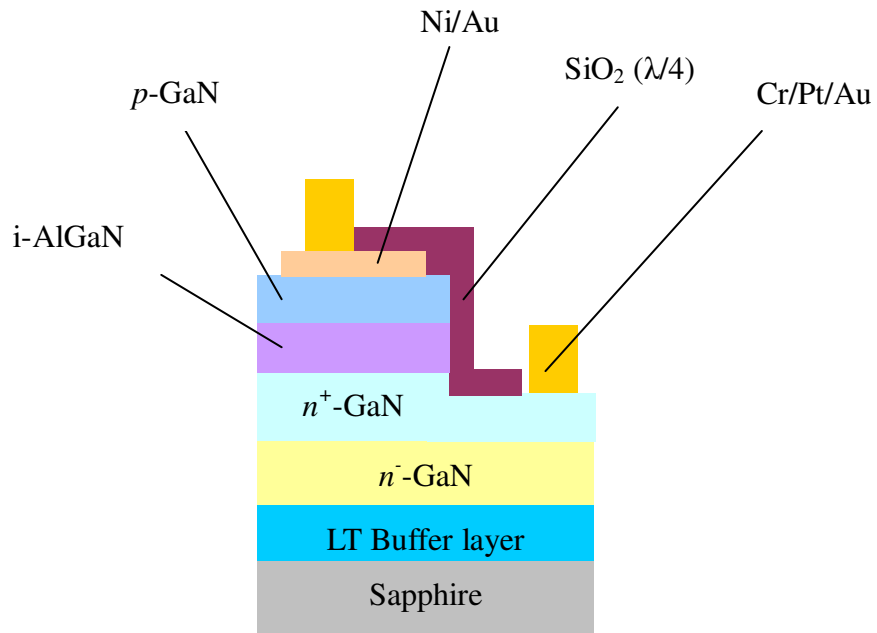
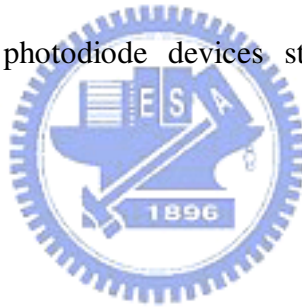


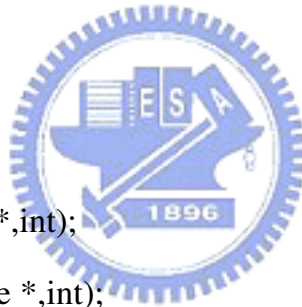
Fig. C.3. The AlGaN-based photodiode devices structure with different surface treatments.



Appendix D. Current voltage characteristics analysis and simulation by C language tools

```
#include <math.h>
#include <stdio.h>
#include <stdlib.h>
#include <process.h>
#include <IV_100.h>
#include <I_100.h>
#include <IV.h>
```

```
void main()
{
    FILE *out;
    void voltage(float *,int);
    void current(double *,int);
    char name[10];
    double X[500]={0};
    double Y[500]={0};
    double Total_d=0,d=0;
    double Total_I=0;
    float Group_V[500]={0};
    double Group_I[500]={0};
    float Group_n[500]={0};
    double Group_Is[500]={0};
    float Start_V,End_V,Step_V,Count_V=0;
```



```

float From_Is,To_Is,Step_Is;

float From_n,To_n,Step_n;

float Rs,n,Is;

float T,KT;

double A=1,C,E=0;

float B;

int i,m;

float j;

float *V=0;

double *I=0;

/*-----*/

float X1,X2,Y1,Y2;
double Result_Is;
float Slope_Is,Interrept_Is;

/*-----*/

printf("\n");

printf("Start fit volt (0.1)=");

scanf("%f",&Start_V);

printf("End fit volt (0.3)=");

scanf("%f",&End_V);

printf("Voltage step (0.01)=");

scanf("%f",&Step_V);

/*-----*/

printf("Measured T (300K)=");

scanf("%f",&T);

/*-----*/

```



```

/*      printf("Is region from (10E-11)=");
        scanf("%f",&From_Is);
        printf("Is region to (1E-11)=");
        scanf("%f",&To_Is);
        printf("Is region step (1E-12)=");
        scanf("%f",&Step_Is);                                */

/*-----*/

        printf("n region from (1)=");
        scanf("%f",&From_n);
        printf("n region to (2)=");
        scanf("%f",&To_n);
        printf("n region step (0.01)=");
        scanf("%f",&Step_n);

/*-----*/

        printf("save file name (*.txt) =");
        scanf("%s",&name);
        out=fopen(name,"w");

/*-----*/

        KT=T*8.617E-5;

/*-----*/

        Count_V=Start_V/Step_V;
        j=(End_V)/Step_V;

/*-----*/

        printf("T=%5.1f A\n",T);
        fprintf(out,"T=%5.1f A\n",T);

voltage(V,j);

```



```

for(i=0;i<j;i++)
    Group_V[i]=*(V+i);
current(I,j);
for(i=0;i<j;i++)
    Group_I[i]=*(I+i);
fprintf(out,"V\t\t");
fprintf(out,"I(cal.)\n");
for(i=0;i<j;i++)
{
    printf("V%d=%5.2f\t",i,Group_V[i]);
    printf("I%d=%5.3e\n",i,Group_I[i]);
    fprintf(out,"V%d=%5.2f\t",i,Group_V[i]);
    fprintf(out,"\t");
    fprintf(out,"%5.3e\n",Group_I[i]);
}
for(i=0;i<5;i++)
fprintf(out,"\n");
fprintf(out,"V\t");
fprintf(out,"I(mea.)\t\t");
fprintf(out,"I(cal.)\t\t");
fprintf(out,"distance\t");
fprintf(out,"Rs\t");
fprintf(out,"n\t");
fprintf(out,"Is\n\n");

/*-----*/

X1=Group_V[Count_V];

```

```

X2=Group_V[j-1];
Y1=log10(Group_I[Count_V]);
Y2=log10(Group_I[j-1]);
Slope_Is=(Y2-Y1)/(X2-X1);
Interrept_Is=Y1-(X1*Slope_Is);
Result_Is=exp(Interrept_Is*2.3);
From_Is=Result_Is*10;
To_Is=Result_Is/10;
Step_Is=Result_Is/10;

```

```

/*-----*/

```

```

for(i=Count_V;i<j;i++)
{
    A=1;
    for(n=From_n;n<To_n;n=n+Step_n)
    {
        for(Is=From_Is;Is>To_Is;Is=Is-Step_Is)
        {
            Total_I=Is*(exp((Group_V[i]/(n*KT))-1);
            d=fabs(Total_I-Group_I[i]);
            if(d<A)
            {
                A=d;
                Group_n[i]=n;
                Group_Is[i]=Is;
                Y[i]=Total_I;
            }
        }
    }
}

```

```

    }
}
printf("V%d=%5.2f\t",i,Group_V[i]);
printf("d=%5.3e\t",A);
printf("n=%4.2f\t",Group_n[i]);
printf("Is=%5.3e\t",Group_Is[i]);
printf("I=%5.3e\n",Y[i]);
fprintf(out,"V%d=%5.2f\t",i,Group_V[i]);
fprintf(out,"I=%5.3e\t",Group_I[i]);
fprintf(out,"I=%5.3e\t",Y[i]);
fprintf(out,"d=%5.3e\t",A);
fprintf(out,"n=%4.2f\t",Group_n[i]);
fprintf(out,"Is=%5.3e\n",Group_Is[i]);
}
for(i=0;i<5;i++)
{
    printf("\n");
    fprintf(out,"\n");
}

/*-----*/

for(m=Count_V;m<j;m++)
{
    Total_d=0;
    A=1e20;
    for(i=Count_V;i<j;i++)
    {

```

```

Total_I=Group_Is[m]*(exp((Group_V[i]/(Group_n[m]*KT))-1);
d=fabs(Total_I-Group_I[i]);
Total_d=Total_d+d;
if(Total_d<A)
{
    A=Total_d;
    B=Group_n[m];
    C=Group_Is[m];
}
}

printf("V%d=%4.1ft",m,Group_V[m]);
printf("one point total distance=%e\t",Total_d);
printf("n=%4.2ft",B);
printf("Is=%5.3e\n",C);
fprintf(out,"V%d=%5.2ft",i,Group_V[m]);
fprintf(out,"one point total distance=%e\t",Total_d);
fprintf(out,"n=%4.2ft",B);
fprintf(out,"Is=%5.3e\n",C);
}

/*-----*/

Total_d=0;
A=1e20;
for(m=Count_V;m<j;m++)
{
    Total_d=0;
    for(i=Count_V;i<j;i++)

```

```

    {

Total_I=Group_Is[m]*(exp((Group_V[i])/(Group_n[m]*KT))-1);

    d=fabs(Total_I-Group_I[i]);
    Total_d=Total_d+d;
    if(Total_d<A)
A=Total_d;
    }
    X[m]=Total_d;
}

/*-----*/

for(i=Count_V;i<j;i++)
    for(m=i+1;m<j;m++)
        if(X[i]>X[m])
            {
E=X[i];
X[i]=X[m];
X[m]=E;

B=Group_n[i];
Group_n[i]=Group_n[m];
Group_n[m]=B;

C=Group_Is[i];
Group_Is[i]=Group_Is[m];
Group_Is[m]=C;

```

```

        }

        Total_d=X[Count_V];

        B=Group_n[Count_V];

        C=Group_Is[Count_V];

/*-----*/

        for(i=0;i<2;i++)

        {

                printf("\n");

                fprintf(out,"\n");

        }

        printf("Inital_Is=%5.3e\n",Result_Is);

        printf("Curve total distance=%e\n",Total_d);

        printf("n=%4.2f\n",B);

        printf("Is=%5.3e\n",C);

        fprintf(out,"Inital_Is=%5.3e\n",Result_Is);

        fprintf(out,"Curve total distance=%e\n",Total_d);

        fprintf(out,"n=%4.2f\n",B);

        fprintf(out,"Is=%5.3e\n",C);

        fclose(out);

}

```

Appendix E. Publications

(A) Referred papers

- [1] Kuo-Chin Huang, Wen-How Lan and Kai Feng Huang, “Inductively Coupled Plasma Reactive Ion Etching-Induced GaN Defect Studied by Schottky Current Transport Analysis”, Japanese Journal of Applied Physics, Vol. 43, pp.82-85, 2004.
- [2] Wen-How Lan, Kuo-Chin Huang and Kai Feng Huang, “Surface KOH treatment in AlGaIn-based photodiodes” Electronics Letters, Vol.42, pp.821-822, 2006.
- [3] Wen-How Lan, Kuo-Chin Huang and Kai Feng Huang, “ICP-Induced Defects in GaN Characterized by Capacitance Analysis”, Solid-State Electronics, Vol.50, pp. 1677-1681, 2006.
- [4] J. C. Lin, Y. K. Su, S. J. Chang, W. H. Lan, K. C. Huang, W. R. Chen, C. Y. Huang, W. C. Lai, W. J. Lin and Y. C. Cheng, “High responsivity of GaN p-i-n photodiode by using low-temperature interlayer”, Applied Physics Letters, Vol.91, pp.173502, 2007.
- [5] J.C. Lin, Y.K. Su, S.J. Chang, W.H. Lan, K.C. Huang, W.R. Chen, Y.C. Cheng, and W.J. Lin, “GaN-based light-emitting diodes prepared on vicinal sapphire substrates”, IET Optoelectronics , Vol.1, pp. 23-26, 2007.

- [6] J.C. Lin, Y.K. Su, S.J. Chang, W.H. Lan, K.C. Huang, W.R. Chen, C.H. Lan, C.C. Huang, W.J. Lin, Y.C. Cheng and C.M. Chang, “GaN p-i-n photodetectors with an LT-GaN interlayer”, IET Optoelectronics , Vol.2, pp. 59-62, 2008.
- [7] Kuo-Chin Huang, Wen-How Lan and Kai Feng Huang, “Enhancement of Light Output Power of InGaN/GaN Multiple Quantum Well Light-Emitting Diodes by Titanium Dioxide Texturing”, Japanese Journal of Applied Physics, Vol.47, pp. 5438-5440, 2008.
- [8] K.C. Huang, W.H. Lan, K. F. Huang, J.C. Lin, Y.C. Cheng, W.J. Lin and S. M. Pan, “High light output intensity of titanium dioxide textured light-emitting diodes”, Solid-State Electronics, Vol.52, pp.1154-1156, 2008.
- [9] Wen-How Lan, Kuo-Chin Huang, Kai Feng Huang, Jia-Ching Lin, Yi-Cheng Cheng and Wen-Jen Lin, “Annealing of defect states in reactive ion etched GaN”, Journal of Physics and Chemistry of Solids, Vol.69, pp. 719-723, 2008.
- [10] J.C. Lin, Y.K. Su, S.J. Chang, W.H. Lan, W.R. Chen, K.C. Huang, Y.C. Cheng and W.J. Lin, “Low Dark Current GaN p-i-n Photodetectors With a Low-Temperature AlN Interlayer”, IEEE Photonics Technology Letters, Vol.20, pp. 1255-1257, 2008.
- [11] J.C. Lin, Y.K. Su, S.J. Chang, W.H. Lan, K.C. Huang, Y.C. Cheng and W.J. Lin, “Improved External Quantum Efficiency of GaN p-i-n Photodiodes With a TiO₂

Roughened Surface”, IEEE Photonics Technology Letters, Vol.20, pp. 285-287, 2008.

(B) Conference papers

[1] Wen-How Lan, Kuo-Chin Huang, Kai Feng Huang, Jia-Ching Lin, Yi-Cheng Cheng and Wen-Jen Lin, “Influences of hydrogen-related state in GaN”, The 2nd International Symposium on Point Defect and Nonstoichiometry, We-B2-4, 2005.

[2] Kuo-Chin Huang, Kai-Feng Huang, Wen-How Lan, Wen-Hung Liu, Jia-Ching Lin, Wen-Jen Lin, Han-Zhong Liao, “Low dark current AlGaIn-based p-i-n photodiodes with low doping p-GaN:Mg layer structure, “2008 International Conference on Optics and Photonics in Taiwan” pp.96, 04-06, 2008.

